



## 저작자표시-비영리-변경금지 2.0 대한민국

이용자는 아래의 조건을 따르는 경우에 한하여 자유롭게

- 이 저작물을 복제, 배포, 전송, 전시, 공연 및 방송할 수 있습니다.

다음과 같은 조건을 따라야 합니다:



저작자표시. 귀하는 원저작자를 표시하여야 합니다.



비영리. 귀하는 이 저작물을 영리 목적으로 이용할 수 없습니다.



변경금지. 귀하는 이 저작물을 개작, 변형 또는 가공할 수 없습니다.

- 귀하는, 이 저작물의 재이용이나 배포의 경우, 이 저작물에 적용된 이용허락조건을 명확하게 나타내어야 합니다.
- 저작권자로부터 별도의 허가를 받으면 이러한 조건들은 적용되지 않습니다.

저작권법에 따른 이용자의 권리는 위의 내용에 의하여 영향을 받지 않습니다.

이것은 [이용허락규약\(Legal Code\)](#)을 이해하기 쉽게 요약한 것입니다.

[Disclaimer](#)

이학박사 학위논문

**Deformation microstructures of  
talc, chloritoid and serpentine, and  
their contributions to seismic  
anisotropy in subduction zones**

활석, 경록니석, 그리고 사문석의 변형미구조와  
이들이 섭입대에서 지진파 이방성에 미치는 영향

2023 년 8 월

서울대학교 대학원

지구환경과학부

이 정 진

Doctoral Thesis

**Deformation microstructures of  
talc, chloritoid and serpentine, and  
their contributions to seismic  
anisotropy in subduction zones**

**Jungjin Lee**

A dissertation submitted in partial fulfillment of the  
requirements for the degree of Doctor of Philosophy

**School of Earth and Environmental Sciences**

**Seoul National University**

**August, 2023**

# **Deformation microstructures of talc, chloritoid and serpentine, and their contributions to seismic anisotropy in subduction zones**

지도 교수 정 해 명

이 논문을 이학박사 학위논문으로 제출함  
2023 년 5 월

서울대학교 대학원  
지구환경과학부  
이 정 진

이정진의 이학박사 학위논문을 인준함  
2023 년 7 월

위 원 장 \_\_\_\_\_ 김 영 희 \_\_\_\_\_ (인)

부위원장 \_\_\_\_\_ 정 해 명 \_\_\_\_\_ (인)

위 원 \_\_\_\_\_ 이 현 우 \_\_\_\_\_ (인)

위 원 \_\_\_\_\_ 우 주 선 \_\_\_\_\_ (인)

위 원 \_\_\_\_\_ 박 문 재 \_\_\_\_\_ (인)



## ABSTRACT

# **Deformation microstructures of talc, chloritoid and serpentine, and their contributions to seismic anisotropy in subduction zones**

Jungjin Lee

School of Earth and Environmental Sciences

The Graduate School

Seoul National University

Seismic anisotropy has been observed in worldwide subduction zones, and one generally accepted hypothesis is that hydrous mineral abundant in subduction zones by intense hydration is important to understand the seismic anisotropy. Hydrous minerals have been characterized by intrinsically high elastic anisotropy of their single crystal, and their strong crystallographic preferred orientations (CPOs) formed by plastic deformation can play a key role to generate a strong seismic

anisotropy in subduction zones. However, there are a lot of hydrous minerals in subduction zones and a lack of study about their CPOs formed by subduction-related deformation. Talc and chloritoid are representative hydrous minerals in mantle wedge and subduction zone interfaces, and serpentine is considered to be the most abundant hydrous mineral in the mantle wedge. Therefore, I measured the CPOs of talc in garnet-chloritoid-talc schists in the Makbal complex in Tianshan (Kazakhstan-Kyrgyzstan) and talc-tremolite-chlorite schists in the Valla complex in Scotland (England), the CPOs of chloritoid in the Makbal Grt-Cld-Tlc schists, and the CPOs of antigorite serpentine in diopside serpentinites in the Monte San Petrone area in Corsica (France).

The CPO of talc showed the strong concentration of [001] axes normal /subnormal to the foliation and the weak girdle of (100) and (010) poles subparallel to the foliation. The strong alignment of talc [001] axes caused high P-wave anisotropy ( $AV_p = 67 - 72 \%$ ), and negative radial anisotropy of P-wave at high-angle ( $\theta > 50^\circ$ ) subduction zones.

The CPO of chloritoid displayed a strong distribution of [001] axes subnormal to the foliation and the weak girdle of (100) and (010) poles subparallel to the foliation. The elastic anisotropy of single-crystal chloritoid was calculated for the first time, and the P–T stability of chloritoid was re-evaluated by pseudosection studies. It was found that the combination of the CPO and the elastic anisotropy can

influence the trench-parallel anisotropy of S-wave ( $AVs = 9.7 - 18.1 \%$ ) in subduction zones with cold geotherms.

The CPO of antigorite serpentine presented the strong maxima of [001] axes normal/subnormal to the foliation with a weak girdle normal to the lineation. Combined with the CPO of diopside in the serpentinites, it was found that the formation of serpentine CPO can be influenced by topotactic growth of serpentine from diopside. This analysis also revealed a new type of diopside CPO of (100) poles strongly oriented normal to the foliation, which can be formed by the basal glide of serpentine (001) plane under the syn-kinematic serpentinization. It suggested that the antigorite CPO can be very important to cause the trench-parallel S-wave anisotropy in subduction zones.

In summary, it is emphasized that the strong CPOs of hydrous minerals such as talc, chloritoid, and serpentine, play an important role in interpreting the anomalously strong seismic anisotropy observed in subduction zones.

**Keywords:** CPO, talc, chloritoid, serpentine, seismic anisotropy, subduction zone

Student Number : 2016-37813

# TABLE OF CONTENTS

ABSTRACT .....	i
TABLE OF CONTENTS .....	iv
LIST OF FIGURES.....	ix
LIST OF TABLES.....	xv
LIST OF PUBLICATIONS.....	xvi
CHAPTER 1. Introduction.....	1
CHAPTER 2. Crystallographic preferred orientation of talc and implications for seismic anisotropy in subduction zones .....	5
Abstract .....	5
2.1 Introduction.....	7
2.2 Materials and Method .....	9
2.2.1 Geological settings of rock specimens and sample description .....	9
2.2.2 Measurement of CPOs of minerals.....	15
2.2.3 Calculation of seismic anisotropy of polycrystalline talc .....	16
2.3 Results .....	18

2.3.1 CPO of talc and other minerals.....	22
2.3.2 Seismic anisotropy of polycrystalline talc and whole rock.....	29
2.4 Discussion .....	38
2.4.1 CPO development of talc.....	38
2.4.2 Implication of talc CPO to the P-wave seismic anisotropy in subduction zones .....	40
2.4.3 Implication of talc CPO to the S-wave seismic anisotropy in subduction zones .....	43
2.5 Conclusion .....	49

## CHAPTER 3. Seismic anisotropy in subduction zones: evaluating the role of chloritoid..... 50

Abstract.....	50
3.1 Introduction.....	52
3.2 Materials and Method .....	54
3.2.1 Rock samples .....	54
3.2.2 Measurement of the CPO.....	55
3.2.3 Elasticity of single-crystal chloritoid.....	58
3.2.4 Calculation of the seismic velocity and anisotropy .....	61
3.2.5 Calculation of the thermodynamic stability and modal abundance of chloritoid .....	65
3.3 Results.....	72

3.3.1 CPOs of chloritoid .....	72
3.3.2 Elastic constant and seismic anisotropy of chloritoid.....	74
3.3.3 Thermodynamic stability and modal abundance of chloritoid.....	79
3.4 Discussion .....	80
3.4.1 CPO development of chloritoid .....	80
3.4.2 Chloritoid stability and its implication for seismic anisotropy in subduction zones .....	82
3.4.3 Effect of chloritoid CPO on seismic anisotropy of the Grt-Cld-Tlc schist.....	87
3.4.4 Effect of hydrous minerals in blueschist-facies rock on seismic anisotropy .....	92
3.5 Conclusion .....	98

## CHAPTER 4. Deformation fabrics of diopside and antigorite in serpentinites and implications for seismic anisotropy in subduction zones .....

Abstract .....	99
4.1. Introduction.....	101
4.2. Geological setting and sample description.....	103
4.3. Method .....	113
4.3.1. Analysis of chemical composition of minerals .....	113
4.3.2. P-T pseudosection of sample .....	113

4.3.3. Determination of foliation, lineation, and grain sizes .....	114
4.3.4. Measurement of CPO.....	114
4.3.5. Calculation of misorientations .....	115
4.3.6. Calculation of seismic velocities and anisotropies .....	116
4.4. Results .....	117
4.4.1. Mineral chemistry .....	117
4.4.2. Pressure-temperature estimates.....	117
4.4.3. Microstructures of antigorite and diopside .....	120
4.4.4. CPO of antigorite and diopside.....	128
4.4.5. Misorientations of diopside and antigorite .....	132
4.4.6. Seismic velocities and anisotropies of diopside and antigorite...	136
4.5. Discussion .....	145
4.5.1. Serpentinization and grain size of diopside .....	145
4.5.2. Relationship between diopside CPO and antigorite CPO.....	146
4.5.3. Deformation mechanism of diopside and antigorite .....	150
4.5.4. Serpentinization and stability field of the samples in MSP area.	160
4.5.5. Implications of diopside and antigorite for seismic anisotropy in subduction zones .....	161
4.6. Conclusions .....	167
 CHAPTER 5. Summary and conclusion.....	 168

REFERENCES.....	170
국문 초록.....	199



## LIST OF FIGURES

**Figure 2.1.** Map showing sample locations and microphotographs of talc aggregates.

**Figure 2.2** Elastic anisotropy of single-crystal monoclinic talc at ambient pressure.

**Figure 2.3** Single-crystal elastic properties of composite mineral phases which were used for calculation of polycrystal seismic properties.

**Figure 2.4.** Pole figures of polycrystalline talc in each sample. **(a, b and c)** Samples from UHP Makbal Complex. **(d, e)** Samples from Valla Complex in Unst.

**Figure 2.5.** Pole figures of CPO of composite minerals (garnet, quartz, chlorite, tremolite, phengite and chloritoid) in studied samples.

**Figure 2.6.** P–wave velocity, P–wave azimuthal anisotropy, S–wave anisotropy and fast S–wave polarization direction of polycrystalline talc in each sample **(a – e)**. **(a, b and c)** Samples from UHP Makbal Complex. **(d, e)** Samples from Valla Complex in Unst.

**Figure 2.7.** P–wave velocity and P–wave seismic anisotropy ( $AV_P$  in %) of each polycrystalline mineral and whole rock of the five rock samples analyzed in this study.

**Figure 2.8.** Comparison of the P–wave anisotropy of talc aggregates with that of other polycrystalline minerals.

**Figure 2.9.** S-wave seismic anisotropy ( $AV_s$  in %) and fast S-wave ( $V_{s1}$ ) polarization directions of each polycrystalline mineral and whole rock of the five rock samples analyzed in this study.

**Figure 2.10.** Seismic properties of polycrystalline talc at a high pressure of  $P = 2.9$  GPa.

**Figure 2.11.** Images of P-wave radial anisotropy in the Japan subduction zone.

**Figure 2.12.** P-wave anisotropy and S-wave anisotropy of polycrystalline talc with changes in the dip-angle of slab, and the thickness of anisotropic layer of talc as a function of delay time.

**Figure 2.13.** Variations of  $V_{ph}$ ,  $V_{pv}$ , and RA of polycrystalline talc at  $P = 2.9$  GPa with increasing slab dip-angle.

**Figure 3.1** Hand specimen **(a, c, e)** and plane-polarized microphotographs **(b, d, f)** of UHP Makbal garnet-chloritoid-talc schist samples.

**Figure 3.2** Undulose extinction of chloritoid in sample #10-16.

**Figure 3.3** Elastic anisotropy of single-crystal monoclinic chloritoid at a pressure of 0 GPa.

**Figure 3.4 (a)** P-T pseudosection calculated for an average composition of 18 published metapelites from Shaw (1956) in the model system NCKFMASH. **(b)** Modal volume percentages of chloritoid (vol.%).

**Figure 3.5 (a)** P-T pseudosection calculated for a Mg-Al metagabbro from Messiga et al. (1999) (sample MOE11B) in the model system NCFMASH. **(b)** Modal volume percentages of chloritoid (vol.%).

**Figure 3.6** Pole figures showing the CPO of chloritoid in the three UHP Makbal schist samples.

**Figure 3.7** Seismic anisotropies of polycrystalline chloritoid in the UHP Makbal schist samples.

**Figure 3.8** Bulk seismic anisotropy of the whole rock.

**Figure 3.9** P-T pseudosection showing the chloritoid-stability fields and the volume percentage isopleths of chloritoid.

**Figure 3.10 (a)** Schematic diagram illustrating a subducting slab with a dipping angle of  $60^\circ$ . **(b)** Pressure-temperature stability fields of hydrous phases in hydrated MORB under subduction zone conditions (modified after Schmidt and Poli, 1998). **(c)** Schematic diagram of a subduction zone illustrates the influence of the chloritoid CPO on the seismic anisotropy in the subduction zone.

**Figure 3.11** Illustration of the 3-D effect of chloritoid, talc and the Grt-Cld-Tlc schist on a vertically incident S-wave.

**Figure 3.12** Representation of the effect of the glaucophane, lawsonite, chlorite, phengite, and chloritoid on the delay time and fast S-wave polarization

direction of a vertically incident S wave, and that of the bulk seismic anisotropy of a hypothetical blueschist.

**Figure 4.1.** Maps showing the sample location of diopside serpentinites.

**Figure 4.2.** Microphotographs of Corsica diopside-bearing serpentinite samples.

**Figure 4.3.** Raman spectra of serpentine grains in the MSP diopside serpentinite samples (3096core, 3096D, 3096F and 3096A).

**Figure 4.4. (a)** P-T pseudosection for the serpentinite (bulk-rock composition of sample 3096core). **(b)** Volume fraction of diopside in the same bulk composition used in **(a)**.

**Figure 4.5.** Representative grain shapes of diopside and antigorite in serpentinite samples (sample 3096A).

**Figure 4.6. (a1, b1)** GOS maps of antigorite in a **(a1)** weakly foliated area (WFA) and **(b1)** strongly foliated area (SFA) obtained from EBSD mapping (sample 3096core) overlaying the gray-scaled band contrast map. **(a2, b2)** CPOs and inverse pole figures of antigorite in the **(a2)** WFA and **(b2)** SFA. **(a3, b3)** Histograms for GOS distribution of antigorite in the **(a3)** WFA and **(b3)** SFA. **(a4, b4)** Subgrain rotation axes (subgrain boundaries with misorientation angles of 2 – 10 degrees) of antigorite in the **(a4)** WFA and **(b4)** SFA.

**Figure 4.7.** (a1, b1) GOS maps of diopside in a (a1) weakly foliated area (WFA) and (b1) strongly foliated area (SFA) (sample 3096core) overlaying the gray-scaled band contrast map. (a2, b2) CPOs and inverse pole figures of diopside in the (a2) WFA and (b2) SFA. (a3, b3) Histograms for GOS distribution of diopside in the (a3) WFA and (b3) SFA. (a4, b4) Subgrain rotation axes (subgrain boundaries with misorientation angles of 2 – 10 degrees) of diopside in the (a4) WFA and (b4) SFA.

**Figure 4.8.** Large-area CPOs of antigorite and diopside at thin section scale in serpentinite samples.

**Figure 4.9.** Grain reference orientation deviation (GROD) angle maps of diopside and antigorite grains.

**Figure 4.10.** (a, b) Representative GOS maps of (a) diopside and (b) antigorite in the WFA (sample 3096core).

**Figure 4.11** (a – c) Seismic velocities and seismic anisotropies of (a) antigorite, (b) diopside and (c) bulk rock (whole rock) of the MSP diopside serpentinite samples.

**Figure 4.12.** Comparison of seismic properties of antigorite aggregates (sample 3096core) using the antigorite single-crystal elastic constants of Bezacier et al. (2010a) and Satta et al. (2022).

**Figure 4.13. (a, b)** Orientation maps (inverse pole figure color-coded, direction of view normal to the screen) and pole figures for antigorite (Atg) and diopside (Di).

**Figure 4.14.** The 3-dimensional seismic properties of antigorite and diopside CPO on delay time between fast S-wave and slow S-wave (Delay time), fast S-wave polarization direction (Vs1 pol.) and the ratio between P-wave velocity and fast S-wave velocity (Vp/Vs ratio) using representative large area CPO data (sample 3096core).

**Figure 4.15.** The 3-dimensional seismic properties of olivine, diopside and antigorite CPO on delay time, Vs1 polarization directions, and Vp/Vs ratio.

## LIST OF TABLES

**Table 2.1.** Modal compositions (in % of volume) of samples.

**Table 2.2.** P-wave anisotropy ( $AV_P$  in %), S-wave anisotropy ( $AV_S$  in %) and CPO strength of the polycrystalline minerals composing the studied samples and those of the whole rock samples.

**Table 3.1** Elastic stiffness tensor of single crystal chloritoid using the GGA method and the LDA method.

**Table 3.2** Seismic velocity and anisotropy of hydrous minerals and a hypothetical bulk rock.

**Table 4.1.** Summary of sample description (mineral volume percentage and average grain size), large-area CPO type, and CPO strength (M-index) of antigorite and diopside in MSP serpentinite samples.

**Table 4.2.** Chemical composition of bulk rock, diopside and antigorite in four serpentinite samples from Monte San Petrone area.

**Table 4.3.** Summary of seismic anisotropies of antigorite, diopside and bulk rocks of the serpentinite samples.

## LIST OF PUBLICATIONS

- D. Kim, H. Jung, and **J. Lee**. (2023). Impact of dehydration on chlorite and intermediate-depth earthquakes, *Communications Earth & Environment*, under review.
- J. Lee**, M. Mookherjee, T. Kim, H. Jung, and R. Klemm. (2021). Seismic anisotropy in subduction zones: evaluating the role of chloritoid, *Frontiers in Earth Science*, 9, 644958.
- D. Kim, H. Jung, and **J. Lee**. (2020). Strain-induced fabric transition of chlorite and implications for seismic anisotropy in subduction zones, *Minerals*, 10, 503.
- J. Lee**, H. Jung, R. Klemm, M. S. Tarling, and D. Konopelko (2020). Lattice preferred orientation of talc and implications for seismic anisotropy in subduction zones. *Earth and Planetary Science Letter*. 537, 116178.
- I. Moon, I. Lee, **J. Lee**, H. Jung, and X. Yang. (2018). Interpretation of formation condition in Superior-type banded iron formation (BIF) of Yuanjiacun in North China Craton using magnetite, *Journal of the Geological Society of Korea*, 54, 281-291.



# CHAPTER 1. Introduction

Seismic anisotropy has been observed in worldwide subduction zones and it can provide important information for understanding internal structures of the Earth (Long and Silver, 2008; Savage, 1999; Uchida et al., 2020). Crystallographic preferred orientations (CPOs) of minerals, which is a deformation microstructure of rock-forming minerals, can act as anisotropic mediums to cause the seismic anisotropy in subduction zones (Almqvist and Mainprice, 2017; Jung, 2017; Mainprice and Ildefonse, 2009). There have been a lot of previous studies to correlate the seismic anisotropy with the CPO of olivine, due to its volumetric abundance in the upper mantle (Jung and Karato, 2001; Michibayashi et al., 2016; Skemer and Hansen, 2016). However, strong seismic anisotropy (long delay time of S-wave), observed in some subduction zones cannot be fully explained by olivine-dominant lithologies alone.

As the subduction zone interiors are actively hydrated by the subduction of oceanic plate, CPOs of hydrous minerals, which single crystal is elastically anisotropic, are thought to be responsible to cause the high seismic anisotropy in subduction zones (Jung, 2017; Mainprice and Ildefonse, 2009; Morales et al., 2013). One of the most abundant hydrous minerals in subduction zones is serpentine, which is known to be elastically anisotropic (Brownlee et al., 2013; Jung, 2011; Katayama et al., 2009; Mookherjee and Capitani, 2011; Watanabe et al., 2014). However, the mechanism of the CPO formation of serpentine in subduction zones is still controversial. Additionally, there are still hydrous minerals which CPO and elastic

properties have been lack of study, such as talc and chloritoid. Talc is one of the important hydrous minerals in mantle wedge and subducting slab and known to be elastically very anisotropic (Kim et al., 2013; Mainprice et al., 2008; Peng et al., 2022; Spandler et al., 2008). Chloritoid is one of the representative hydrous minerals present in subducting metapelites and metagabbro (Ghent et al., 1987; Grevel et al., 2005; Messiga et al., 1995), however there has been no report on its elastic properties.

In Chapter 2, the CPO of talc and the CPO-induced seismic anisotropy of talc were studied. CPO measurement of talc has been considered to be difficult as talc is mechanically very weak. By carefully polishing the thin-section surface, I successfully measured the CPO of talc using electron back-scattered diffraction (EBSD). The analyzed rock samples are garnet-chloritoid-talc schist from the Makbal ultrahigh-pressure complex (Kyrgyzstan) and talc schists from the Unst Island (Scotland). The CPO of talc shows a strong alignment of (001) plane subparallel or parallel to the foliation of the rock samples. The seismic anisotropy of talc was also calculated. The results imply that the CPO of talc influence both the strong trench-parallel azimuthal anisotropy and positive/negative radial anisotropy of P-waves, and the trench-parallel seismic anisotropy of S-waves in these subduction zones.

In Chapter 3, the single-crystal elastic anisotropy of chloritoid and the CPO of polycrystalline chloritoid were studied. Chloritoid is one of the metamorphic indicator minerals for high- to ultrahigh-pressure metamorphic conditions (from greenschist facies to eclogite facies) relevant for subduction zone settings (e.g. Kienast and Messiga, 1987; Meyer et al., 2014; Negulescu et al., 2009; Smye et al.,

2010; Wei and Song, 2008), and previous studies of chloritoid-bearing rocks reported on chloritoid modal amount of 10–23 vol% (e.g. Haerinck et al., 2013; Regis et al., 2014). The analyzed rock samples in this chapter are garnet-chloritoid-talc schist from the Makbal ultrahigh-pressure complex (Kyrgyzstan) (in Chapter 2). New elasticity data of single-crystal chloritoid showed a strong elastic anisotropy of chloritoid and contributed to acquire the complete bulk seismic anisotropy of the samples. The CPO of chloritoid displayed a strong alignment of the [001] axes subnormal to the rock foliation, with a girdle distribution of the [100] axes and the (010) poles subparallel to the foliation. Combining the CPO results of chloritoid and the re-evaluated thermodynamic stability field of chloritoid indicate that the strong CPO of chloritoid along the subduction interface and in subducting slabs can influence the trench-parallel seismic anisotropy in subduction zones with “cold” geotherms.

In Chapter 4, serpentine CPOs in diopside serpentinites were studied to find a possible deformation mechanism of antigorite associated with diopside pyroxene, and to understand their impact on seismic anisotropy in subduction zones. The antigorite CPOs have been widely reported in nature (Bezacier et al., 2010a; Brownlee et al., 2013; Jung, 2011, 2017; Katayama et al., 2009; Liu et al., 2020b), however their deformation mechanisms are still controversial. In this study, the antigorite CPO showed strong maxima of [001] axes normal/subnormal to the foliation with a weak girdle parallel to the foliation, and diopside CPO showed strong maxima of [100] axes normal/subnormal to the foliation with a weak girdle parallel to the foliation. The CPO results suggested that the CPO formation of antigorite can

be influenced by a topotactic growth of serpentine from diopside. The CPO-induced seismic properties of antigorite showed that syn-kinematic serpentinization in mantle wedge would be important for strong trench-parallel seismic anisotropies and high  $V_p/V_s$  ratio observed in cold subduction zones. It was also found that the strong diopside CPO in the foliated serpentinites would decrease the delay time of S-wave.

## **CHAPTER 2. Crystallographic preferred orientation of talc and implications for seismic anisotropy in subduction zones**

\* This chapter has been modified from a published paper:

J. Lee, H. Jung, R. Klemm, M. S. Tarling, and D. Konopelko (2020). Lattice preferred orientation of talc and implications for seismic anisotropy in subduction zones. *Earth and Planetary Science Letter*. 537, 116178.

### **Abstract**

Strong seismic anisotropy is generally observed in subduction zones. Crystallographic preferred orientation (CPO) of olivine and elastically anisotropic hydrous minerals has been considered as an important factor causing anomalous seismic anisotropy. In this chapter, I reported on measured CPOs of polycrystalline talc. The study comprises subduction-related ultra-high-pressure metamorphic schists from the Makbal Complex in Kyrgyzstan-Kazakhstan and amphibolite-facies metasomatic schists from the Valla Field Block in Unst, Scotland. The here studied talc revealed a strong alignment of (001) planes (sub)parallel to the foliation and a girdle distribution of [100] axes and (010) poles (sub)parallel to the foliation. The CPOs of polycrystalline talc produced a significant P-wave anisotropy ( $AV_p = 72\%$ )

and a high maximum S-wave anisotropy ( $\max AV_s = 24 \%$ ). The results imply that the CPO of talc influence both the strong trench-parallel azimuthal anisotropy and positive/negative radial anisotropy of P-waves, and the trench-parallel seismic anisotropy of S-waves in these subduction zones.

**Keywords:** talc, CPO, seismic anisotropy, P-wave anisotropy, subduction zone.

## 2.1 Introduction

Numerous studies have established a correlation between seismic anisotropy, which has been observed in many subduction zones (Long and Silver, 2008; Savage, 1999; Zhao et al., 2016), and the crystallographic preferred orientation (CPO) of elastically anisotropic minerals in the mantle wedge, subducting slab, and the overriding crust (Almqvist and Mainprice, 2017; Jung, 2017; Karato et al., 2008; Lloyd et al., 2009; Mainprice and Ildefonse, 2009). Strong P-wave anisotropy, which occurs in both the mantle wedge and the subducting slab, is interpreted to be due to upwelling flow in the mantle wedge, fossil anisotropy of a slab formed in a mid-ocean ridge environment, and/or olivine CPO transitions (Niu et al., 2016; Wang et al., 2019). The CPO of olivine has been suggested as a possible primary cause for the P-wave radial anisotropy (Wang et al., 2019; Zhao et al., 2016) in the slab and trench-parallel S-wave anisotropy in many subduction zones (Jung and Karato, 2001; Karato et al., 2008; Skemer and Hansen, 2016), while the CPOs of hydrous minerals, which are elastically very anisotropic media, have recently been proposed as the possible cause of the anomalous seismic anisotropy (Jung, 2011; Kang and Jung, 2019; Katayama et al., 2009; Mainprice and Ildefonse, 2009; Watanabe et al., 2014). However, up to now the CPO of talc has not been studied, even though talc is one of the most important hydrous phases in the hydrated mantle wedge, the subducting slab, and the slab-mantle interface (Hacker et al., 2003; Mainprice and Ildefonse, 2009). This is probably due to the difficult sample preparation for the talc CPO measurement.

Talc is one of the mechanically weakest minerals on Earth (Escartín et al., 2008) and has been reported to occur significantly in tectonically weak zones such as active slip faults (e.g. the San Andreas Fault; Moore and Rymer, 2007) and (ultra)high-pressure metasomatic mélanges along with slab-mantle interfaces (Spandler et al., 2008). Talc is found to be stable over a very wide spatial range from abyssal oceanic crust to deep subduction zones (Poli and Schmidt, 1997), and can represent up to 41 vol.% of the altered harzburgite being associated with the alteration of orthopyroxene to talc (Hacker et al., 2003). In addition, geophysical evidence suggests that the presence of talc in the slab and the lower part of the mantle wedge is the cause of low-velocities in the mantle wedge (Kim et al., 2013) and slab-mantle decoupling (Hirauchi et al., 2013). In the slab and slab-mantle interfaces, talc can be formed by the following processes: (1) silica-metasomatism by rising fluids along the slab-mantle interface (Hirauchi et al., 2013), (2) mechanical mixing of the mantle with siliceous sediments (Spandler et al., 2008), and/or (3) dehydration of serpentinite and serpentinization-related faults in the subducting slab where serpentine is also an important hydrous mineral (Faccenda et al., 2008). The deepest occurrence of talc was reported for the subduction-related Dora Maira UHP massif at peak metamorphic pressure conditions of  $P = 3.0$  GPa suggesting a depth of  $> 100$  km (Chopin, 1984). Furthermore, laboratory measurements show that talc is stable up to pressures of  $P = 5.0$  GPa (ca. 150 km depth) before its breakdown to the  $10\text{\AA}$  phase (Pawley and Wood, 1995).

Here I measured the CPOs of talc in talc-rich schist samples collected from metasomatic and ultrahigh-pressure metamorphic complexes, using scanning



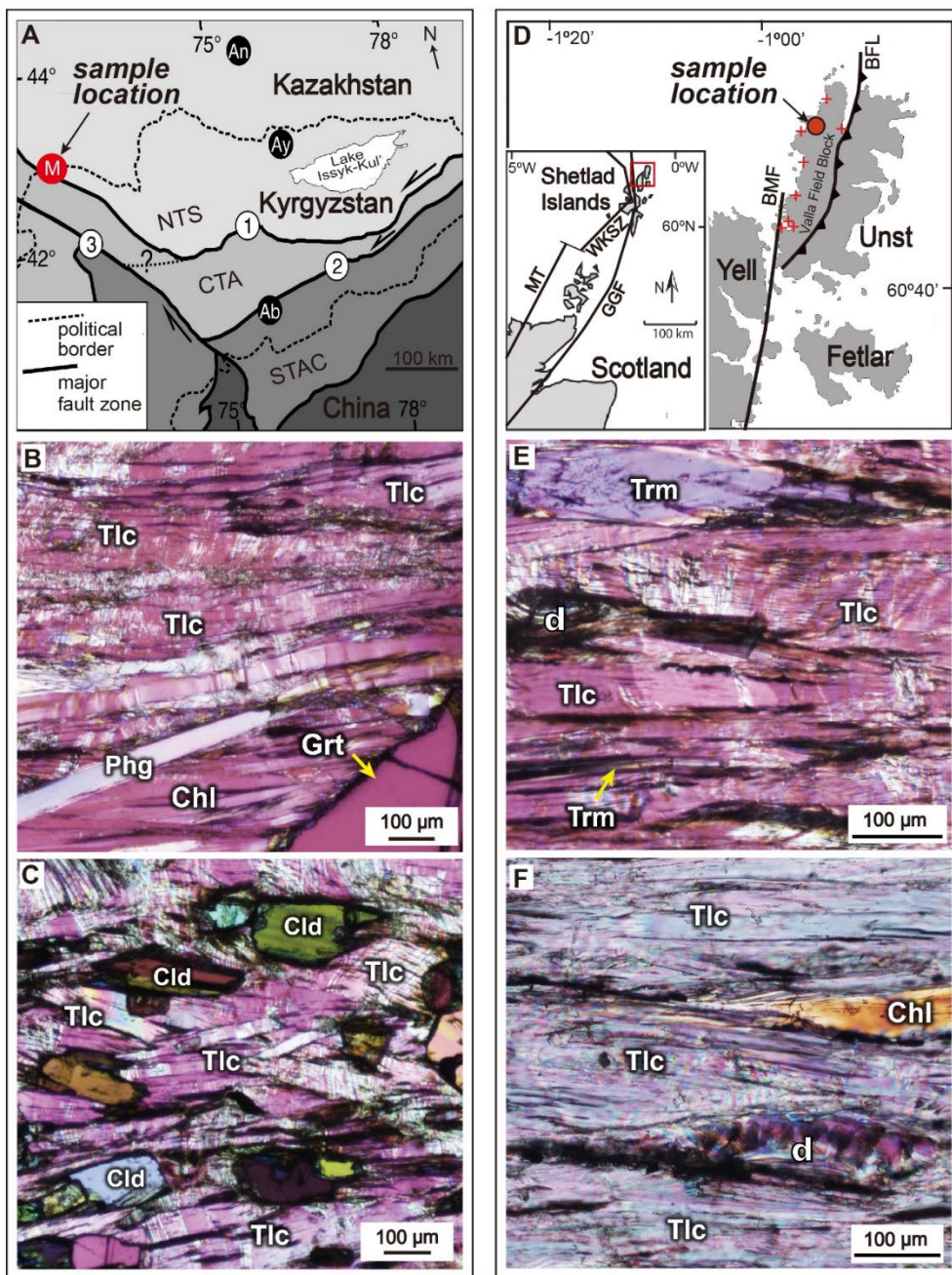
electron microscopy (SEM) with electron backscattered diffraction (EBSD). For the first time, the results showed a strong CPO of talc, and thus provide evidence for its significant contribution to radial and azimuthal P-wave anisotropy and trench-parallel S-wave seismic anisotropy in subduction zones.

## **2.2 Materials and Method**

### **2.2.1 Geological settings of rock specimens and sample description**

Rock samples were collected from two locations, the Makbal UHP Complex (Kazakhstan-Kyrgyzstan) and the Valla Field Block in Unst (Shetland Islands, Scotland). The Makbal Complex is a high- to ultrahigh-pressure (UHP) metamorphic complex located in the Kyrgyzstan Northern Tianshan orogenic belt on both sides of the Kazakhstan-Kyrgyzstan border (**Fig. 2.1a**), which is believed to be part of a UHP tectonic mélange comprising UHP Grt-Cld-Tlc schists, quartzites, metapelites and exotic blueschist-eclogite blocks (Meyer et al., 2014). The Makbal Complex comprises an area of  $\sim 12 \times 25$  km, in which (U)HP talc-bearing schists occur widespread, forming zones hundreds of meters wide within the UHP area (ca. 10 km in diameter). The UHP Grt-Cld-Tlc schists occur as up to 200 m thick layers in the central zone of the Makbal Complex (see Meyer et al., 2014 and references therein). Meyer et al. (2014) showed that the potential protolith of the UHP schists

is considered as a highly altered oceanic crust or pelitic sediments, and thermodynamic modelling has constrained peak metamorphic conditions of ca. 2.85 GPa at ca. 580 °C using the equilibrium peak mineral assemblage of talc + chloritoid + garnet + phengite + coesite + rutile. These conditions imply, as suggested by Meyer et al. (2014), a continental-type subduction along a cold geotherm at depths of up to 110 km and buoyancy-driven exhumation by low-density minerals such as talc and mica. Three Grt-Cld-Tlc schist samples (15R, 10–16 and 12–52), showing a distinct schistosity, were selected for CPO analysis of talc grains. Modal compositions of the samples are shown in **Table 2.1**.



(Caption in the next page)

**Figure 2.1.** Map showing sample locations and microphotographs of talc aggregates.

**(a)** Map showing sample locations of Makbal UHP talc schists and the surrounding tectonic units (NTS, Northern Tianshan; CTA, Central Tianshan Arc Terrane; STAC, Southern Tianshan Accretionary Complex). Ultrahigh-pressure (UHP) metamorphic complexes in the Tianshan orogen are labeled as follows: Makbal (M), Aktyuz (Ay), Atbashi (Ab), and Anrakhai (An) (Meyer et al., 2014). **(b, c)** Microphotograph of the ultramafic schist samples 10–16 **(b)** 12–52 **(c)**, showing well-elongated talc grains subparallel to the lineation (horizontal direction), under cross-polarized light. In **(b)**, the middle-located talc grains indicate the C-plane of the S–C fabric in sample 10–16. Tlc, talc; Phg, phengite, Chl, chlorite; Grt, garnet; and Cld, chloritoid. **(d)** Map showing sample location of Unst metasomatic talc schists illustrating tectonic lines. GGF, Great Glen Fault; MT, Moine Thrust; WKSZ, Wester Keolka Shear Zone; BMF, Bluemull Fault; and BFL, Burra Firth Lineament (Cutts et al., 2011). Red crosses indicate main localities of the metasomatic bodies in the Valla Field Block (Read, 1934). **(e, f)** Microphotographs of the Unst metasomatic schist samples UN04 **(e)** and UN22 **(f)**, showing well-elongated talc grains parallel to the lineation (horizontal direction) under cross-polarized light. Sample UN04 is a talc-tremolite schist and UN22 is a talc-chlorite schist. Tlc, talc; Trm, tremolite; Chl, chlorite; and d, depression in a weak talc grain.

**Table 2.1.** Modal compositions (in % of volume) of samples.

<i>Sample</i>	<i>15R</i>	<i>10-16</i>	<i>12-52</i>	<i>UN04</i>	<i>UN22</i>
<i>Mineral</i>	(vol.%)				
<i>Talc</i>	25	40	20	70	80
<i>Garnet</i>	10	25	35		
<i>Chloritoid</i>	10	20	25		
<i>Quartz</i>	15	3	17		
<i>Phengite</i>	10	7	1		
<i>Chlorite</i>	30	5	2		20
<i>Tremolite</i>				30	

Porphyroblastic garnet is embedded in a groundmass of talc + chloritoid  $\pm$  phengite  $\pm$  chlorite  $\pm$  quartz  $\pm$  rutile, and accessory apatite. The schistosity is defined by parallel crystals of talc and phengite, which showed a non-layered homogeneous distribution. Lepidoblastic talc has average grain lengths of 1.6, 1.8 and  $\sim$ 0.5 mm in samples 15R, 10–16 and 12–52 respectively. Talc grains in samples 15R and 10-16 are intimately intergrown with phengite and both of which replace chloritoid. They are elongated parallel and/or subparallel along the lineation, related to the S–C fabric (**Fig. 2.1b**). Sample 12–52 comprises a relatively homogeneous distribution of talc associated with fine-grained chloritoid grains (**Fig. 2.1c**). Undulose extinction and microkinks in talc grains commonly occur in the three samples.

Talc-rich metasomatic bodies occur in the basement of the Valla Field Block tectonic unit located in the western part of Unst Island (**Fig. 2.1d**), separated from the Shetland Ophiolite Complex by the Burra Firth Lineament. The Valla Field Block is mainly composed of pre-Caledonian gneisses, mostly of sedimentary origin, and the talc-rich metasomatic bodies are hosted by the Westing Group in the southwestern part of the complex (Read, 1934). Main localities of the talc-rich metasomatic bodies occur widespread along the 16–km long shore of the western Unst Island, as roughly spherical balls or lenses being up to 20 meters in diameter (Read, 1934), and the talc layers associated with these zoned metasomatic bodies are on the order of 10 cm to 1 m thick. These bodies often occur as talc-tremolite and talc-chlorite schists, forming a reaction zone between the serpentinite and the pelitic country rock due to metasomatic fluid-rock interaction. The bodies often have a central serpentinite core that is surrounded by a talc-rich margin followed by layers

of tremolite amphibole, chlorite, and biotite (Read, 1934). This type of mineral zoning of ultramafic bodies is similar to that of metasomatic ultramafic bodies from the slab-mantle interface (Spandler et al., 2008). The occurrence of talc with tremolite and/or chlorite has been interpreted to be due to the metasomatic circulation of Si–Ca–Al-rich fluids channelized in the foliated serpentinites along the paleo-subduction interface (Guillot et al., 2009).

The samples UN04 and UN22 from Unst Island comprise ca. 70 vol.% talc and 30 vol.% tremolite, and 80 vol.% talc and 20 vol.% chlorite, respectively, with accessory chromite and magnetite. Modal compositions of the samples are shown in **Table 2.1**. Both samples show strong slaty cleavages defined by fine-grained talc, elongated tremolite and chlorite (**Figs. 2.1e and 2.1f**). In both samples, talc mainly forms the lineation.

### **2.2.2 Measurement of CPOs of minerals**

The foliation of the UHP Makbal schists and Valla Field Block metasomatic schists was determined by examining the shape preferred orientation of minerals such as talc and phengite mica. The lineation was defined by analyzing the elongation of minerals within the foliation plane. They were cut parallel to the X–Z plane (where X is parallel to the lineation and Z is normal to the foliation). In order to prevent any severe loss of weak talc crystals, each specimen was carefully coated with epoxy bond prior to cutting and polishing. Thin sections were mechanically and chemically polished using Syton (colloidal silica) for 6 h, and coated by carbon with

a minimum thickness to prevent electric charging. The CPOs of polycrystalline talc and the other major composite minerals were determined using the EBSD in the JEOL JSM-6380 SEM at the School of Earth and Environmental Sciences at the Seoul National University. The SEM was operated at an accelerating voltage of 20 kV and a working distance of 15 mm. The EBSD patterns were indexed manually, because it was difficult to constrain the relatively weak Kikuchi bands of talc compared to other composite minerals such as phengite and chlorite using the automatic mapping method. I employed the HKL Channel 5 software and the crystal symmetry parameters of monoclinic talc (Mainprice et al., 2008). For a better data quality, CPO of talc was measured with a mean angular deviation less than  $0.8^\circ$  and a minimum of 11 diffraction Kikuchi bands for each point measurement. Each point of measurement corresponds to a single grain except in the case of large garnet porphyroblasts in the UHP rock samples. Because of the large size of garnet porphyroblasts and small number of grains in the UHP rock samples, CPOs of garnet were obtained from tens of EBSD points in individual grains.

### **2.2.3 Calculation of seismic anisotropy of polycrystalline talc**

The seismic anisotropy of talc was obtained using the MTEX and MSAT toolkits (Mainprice et al., 2014; Walker and Wookey, 2012). The essential parameters used for calculations include the single-crystal elastic constants ( $C_{ij}$ ), mineral density ( $2.76 \text{ g/cm}^3$  of talc), mineral modal abundances, and CPOs of individual grains. Single-crystal elastic properties of talc are highly dependent on the symmetry



system (triclinic talc or monoclinic talc) (Mainprice et al., 2008). The indexed EBSD patterns of talc were consistent with monoclinic crystal symmetry, and this was used to determine the CPO of polycrystalline talc. P-wave azimuthal anisotropy ( $AV_P$ ) was calculated as

$$AV_P (\%) = \frac{(V_{Pmax} - V_{Pmin})}{(V_{Pmax} + V_{Pmin})/2} \times 100,$$

and P-wave radial anisotropy (RA) was calculated as

$$RA (\%) = \frac{(V_{Ph} - V_{Pv})}{(V_{Ph} + V_{Pv})/2} \times 100,$$

where  $V_{Ph}$  is the average velocity of horizontally propagating P-waves (4 orthogonal directions on a horizontal plane) and  $V_{Pv}$  is the vertically propagating P-wave velocity (Ishise et al., 2018). The S-wave anisotropy was calculated as

$$AV_S (\%) = \frac{(V_{S1} - V_{S2})}{(V_{S1} + V_{S2})/2} \times 100,$$

where  $V_{S1}$  and  $V_{S2}$  represent the fast and slow S-wave velocity, respectively. The single-crystal elastic anisotropy of talc ( $AV_P = 76\%$  and  $\max AV_S = 32\%$  for monoclinic talc at  $P = 0$  GPa), which is extremely high, is shown in **Figure. 2.2**. These zero-pressure elastic properties ( $C_{ij}$  at  $P = 0$  GPa) were used for most of the following calculations related to polycrystalline talc and the bulk rock seismic anisotropy, in order to compare the data of talc and that of other minerals at the same pressure condition. Therefore, zero-pressure (ambient pressure) elastic anisotropy of other composite minerals were used for the bulk rock seismic anisotropy and the comparison of S-wave delay time (**Fig. 2.3**). Elastic data for single chloritoid crystal

has not been published. The elastic anisotropy of talc at an ultra-high pressure  $P = 2.9$  GPa is also shown in **Fig. 2.3**.

## 2.3 Results

Five rock samples were collected from two locations, the Makbal UHP Complex in Kazakhstan-Kyrgyzstan and the Valla Field Block in Unst in Shetland Islands, Scotland. Three samples 15R, 10–16 and 12–52 are ultrahigh-pressure (UHP) Grt-Cld-Tlc schists from the Makbal UHP Complex (**Fig. 2.1a**). Talc grains in samples 15R and 10-16 are elongated parallel and/or subparallel to the lineation, related to the S–C fabric (**Fig. 2.1b**). Sample 12–52 comprises a relatively homogeneous distribution of talc associated with fine-grained chloritoid grains (**Fig. 2.1c**). Samples UN04 and UN22 are metasomatic talc-rich schists from the Valla Field Block (**Fig. 2.1d**), which contain talc and other major minerals such as tremolite in sample UN04 and chlorite in sample UN22. Both samples show strong slaty cleavages defined by fine-grained, lepidoblastic talc and strongly oriented tremolite and chlorite (**Figs. 2.1e and 2.1f**). Modal compositions of the five samples are shown in **Table 2.1**. Detailed rock descriptions and geological settings are provided in **Section 2.2.1**.

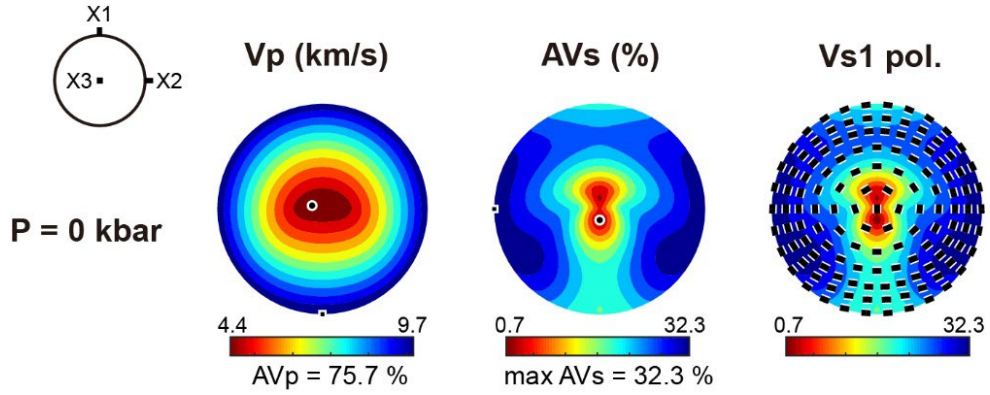
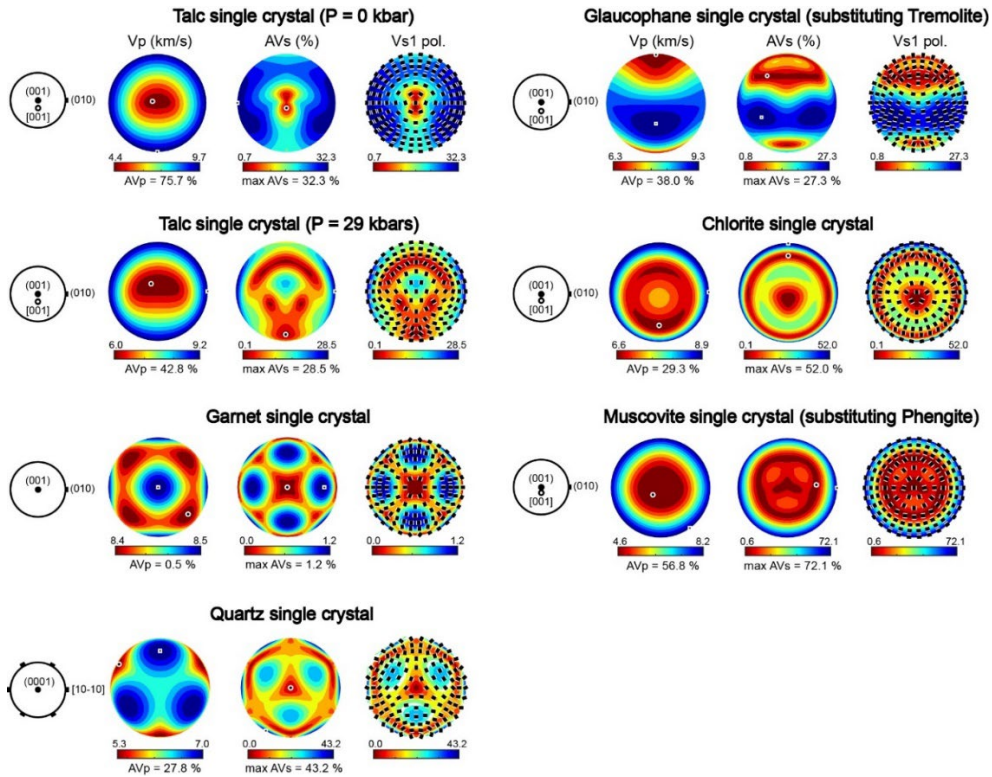


**Figure 2.2** Elastic anisotropy of single-crystal monoclinic talc at ambient pressure, which was obtained using elastic constants, crystal structure parameters, and the density of talc (Mainprice et al., 2008). Seismic velocity and anisotropy are shown in the lower hemisphere using equal-area projection. The P–wave anisotropy is very high ( $AV_P = 75.7\%$ ) and S–wave anisotropy is relatively high ( $AV_S = 32.3\%$ ). Polarization directions of fast S–wave ( $V_{S1}$  pol.) are shown as black bars. A reference frame for monoclinic symmetry is shown on the left and depicts three orthogonal axes X1, X2 and X3, where X2 is parallel to the crystallographic b-axis while the plane normal to the b-axis is a mirror plane containing X1 and X3 (where X1 corresponds to the crystallographic a-axis and X3 is perpendicular to the (001) basal plane (X1–X2 plane)).



(Caption in the next page)

**Figure 2.3** Single-crystal elastic properties of composite mineral phases which were used for calculation of polycrystal seismic properties (**Figs. 2.7 and 2.8**). Elastic velocity and anisotropy are shown in the lower hemisphere using equal-area projection. Reference frame  $V_P$  (km/s): P-wave velocity,  $AV_P$  (%): P-wave anisotropy,  $AV_S$  (%): S-wave anisotropy,  $V_{S1}$  pol.: fast S-wave polarization direction. Polarization directions of fast S-waves ( $V_{S1}$  pol.) are shown as black bars. Reference frames are shown on the left of each projection. For monoclinic and cubic symmetries, (001) pole is horizontal, (001) poles is out of plane and [001] axis (c-axis) is also denoted. For a trigonal symmetry, (10-10) pole is horizontal and (0001) pole (c-axis) is out of plane. Elastic constants from references: talc single crystal (Mainprice et al., 2008), garnet single crystal (Babuška et al., 1978), quartz single crystal (Heyliger et al., 2003), glaucophane single crystal (Bezacier et al., 2010b), chlorite single crystal (Mookherjee and Mainprice, 2014) and muscovite single crystal (Vaughan and Guggenheim, 1986).

### 2.3.1 CPO of talc and other minerals

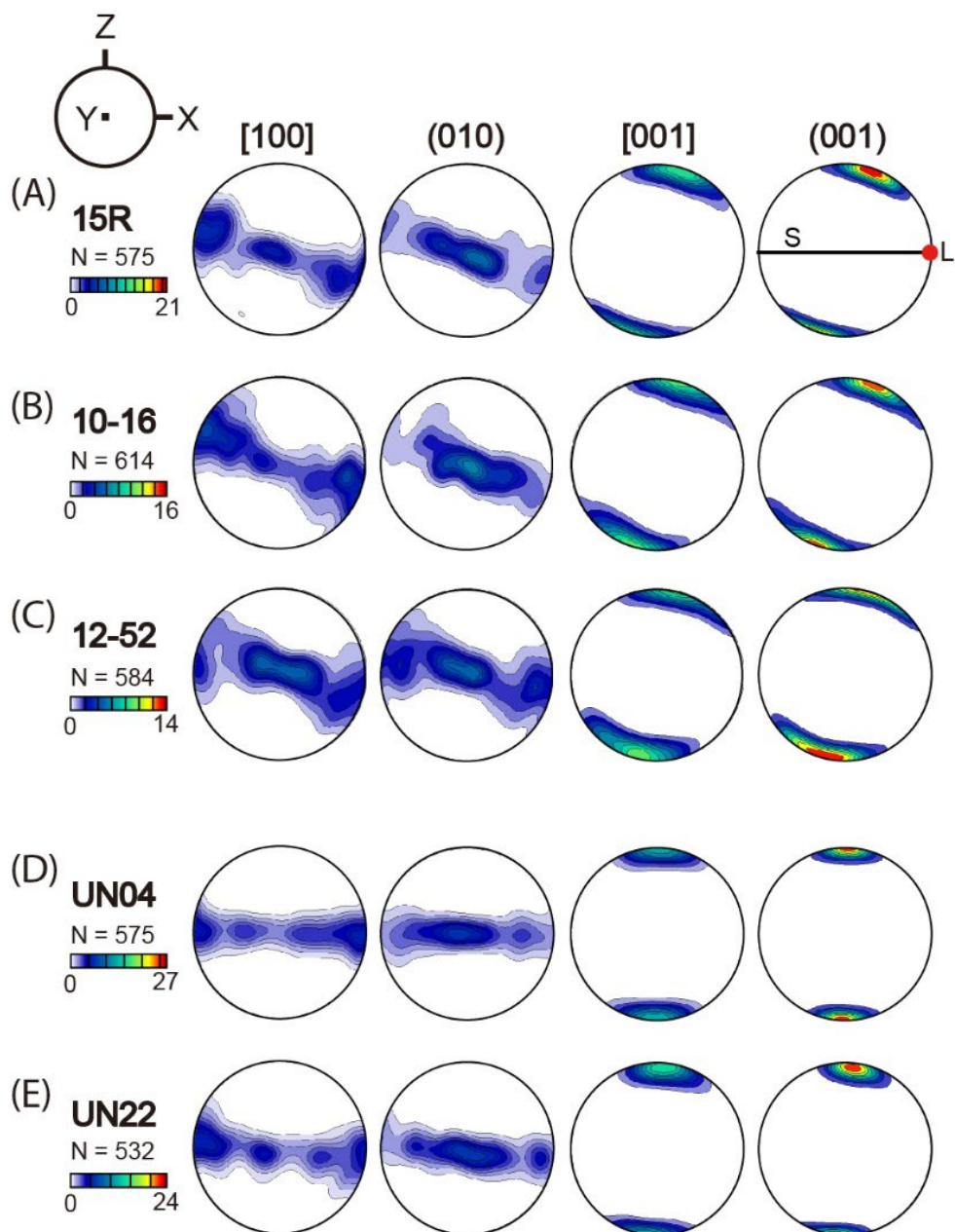
The CPO patterns of talc aggregates were determined via SEM/EBSD (see **Methods**) and are shown in **Figs. 2.4a – 2.4e**. The three Makbal Complex samples revealed [001] axes and (001) poles of talc that were strongly aligned subnormal to the foliation (C-plane of the S–C fabric) and normal to the S-plane which is disposed at 10 – 20 degrees to the foliation. Both [100] axes and (010) poles of talc exhibited a girdle distribution subparallel to the foliation. Two medium-grained samples (15R and 10–16) showed a maximum concentration of (010) poles subnormal to the lineation, while the other sample (12–52) showed a nearly uniform girdle distribution of (010) poles subparallel to the foliation.

The two metasomatic schist samples showed the highest degrees of alignment of (001) poles subnormal to the foliation (i.e., (001) planes subparallel to the foliation). Sample UN04 showed a nearly uniform girdle distribution of (010) poles parallel to the foliation, while sample UN22 revealed a maximum concentration of (010) poles normal to the lineation and parallel to the foliation.

The talc CPO, particularly the (001) poles, showed a strength of 14 – 21 multiples of random distribution (m.r.d.) for the UHP rock samples (**Figs. 2.4a – 2.4c**) and 24 – 27 m.r.d. for the metasomatic rock samples (**Figs. 2.4d and 2.4e, Table 2.2**).

The CPOs of other composite minerals are shown in **Figure. 2.5**. CPOs of chlorite (samples 15R, 10–16 and UN22) commonly showed strong maxima of (001) poles subnormal to the foliation, which were similar to those of talc. The CPOs of phengite (samples 15R and 10–16) showed similar distribution of (001) poles

subnormal to the foliation. An CPO of tremolite (sample UN04) showed a strong concentration of [001] axes parallel to the lineation and an alignment of [100] axes normal to the foliation. The CPOs of garnet porphyroblasts resulted in a random distribution. The CPOs of quartz were weak with some random concentrations of (0001) poles. The CPOs of chloritoid showed a strong alignment of [001] axes subnormal to the foliation.



(Caption in the next page)



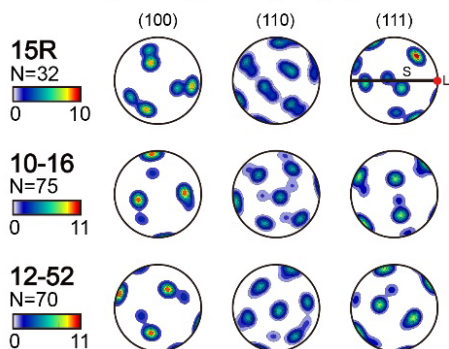
**Figure 2.4.** Pole figures of polycrystalline talc in each sample (**a – e**). (**a, b and c**) Samples from UHP Makbal Complex. (**d, e**) Samples from Valla Complex in Unst. Pole figures are presented in lower hemisphere using an equal-area projection. N represents the number of analyzed grains. Colorbars in the left side indicate CPO strengths of [100] axes, (010) poles, [001] axes and (001) poles of talc in units of multiples of random distribution (m.r.d.). X-direction is parallel to the lineation (L), Z-direction normal to the foliation (S), and Y-direction orthogonal to the X–Z plane.

**Table 2.2.** P–wave anisotropy ( $AV_P$  in %), S–wave anisotropy ( $AV_S$  in %) and CPO strength of the polycrystalline minerals composing the studied samples and those of the whole rock samples.

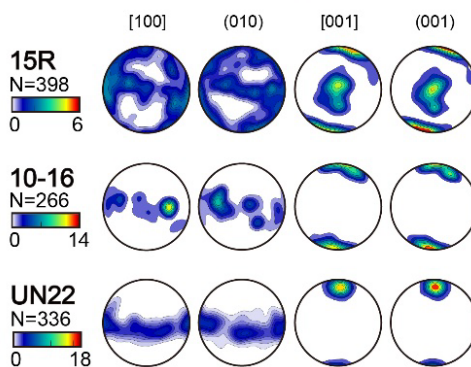
Sample	Mineral (or whole rock)	$AV_P$ (%)	$AV_S$ (%)	CPO strength (m.r.d.)
15R	Talc	72.3	23.3	21
	Garnet	0.4	0.9	10
	Quartz	3.3	4.9	3
	Phengite	34.1	35.3	11
	Chlorite	12.7	17.0	6
	Whole rock	23.9	15.2	
10-16	Talc	67.3	21.9	16
	Garnet	0.4	1.0	11
	Quartz	4.7	6.9	5
	Phengite	39.8	41.4	16
	Chlorite	20.8	33.7	14
	Whole rock	31.2	15.9	
12-52	Talc	69.3	21.5	14
	Garnet	0.4	0.9	11
	Quartz	3.0	3.8	5
	Whole rock	19.1	6.6	
UN04	Talc	71.1	23.8	27
	Tremolite	19.3	11.8	18
	Whole rock	51.4	18.2	
UN22	Talc	70.8	23.7	24
	Chlorite	20.7	35.1	18
	Whole rock	54.5	21.4	



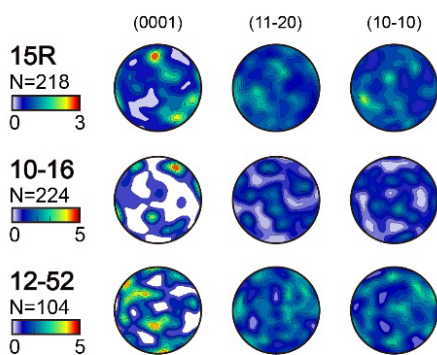
### Garnet pole figures (porphyroblasts)



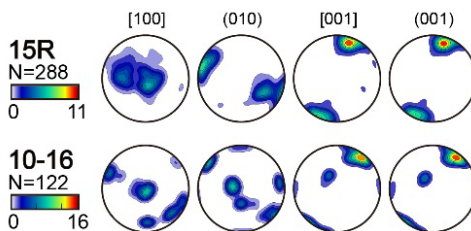
### Chlorite pole figures



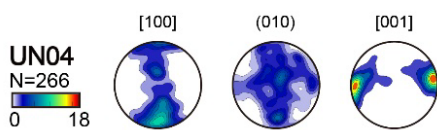
### Quartz pole figures



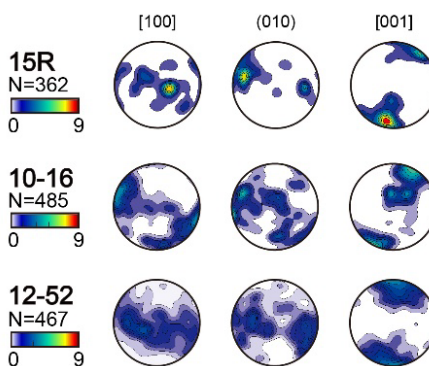
### Phengite pole figures



### Tremolite pole figures



### Chloritoid pole figures



(Caption in the next page)

**Figure 2.5.** Pole figures of CPO of composite minerals (garnet, quartz, chlorite, tremolite, phengite and chloritoid) in studied samples. Reference frame is the same as Fig. 2.2. Pole figures are presented in lower hemisphere using an equal-area projection. N represents the number of analyzed grains. Colorbars indicate CPO strength of each crystallographic axes. In all pole figures, S and L denote the foliation and lineation, respectively. Pole figure of chloritoid data was modified from Lee et al. (2021).

### 2.3.2 Seismic anisotropy of polycrystalline talc and whole rock

The seismic anisotropy of polycrystalline talc was calculated (**Fig. 2.6** and **Table 2.2**) using the CPOs and the single-crystal elastic constant ( $C_{ij}$ ) of talc. The magnitude of the P-wave azimuthal anisotropy ( $AV_P$  in %) of the polycrystalline talc was very high, ranging from 67 to 72 % for the three UHP schist samples (**Figs. 2.6a – 2.6c**) and approximately 71 % for the two metasomatic schist samples (**Figs. 2.6d and 2.6e**). The P-wave velocity ( $V_P$  in km/s) was lower in a seismic wave ray path of the direction subnormal (**Figs. 2.6a – 2.6c**) or normal to the foliation (**Figs. 2.6d and 2.6e**) with strongly aligned (001) poles of talc.

The P-wave azimuthal anisotropy of the other composite minerals in this study is shown in **Fig. 2.7**, which show that the P-wave azimuthal anisotropy of talc is larger than that of the other polycrystalline minerals in each respective rock sample. I also compared the P-wave azimuthal anisotropy of polycrystalline talc with that of olivine (Park and Jung, 2015), orthopyroxene (Jung et al., 2010), clinopyroxene (Park and Jung, 2015), glaucophane (Cao et al., 2013), omphacite (Cao et al., 2013; Kim et al., 2016), serpentine (Hirauchi et al., 2010; Jung, 2011; Watanabe et al., 2014), chlorite (Kim and Jung, 2015), and hornblende (Ji et al., 2013), all of which are important minerals in the upper mantle and the subducting slab (**Fig. 2.8**). I observed an exceptionally high P-wave azimuthal anisotropy of polycrystalline talc ( $AV_P = 67 - 72$  %) when compared to that of the other major minerals ( $AV_P = 2 - 31$  %) in the slab-mantle interface, approximately from 2 to 35 times higher. The maximum P-wave velocity of talc aggregates (this study) was also very high (max

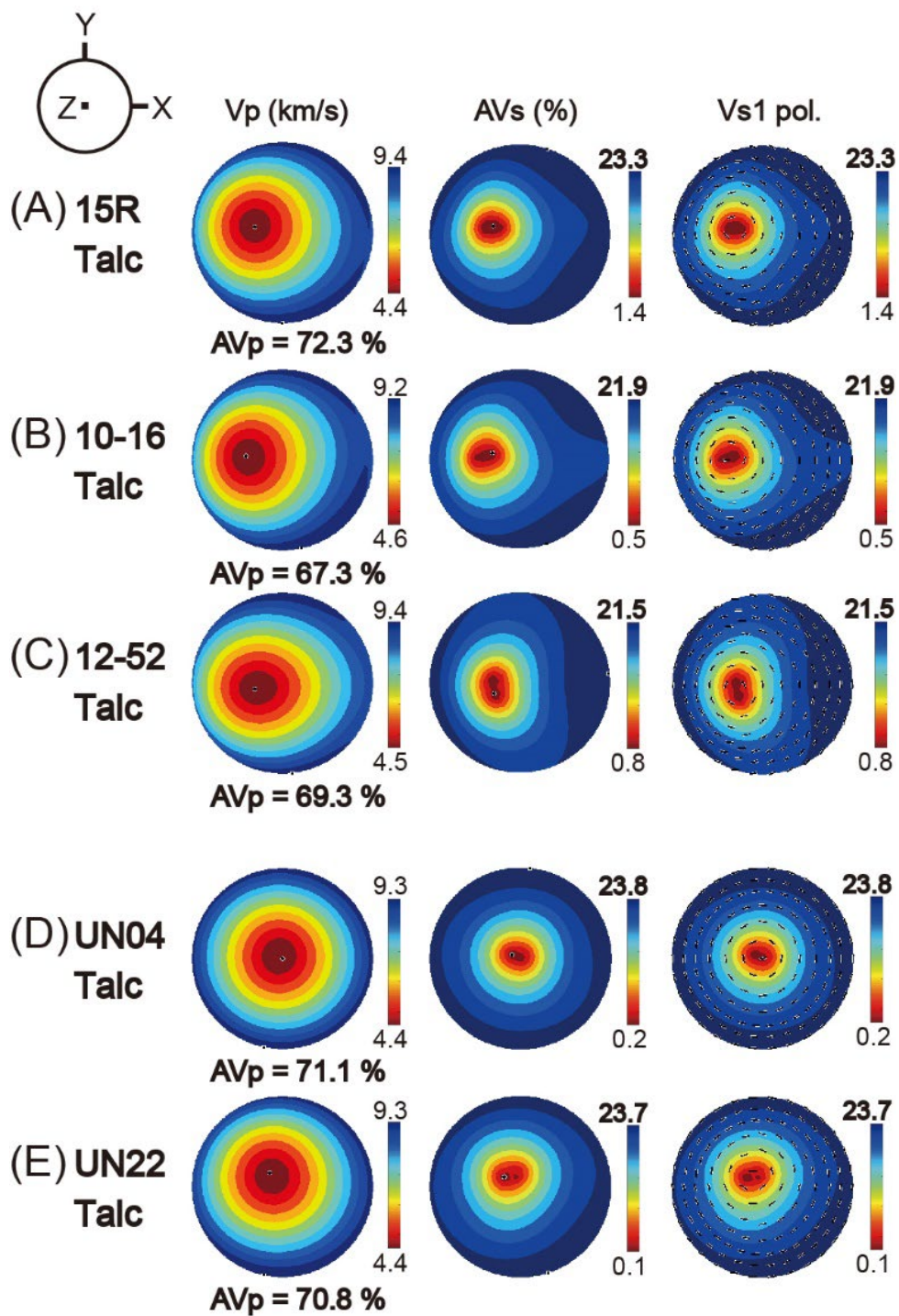
$V_p = 9.2 - 9.4$  km/s) compared to that of other mineral aggregates (max  $V_p = 7.1 - 8.9$  km/s).

Seismic anisotropy of S-wave ( $AV_s$  in %) of polycrystalline talc ranges from 22 to 23 % for the three UHP schist samples (**Figs. 2.6a – 2.6c**) and approximately 24 % for the two metasomatic schist samples (**Figs. 2.6d and 2.6e**). The S-wave anisotropy was lower in a seismic wave ray path of the direction subnormal to the foliation (**Figs. 2.6a – 2.6c**) or normal to the foliation (**Figs. 2.6d and 2.6e**) with strongly aligned (001) poles of talc. The S-wave anisotropy of the other composite minerals in this study is shown in **Fig. 2.9**.

Bulk rock seismic anisotropies were also calculated (**Figs. 2.7 and 2.9, Table 2.2**) by considering the CPOs and elastic properties of composite minerals (**Figs. 2.3 and 2.5**) and their modal abundances in the five samples (**Table 2.1**). The magnitudes of the bulk seismic anisotropies were found to be very large for P-waves (up to 55 %) and large for S-waves (up to 21 %) (**Table 2.2**).

Because the elastic anisotropy of single crystal talc decreases with increasing pressure (Mainprice et al., 2008), seismic anisotropy of polycrystalline talc may change at high pressure conditions. Therefore, the seismic anisotropy of polycrystalline talc was also calculated at a high pressure ( $P = 2.9$  GPa) using the elastic properties of single crystal talc at the given pressure (**Figs. 2.3 and 2.10**). The seismic anisotropies of polycrystalline talc showed low but still large seismic anisotropies of the P- and S-waves ( $AV_p = 38$  % and max  $AV_s = 18$  %) (**Fig. 2.10**). The increasing/decreasing pattern of seismic velocities and anisotropies at the higher

pressure ( $P = 2.9$  GPa) remained similar to that at ambient pressure conditions (see **Figs 2.6 and 2.10**).



(Caption in the next page)



**Figure 2.6.** P–wave velocity, P–wave azimuthal anisotropy, S–wave anisotropy and fast S–wave polarization direction of polycrystalline talc in each sample **(a – e)**. **(a, b and c)** Samples from UHP Makbal Complex. **(d, e)** Samples from Valla Complex in Unst. Colorbars in the right side indicate P–wave velocity ( $V_P$ ) of the talc aggregates in units of km/s.  $V_P$  (km/s): P–wave velocity,  $AV_P$  (%): anisotropy of P–wave,  $AV_S$  (%): anisotropy of S–wave,  $V_{S1}$  pol.: polarization direction of fast S–wave. X–direction is parallel to the lineation (L), Z–direction normal to the foliation (S), and Y–direction orthogonal to the X–Z plane.

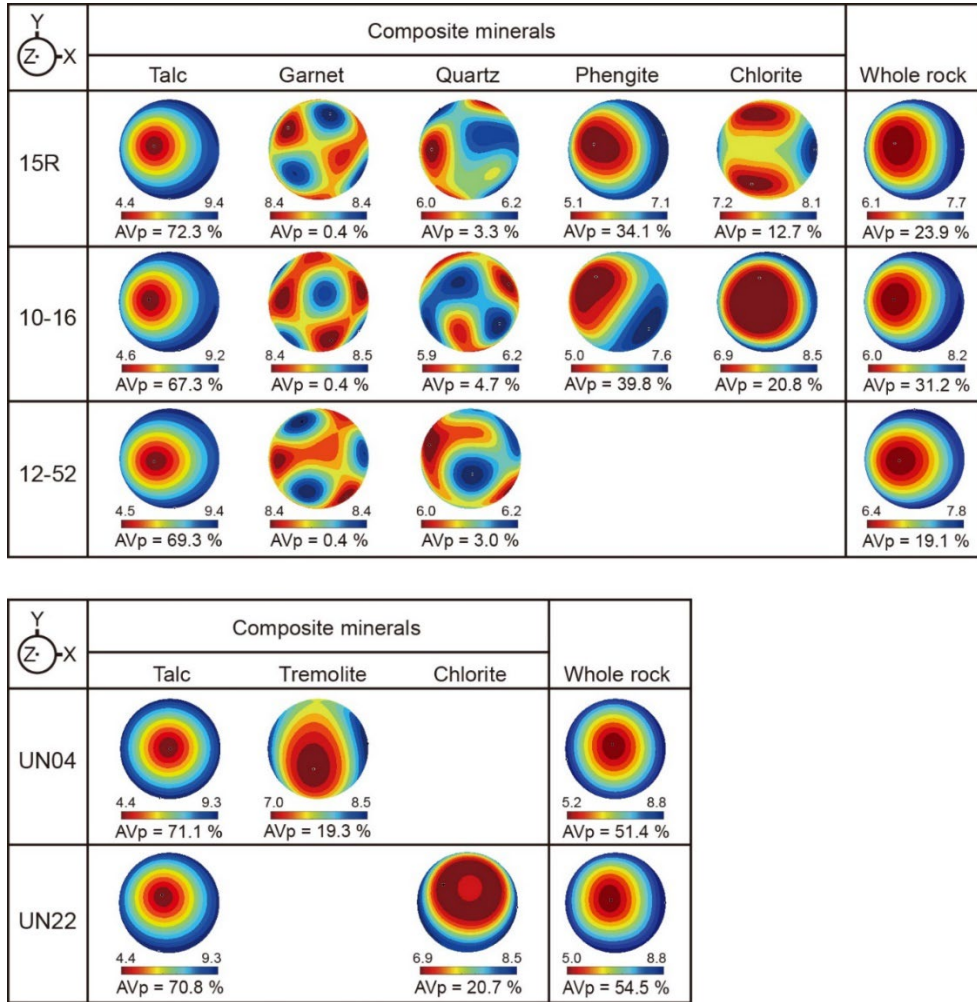


**Figure 2.7.** P–wave velocity and P–wave seismic anisotropy (AV<sub>P</sub> in %) of each polycrystalline mineral and whole rock of the five rock samples analyzed in this study. P–wave velocity in a red-blue colorbar. The modal composition shown in **Table 2.1** was used together with elastic constants of composite minerals and CPOs of each polycrystalline mineral. Reference frame of P–wave velocity is the same as that in **Fig. 2.6**.

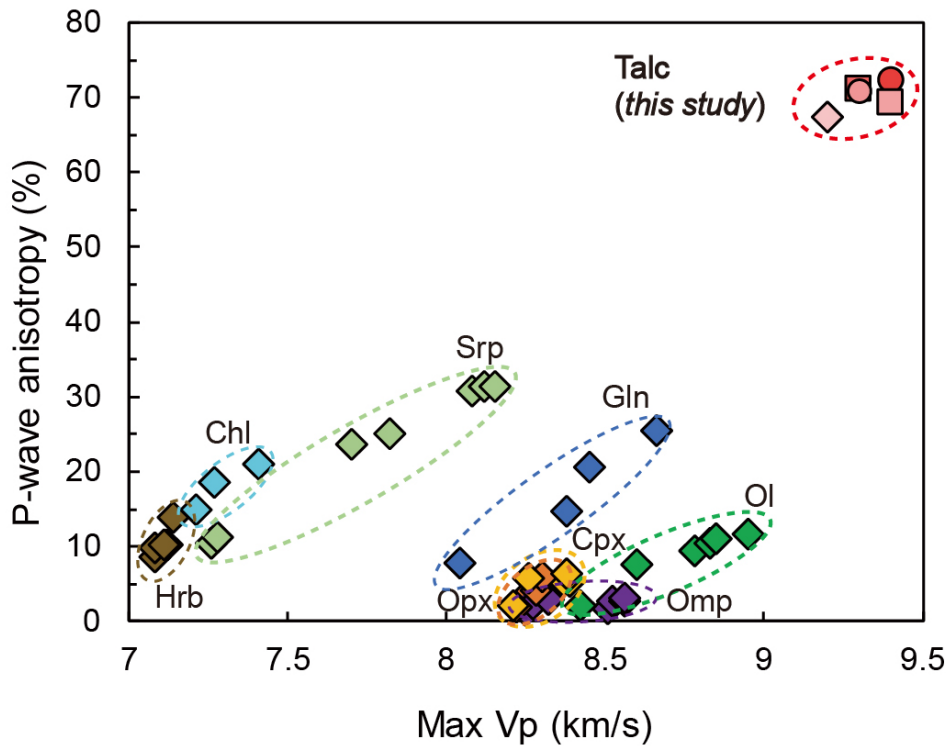


**Figure 2.8.** Comparison of the P–wave anisotropy of talc aggregates with that of other polycrystalline minerals. The P–wave anisotropy ( $AV_p$ ) data of polycrystalline minerals were obtained from natural samples and combined with data of their maximum P–wave velocities ( $V_p$ ). Talc in this study is denoted by the reddish color shapes of the analyzed five samples. Ol, olivine (Park and Jung, 2015); Opx (orange diamonds), orthopyroxene (Jung et al., 2010); Cpx (yellow diamonds), clinopyroxene (Park and Jung, 2015); Gln, glaucophane (Cao et al., 2013); Omp, omphacite (Cao et al., 2013; Kim et al., 2016); Srp, serpentine (Hirauchi et al., 2010; Jung, 2011; Watanabe et al., 2014); Chl, chlorite (Kim and Jung, 2015); and Hrb, hornblende (Ji et al., 2013).

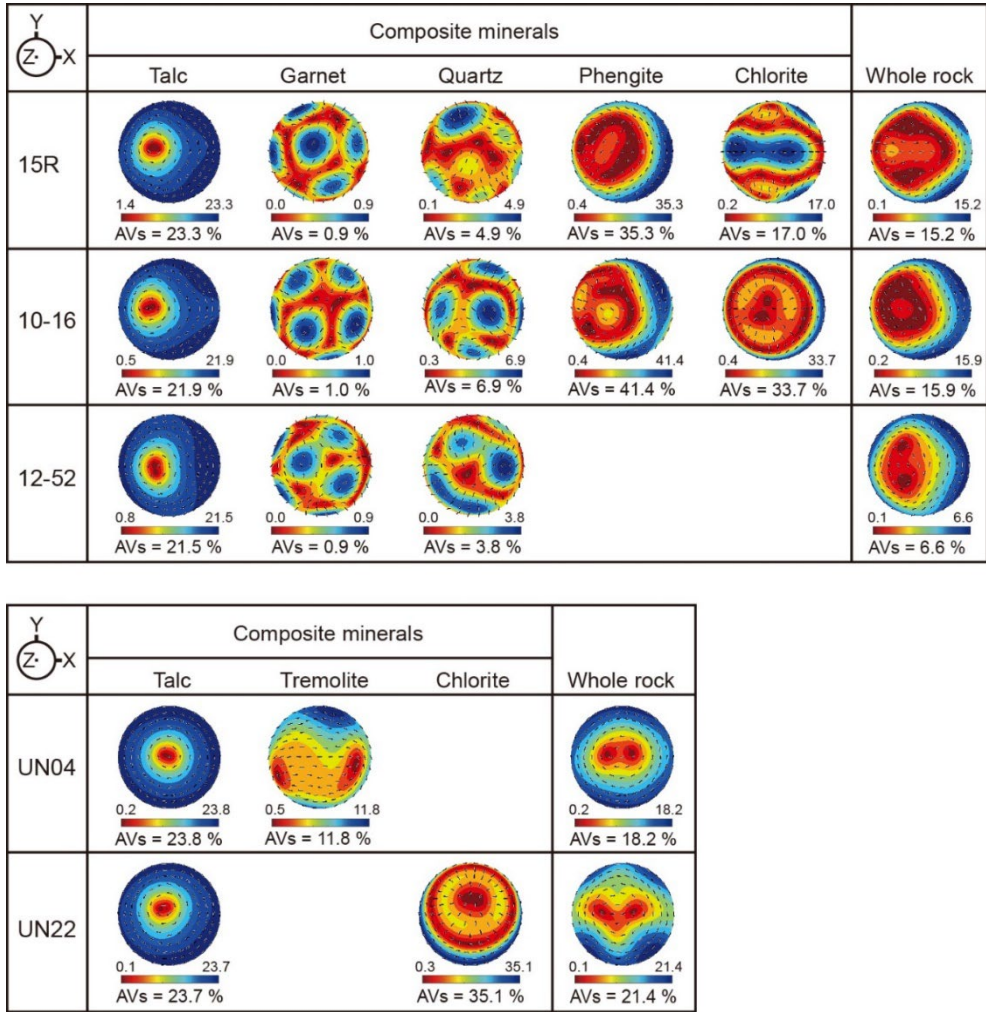


**Figure 2.9.** S-wave seismic anisotropy ( $AV_s$  in %) and fast S-wave ( $V_{s1}$ ) polarization directions of each polycrystalline mineral and whole rock of the five rock samples analyzed in this study. Black short lines indicate  $V_{s1}$  polarization directions. The modal composition shown in **Table 2.1** was used together with elastic constants of composite minerals and CPOs of each polycrystalline mineral. Reference frame of S-wave velocity is the same as that in **Fig. 2.6**.

## Polycrystalline talc (P = 29 kbars)

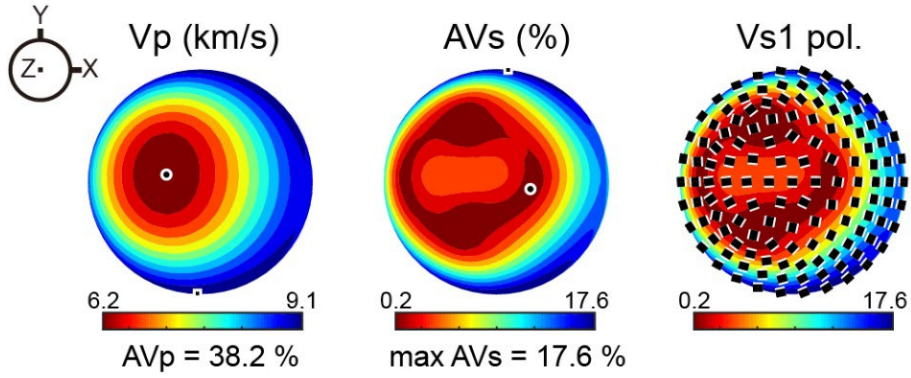


**Figure 2.10.** Seismic properties of polycrystalline talc at a high pressure of  $P = 2.9$  GPa. A representative talc CPO of sample 15R was used. A reference frame of  $V_p$ ,  $AV_s$  and  $V_{s1}$  polarization direction is the same as in **Fig. 2.6**.

## 2.4 Discussion

### 2.4.1 CPO development of talc

The CPO measurements of polycrystalline talc revealed strong maxima of (001) poles aligned subnormal to the foliation and a girdle distribution of both [100] axes and (010) poles subparallel to the foliation. The talc CPOs of (001) poles were subnormal to the basal plane, and may have developed due to its platy habit. In Makbal Complex schist samples, talc and other minerals present except for garnet porphyroblasts were intensively foliated, and the schist samples seem to have originated from the upper part of the oceanic plate and have experienced subduction-induced mantle flow (Meyer et al., 2014). Furthermore, intense simple shear along slab-mantle interfaces and/or nearly-vertical shear along hydrated faults within the slab (Faccenda et al., 2008) are thought to have generated a strong CPO of talc, closely associated with its basal glide parallel (or subparallel) to the flow plane. Basal plane glide of phyllosilicates has been documented as a dominant deformation mechanism in generating their CPOs (Wenk et al., 2010). Generally, the slab-mantle interface shows a complex flow structure by tectonic mixing to form serpentinite mélanges, which cannot be defined only by downward subduction. However, in the UHP rocks, the absence of pervasive deformation during the buoyancy-driven rapid exhumation is essential to allow the preservation of UHP minerals in the rocks (Guillot et al., 2009; Meyer et al., 2014). The observed S–C fabric of talc along the rigid garnet and the lack of garnet deformation (weak CPO and elongation of garnet, and weak elongation of inclusions in the garnet) are evidence of its low strain

deformation during the ultrahigh-pressure rock exhumation, which started after the formation of talc, and of its strong preferred orientation. Accordingly, the CPOs of talc in the UHP schists are thought to have dominantly formed during the prograde-to-peak metamorphic path of the subducting slab, i.e. by the intense shearing along the subduction interfaces. In addition, talc is thought to act as a weak and soft matrix surrounding more rigid minerals or rock slices and thereby forming high-strain shear zones that localize the deformation relatively parallel to the slab-mantle interface (Guillot et al., 2009).

The talc-rich ultramafic serpentinite bodies of the Unst Valla Field Block developed spectacular zoned mineral sequence structures (talc-tremolite-chlorite) by fluid-rock interactions (Read, 1934) comparable to those of ultramafic rocks in a subduction zone setting. The metasomatic schist samples can be considered to be representative of reaction products of mantle serpentinite or serpentinite blocks from the faults in the slab-mantle interface. This is also in accordance with the similar mineral-zoned structures of metasomatic ultramafic bodies from exhumed portions of the slab-mantle interface (Bebout and Barton, 2002). Talc alteration of mantle serpentinites is thought to mainly occur at the top of a subducting plate (Guillot et al., 2009; Spandler et al., 2008), where shearing is most intense during subduction and exhumation, producing the talc CPO of the metasomatic schist samples mostly during the latter.

## 2.4.2 Implication of talc CPO to the P-wave seismic anisotropy in subduction zones

Dense seismic networks like those within the Japan subduction zone have provided high-resolution P-wave anisotropy tomography (**Fig. 2.11**; Wang et al., 2017). The results showed that the fastest P-wave velocity parallel or subparallel to the trench direction (**Fig. 2.12a**), associated with a significantly P-wave anisotropy ( $AV_P$ ) of polycrystalline talc (**Figs. 2.7 and 2.8**). It would be influenced by strong CPO of talc aggregates and inherently high  $AV_P$  of talc single crystal. Maximum  $V_p$  value of single-crystal hydrous minerals such as antigorite (8.9 km/s), chlorite (8.1 km/s), glaucophane (9.3 km/s), hornblende (7.9 km/s) was similar to that of talc crystal (9.7 km/s). The strong CPO of talc aggregates however caused the relatively high maximum  $V_p$  (9.2 – 9.4 km/s), compared to that of other mineral aggregates (7.1 – 8.9 km/s in **Fig. 2.7**). This is consistent with the strong trench-parallel azimuthal anisotropy of P-waves observed in the Pacific slab (Wang and Zhao, 2013).



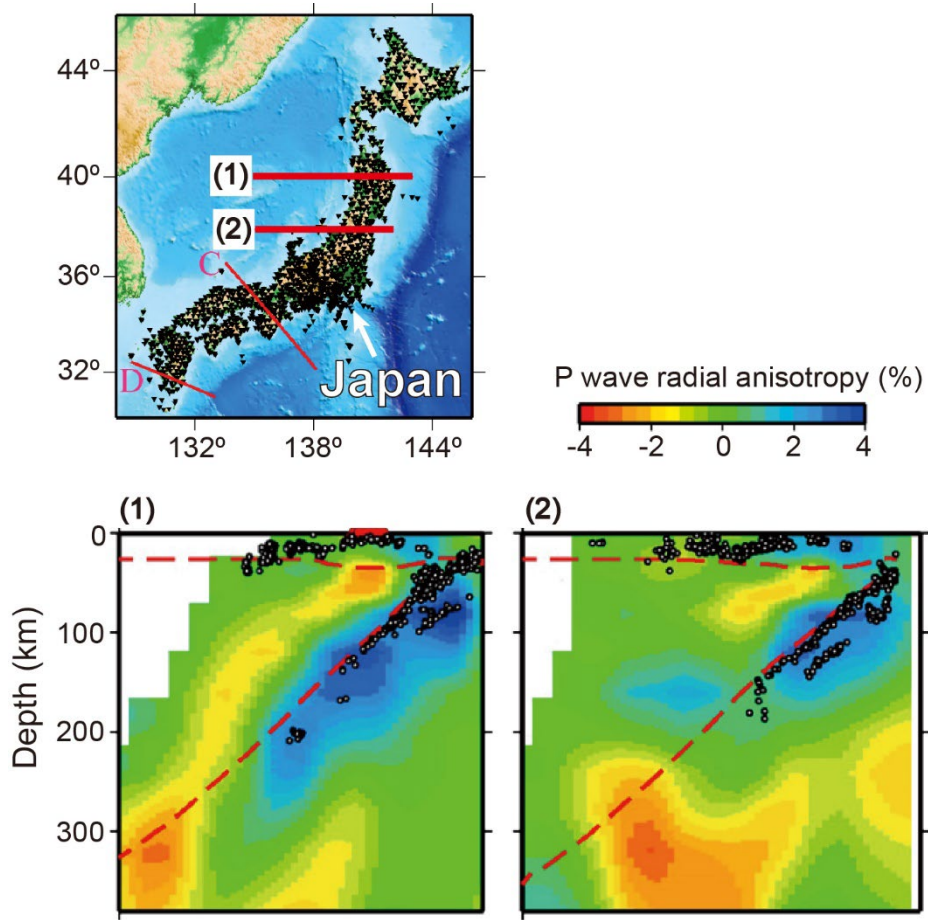


**Figure 2.11.** Images of P–wave radial anisotropy in the Japan subduction zone (Wang et al., 2017). Red and blue colours denote negative and positive radial anisotropies, respectively. The P–wave radial anisotropy (%) scale is shown above the images.

Positive P–wave radial anisotropy ( $RA > 0$ ; horizontal P–wave velocity  $>$  vertical P–wave velocity) is commonly observed in many subducting slabs, and negative P–wave radial anisotropy ( $RA < 0$ ; horizontal P–wave velocity  $<$  vertical P–wave velocity) in high-angle subducting slabs (e.g. Ryukyu arc) (Niu et al., 2016; Wang et al., 2017; Zhao et al., 2016). It has been suggested that this positive P–wave anisotropy was generated by both the dip-angle and the presence of the laminar structure of the slab (Ishise et al., 2018). This laminar structure is in accordance with the symmetrically similar layered structure of polycrystalline talc, implied by the strong talc CPO of (001) poles (**Fig. 2.4**).

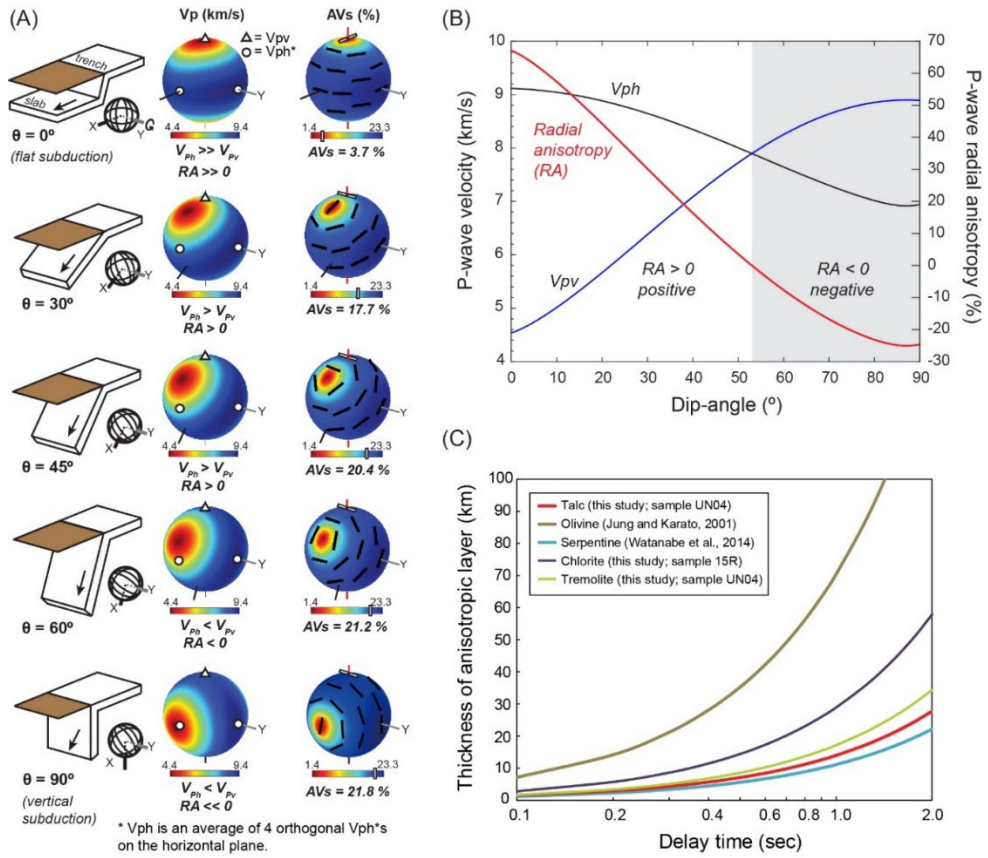
In order to understand the P–wave radial anisotropy of polycrystalline talc, I calculated the horizontal and vertical P–wave velocities and the P–wave radial anisotropy using the CPO of polycrystalline talc. As a result, the P–wave radial anisotropy (RA) was positive ( $RA > 0$ ) with a flow at a dip-angle ranging from  $0^\circ$  to  $50^\circ$  and was negative ( $RA < 0$ ) with a flow at a dip-angle ranging from  $60^\circ$  to  $90^\circ$  (**Fig. 2.12b**).

A close relationship between the radial anisotropy of talc and the dip-angle of the subduction zone (**Figs. 2.12a, 2.12b and 2.13**) is in accordance with the positive radial anisotropy in many subducting slabs and the negative radial anisotropy in high-angle subducting slabs. The subducting slab in subduction zones (Tohoku, Hokkaido, etc.) associated with Japan revealed a positive radial anisotropy (Zhao et al., 2016), while those with relatively high ( $\sim 60^\circ$ ) slab–dip angles (e.g. Ryukyu) a negative radial anisotropy (Wang et al., 2019). In addition, the Alps subduction zone, which is characterized by nearly vertical subduction of the

European and Adriatic slabs, also displayed a negative radial anisotropy of those subducting slabs (Hua et al., 2017).

### **2.4.3 Implication of talc CPO to the S-wave seismic anisotropy in subduction zones**

In many subduction zones, polarization directions of local and teleseismic fast-shear waves are trench-parallel and show a long delay time of S-wave splitting ( $\Delta t > 1$  sec) in some subduction zones (Long and Silver, 2008). Several factors have been shown to generate strong trench-parallel seismic anisotropy: B-type CPO of olivine in a hydrated mantle (Jung and Karato, 2001; Karato et al., 2008; McCormack et al., 2013), trench-parallel flow (Long and Silver, 2008), pressure-induced olivine CPO (Jung et al., 2009), shape-preferred orientation of fluid-filled cracks and hydrous faults in the slab (Faccenda et al., 2008; Healy et al., 2009), and strong CPOs of hydro-phyllsilicates such as serpentine (Katayama et al., 2009) and chlorite (Kim et al., 2020) in the slab and slab-mantle interface (Jung, 2017). However, I propose that the high S-wave anisotropy of talc ( $\max AV_s = 24\%$ ; **Fig. 2.4**) constitutes an important factor contributing to the trench-parallel seismic anisotropy in subduction zones.



(Caption in the next page)

**Figure 2.12.** P–wave anisotropy and S–wave anisotropy of polycrystalline talc with changes in the dip-angle of slab, and the thickness of anisotropic layer of talc as a function of delay time. **(a)** P–wave velocity ( $V_P$ ) and S–wave anisotropy ( $AV_S$ ) of talc aggregates in 3-dimensions considering the dip-angle ( $\theta$ ) of the subducting slab. Representative CPOs of talc in **Fig. 2.4** (sample 15R for  $V_P$  and sample UN04 for  $AV_S$ , respectively) were used. The reference frame is displayed in the left column. The X–direction is parallel to the flow direction and the X–Y plane is parallel to the subducting slab. The second column shows  $V_P$  (km/s) patterns, showing both P–wave azimuthal anisotropy and radial anisotropy (RA) with increasing slab dip-angle. Square dots denote vertical P–wave velocity ( $V_{Pv}$ ) and round dots show two of the four orthogonal P–wave velocities on the horizontal plane ( $V_{Ph}^*$ ) which were averaged to define the horizontal P–wave anisotropy ( $V_{Ph}$ ) (other two were not visible in the given 3-dimensional view). The third column shows  $AV_S$  (%) patterns and fast polarization directions of talc aggregates. Red lines indicate a ray path of vertically propagating S–wave. Long white bar at top of  $AV_S$  patterns represents the polarization direction of a vertically propagating fast S–wave, and each short white bar on the scale bar indicates the magnitude of  $AV_S$  for that S–wave. **(b)** Variations of  $V_{Ph}$ ,  $V_{Pv}$  and radial anisotropy (RA) with changes in slab dip-angle. Grey color area indicates the dip-angle ranges for the negative RA ( $RA < 0$ ). **(c)** Thickness of anisotropic layer ( $L$ ) as a function of delay time ( $dt$ ) of S–wave. The used  $AV_S$  of talc is 23.8 % (sample UN04 from this study), of olivine 4.9 % (Jung and Karato, 2001), of serpentine 25.0 % (Watanabe et al., 2014), of chlorite (sample 15R from this study) and of tremolite (sample UN04 from this study).

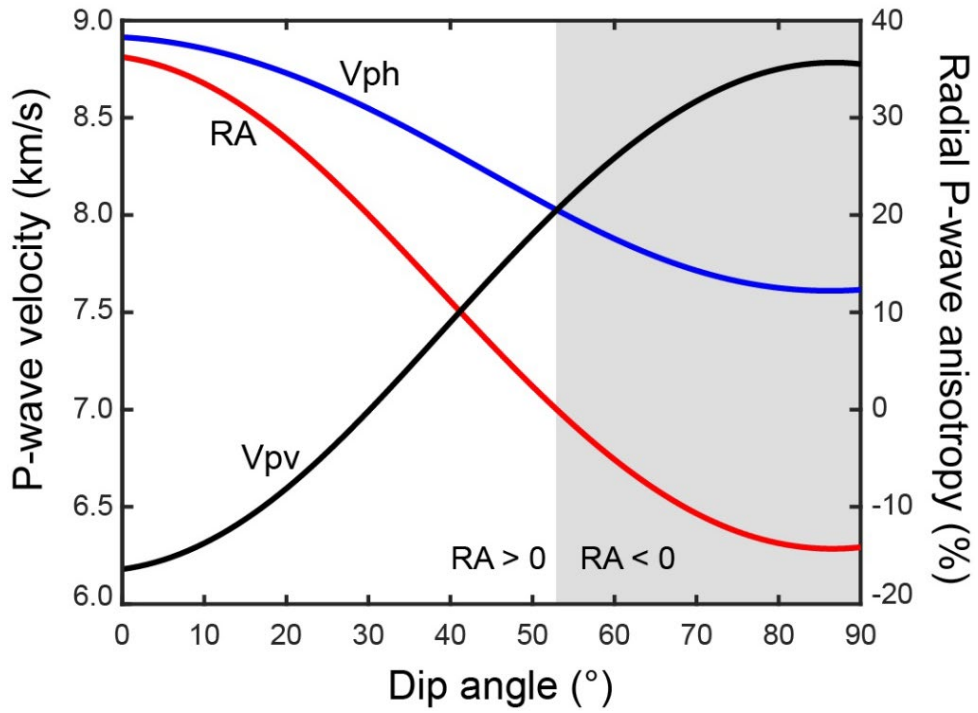


**Figure 2.13.** Variations of  $V_{Ph}$ ,  $V_{Pv}$ , and RA of polycrystalline talc at  $P = 2.9$  GPa with increasing slab dip-angle. Grey colour area indicates the dip-angle range for negative RA ( $RA < 0$ ). It was plotted by using the same method as done for **Fig. 2.12b**.

Considering a lineation direction normal to the trench, the fast S-wave ( $V_{S1}$ ) polarization direction driven by the CPO of talc is trench-parallel (Y-direction in **Figs. 2.9 and 2.12a**). The trench-parallel polarization direction of the fast S-waves is associated with intense shear deformation of talc aggregates in subduction zones where the slab dip-angle is  $30^\circ$  or larger. In addition, steep dip-angles ( $\theta = 45 - 90^\circ$ ; **Fig. 2.12a**) of subducting slabs generate a strengthening of trench-parallel anisotropy of polycrystalline talc ( $AV_s$  is larger). **Figure 2.9** shows the importance of talc for the trench-parallel polarization direction of the whole rock. Along the ray path at low-to-high angle to the foliation of the rock, the  $V_{S1}$  polarization direction of the whole rock is strongly dominated by that of polycrystalline talc (**Fig. 2.9**). This result is consistent with observations of strong anisotropic signatures with long delay times in high-angle subduction zones (Long and Silver, 2008).

Long delay times of local S-waves ( $dt > 1$  sec) have been observed in the Ryukyu, Aleutian, Izu-Bonin and Tonga fore-arc zones (Long and Silver, 2008), and are commonly recorded in the strongly anisotropic layers of the mantle wedge and the slab-mantle interfaces of these regions. The B-type CPO of olivine is often regarded as the cause of trench-parallel seismic anisotropy in supra-subduction zones, however, the long delay time in some fore-arc zones requires a medium that is much more anisotropic than olivine (McCormack et al., 2013). Talc is a suitable candidate for generating the long delay time of S-waves since it occurs in large parts of the mantle wedge and slab (Hacker et al., 2003), and along hydrated high-angle faults in the slab (Faccenda et al., 2008). Under silica-saturated conditions, talc is stable up to temperatures of  $T = 825^\circ\text{C}$  along slab-mantle interfaces (Bose and Ganguly, 1995).

Considering the thermal structure of subduction zones (Faccenda et al., 2008; Peacock, 2003), talc should also be stable in the subducting slabs and mantle wedges of the Aleutian, Izu-Bonin, and Ryukyu fore-arc zones.

To evaluate the magnitude of the S-wave anisotropy of talc, I compared the delay time of polycrystalline talc with that of B-type olivine, serpentine and other major hydrous minerals (chlorite and tremolite), and calculated the thickness of the anisotropic layer ( $L$ ) required for generating a certain delay time ( $dt$ ) as  $L = dt \times (V_{s1} + V_{s2}) / (2 \times AV_s)$  (**Fig. 2.12c**). Using the CPO of B-type olivine with an  $AV_s$  of 4.9 % (Jung and Karato, 2001) and a dip-angle of  $45^\circ$ , an anisotropic layer thickness of 70 km of B-type olivine is required to generate a  $dt$  of 1 s. However, a thickness of 70 km of the olivine layer would exceed that of the mantle wedge ( $L$  ca. 60 km) below the Ryukyu fore-arc zone (McCormack et al., 2013). By using the CPO of talc aggregates (sample UN04 in this study) with an  $AV_s$  of 23.8 % and a dip-angle of  $45^\circ$ , a thickness of 14 km is required to produce a delay time of 1 s (**Fig. 2.12c**). Therefore, instead of seismically anisotropic serpentine (Katayama et al., 2009; Watanabe et al., 2014), it is also likely that polycrystalline talc generated the seismic anisotropy below the Ryukyu fore-arc zone. The thickness required for a delay time was also calculated for polycrystalline chlorite (sample 15R) and tremolite (sample UN04) with a given dip-angle of  $45^\circ$  (**Fig. 2.12c**). The results of both mineral phases showed shorter delay times compared to talc, indicating that not only serpentine but talc is most significant for generating long delay time. Further studies should include geophysical and numerical modeling in order to evaluate the quantitative effect of talc in subduction zone interface.



## 2.5 Conclusion

This is a first report of measured CPOs of polycrystalline talc in natural rock samples which include a strong CPO showing a strong alignment of (001) planes subparallel to the foliation and a girdle distribution of [100] axes and (010) poles subparallel to the foliation. The seismic anisotropy results of polycrystalline talc suggest that the strong CPO of talc, together with the CPOs of olivine and other hydrous minerals such as serpentine, significantly contribute to the production of seismic anisotropies of both P-waves and S-waves in subduction zones.

## **CHAPTER 3. Seismic anisotropy in subduction zones: evaluating the role of chloritoid**

\* This chapter has been modified from a published paper:

**J. Lee**, M. Mookherjee, T. Kim, H. Jung, and R. Klemd. (2021). Seismic Anisotropy in Subduction Zones: Evaluating the Role of Chloritoid, *Frontiers in Earth Science*, 9, 644958.

### **Abstract**

Subduction zones are often characterized by the presence of strong trench-parallel seismic anisotropy and large delay times. Hydrous minerals, owing to their large elastic anisotropy and strong crystallographic preferred orientations (CPOs) are often invoked to explain these observations. However, the elasticity and the CPO of chloritoid, which is one of such hydrous phases relevant in subduction zone settings, is poorly understood. In this chapter, I measured the CPO of polycrystalline chloritoid in natural rock samples, obtained the CPO-induced seismic anisotropy, and evaluated the thermodynamic stability field of chloritoid in subduction zones. The CPO of chloritoid aggregates displayed a strong alignment of the [001] axes subnormal to the rock foliation, with a girdle distribution of the [100] axes and the (010) poles subparallel to the foliation. New elasticity data of single-crystal

chloritoid showed a strong elastic anisotropy of chloritoid with 47% for S-waves ( $V_S$ ) and 22% for P-waves ( $V_P$ ), respectively. The combination of the CPO and the elastic anisotropy of the chloritoid aggregates produced a strong S-wave anisotropy with a maximum  $AV_S$  of 18% and a P-wave anisotropy with an  $AV_P$  of 10%. The role of chloritoid CPO in seismic anisotropy was evaluated in natural rock samples and a hypothetical blueschist. The results indicate that the strong CPO of chloritoid along the subduction interface and in subducting slabs can influence the trench-parallel seismic anisotropy in subduction zones with “cold” geotherms.

**Keywords:** chloritoid, CPO, seismic anisotropy, subduction zone.

### 3.1 Introduction

Solid-state mantle flow is inferred from seismically observed anisotropy in the upper mantle, in subducting slabs, and in many forearc zones and arc regions. Seismic anisotropy is intricately related to the crystallographic preferred orientation (CPO) of major mantle minerals (Ben Ismaïl and Mainprice, 1998; Jung, 2017; Karato et al., 2008; Long and Silver, 2008; Nicolas and Christensen, 1987; Savage, 1999). Due to its volumetric abundance in the upper mantle, the CPO of olivine has been extensively studied (Boneh et al., 2017; Cao et al., 2017; Hansen et al., 2014; Jung and Karato, 2001; Michibayashi et al., 2016; Ohuchi et al., 2011; Précigout et al., 2017; Skemer and Hansen, 2016; Soustelle and Manthilake, 2017; Tommasi and Vauchez, 2015). It is well known that the subducting mantle is variably hydrated and although olivine is volumetrically the most abundant mineral in subducting slabs, olivine dominant lithologies alone are often insufficient to provide adequate explanations for the large delay times observed by teleseismic studies (e.g. Katayama et al., 2009; Nagaya et al., 2016). Possible alternative mechanisms suggest that volumetrically less abundant hydrous phases are significantly more elastically anisotropic than major mantle phases (Faccenda et al., 2008; Jung, 2011; Katayama et al., 2009; Kim et al., 2020; Mookherjee and Capitani, 2011; Mookherjee and Mainprice, 2014). However, in contrast to olivine, the elasticity and CPOs of volumetrically less abundant hydrous mineral phases are incompletely understood and require further study. The few hydrous minerals like serpentine, amphibole, and chlorite, which have been recently examined, exhibit extreme elastic anisotropy and often a strong CPO (Almqvist and Mainprice, 2017; Horn et al., 2020; Jung, 2017;

Kang and Jung, 2019; Katayama et al., 2009; Kim and Jung, 2015; Mainprice and Ildefonse, 2009; Mookherjee and Mainprice, 2014; Nagaya et al., 2016; Puelles et al., 2012). Chloritoid is such a hydrous phase whose elasticity and CPO remain unknown. Since chloritoid is often found in metamorphosed rocks relevant for subduction zone settings, constraining the elasticity and CPO of chloritoid, it is likely to shed valuable insight on the seismic anisotropy of subduction zones.

Chloritoid  $[(\text{Mg,Fe})_2\text{Al}_4\text{Si}_2\text{O}_{10}(\text{OH})_4]$  commonly occurs in greenschist to eclogite facies metamorphic rocks with diverse bulk chemistries, including both felsic and mafic rocks (Messiga et al., 1995; Negulescu et al., 2009; Poli and Schmidt, 1997; van Keken et al., 2002). In previous studies of chloritoid-bearing rocks, chloritoid modal amount of 10–23 vol% has been reported (e.g. Haerinck et al., 2013; Regis et al., 2014). Furthermore, chloritoid is a metamorphic indicator mineral for high- to ultrahigh-pressure metamorphic conditions relevant for subduction zone settings and collision belts (Kienast and Messiga, 1987; Meyer et al., 2014; Negulescu et al., 2009; Smye et al., 2010; Wei and Song, 2008). The lithologies of subducting hydrated oceanic crust and the overlying high-pressure metapelites are dominated by aluminous minerals such as garnet, lawsonite, epidote, and chloritoid. Among these minerals, the elasticity of chloritoid is virtually unknown. However, a recent X-ray synchrotron diffraction study has explored the bulk preferred orientation of chloritoid in a low-grade metamorphic slate (Haerinck et al., 2015).

In this study, I measured the CPO of chloritoid in schistose rock samples by EBSD analysis and used the results to explore the influence of chloritoid-bearing lithologies on the seismic anisotropy in subduction zone settings. I further re-

evaluated the pressure-temperature stability field of chloritoid in subduction zones. In addition, the role of chloritoid in the generation of seismic anisotropy of the slab was examined by comparing its seismic signature with that of other previously studied hydrous minerals, which were found to be stable with chloritoid.

## 3.2 Materials and Method

### 3.2.1 Rock samples

Three garnet-chloritoid-talc schist samples (#15R, #10-16, and #12-52) containing 10–25 vol.% of chloritoid were used to examine the CPO of chloritoid. The abundance of chloritoid in samples was similar to that reported from other localities (10–23 vol%). Additional minerals are phengite, chlorite, quartz, rutile, and minor apatite (**Table 2.1**). The strong foliation of talc and phengite defines the schistosity, while the lineation is defined by the average elongation direction of chloritoid, talc, and phengite (**Fig. 3.1**). Porphyroblastic garnets (5–10 mm in diameter) are embedded in the matrix (**Figs. 3.1**). Idioblastic chloritoid grains are associated with subidioblastic talc. The chloritoid grain size was measured using the linear intercept method (Gifkins, 1970). Chloritoid is coarse-grained and porphyroblastic in samples #15R (~500  $\mu\text{m}$ ) and #10-16 (~610  $\mu\text{m}$ ), and fine-grained in sample #12-52 (~150  $\mu\text{m}$ ) (**Figs. 3.1b, 3.1d and 3.1f**). Equigranular ellipsoidal chloritoid grains are homogeneously distributed in the fine-grained sample (#12-52) (**Fig. 3.1f**) when compared to the porphyroblastic or clustered occurrence of the coarser-grained chloritoid in samples #15R and #10-16 (**Fig. 3.1b and 3.1d**). Sample

#15R is moderately retrogressed, as revealed by the presence of chlorite replacing chloritoid and garnet. Relict euhedral chloritoid grains occur strongly elongated subparallel to the lineation (**Fig. 3.1b**). The porphyroblastic chloritoid grains of sample #10-16 show internal deformation features such as twinning and undulose extinction (**Figs. 3.1d and 3.2**). The fine-grained sample #12-52 is characterized by chloritoid grains that lack internal deformation features such as undulose extinction, microkinks, and subgrain boundaries (**Fig. 3.1f**).

### 3.2.2 Measurement of the CPO

The CPO of chloritoid was measured using electron-backscattered diffraction (EBSD) with a JEOL JSM-6380 scanning electron microscope (SEM) located in the School of Earth and Environmental Sciences at Seoul National University. The SEM was operated using an accelerating voltage of 20 kV, a vacuum level of chamber of  $9.6 \times 10^{-5}$  Pa, 1-nA current, 5- $\mu$ m beam size, and a working distance of 15 mm. All thin sections were carbon coated. To avoid repeated data collection, the EBSD patterns were indexed manually for every single grain. For a better data quality, the CPO of chloritoid was measured with a mean angular deviation of less than  $1.0^\circ$  and a minimum of 11 diffraction Kikuchi bands for each point measurement. A monoclinic instead of a triclinic space group symmetry of the chloritoid was used for the analysis, because the detected Kikuchi bands closely matched the simulated Kikuchi bands of the monoclinic chloritoid.

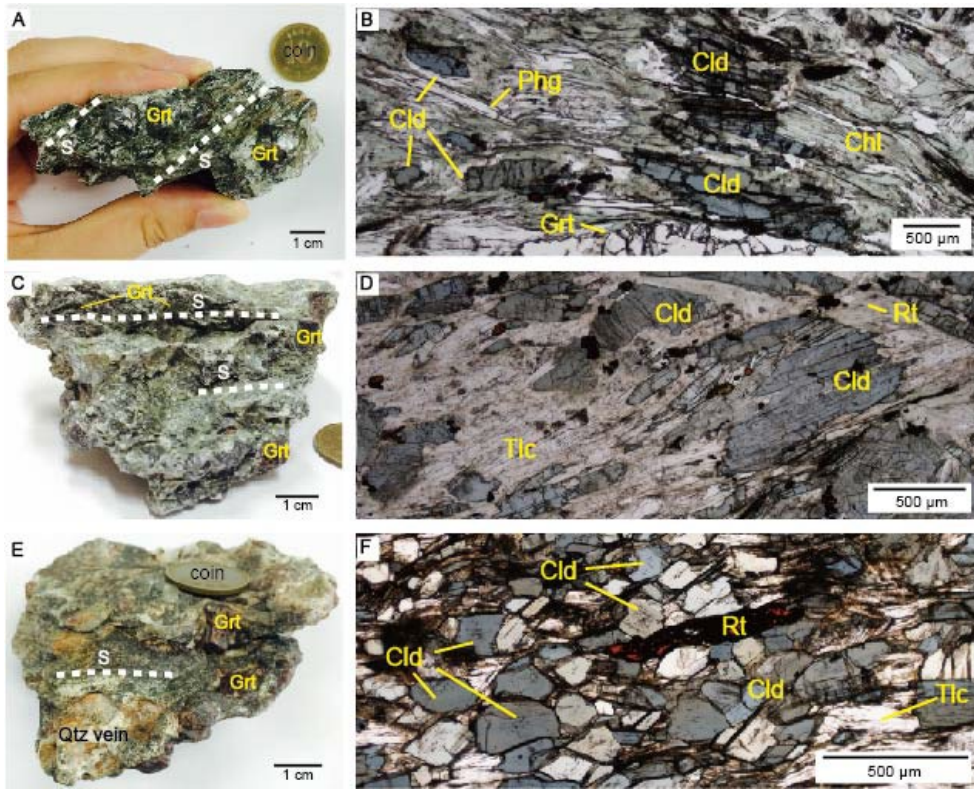


**Figure 3.1** Hand specimen (**a, c, e**) and plane-polarized microphotographs (**b, d, f**) of UHP Makbal garnet-chloritoid-talc schist samples. (**a, b**) sample #15R, (**c, d**) sample #10-16, (**e, f**) sample #12-52. In hand specimen, dashed lines denote the well-developed foliation (S). The lineation was determined on the foliation, by averaging directions of elongation of chloritoid and talc, and here parallel to the horizontal scale bar shown. Grt, garnet; Qtz, quartz; Cld: chloritoid; Tlc: talc; Rt: rutile.



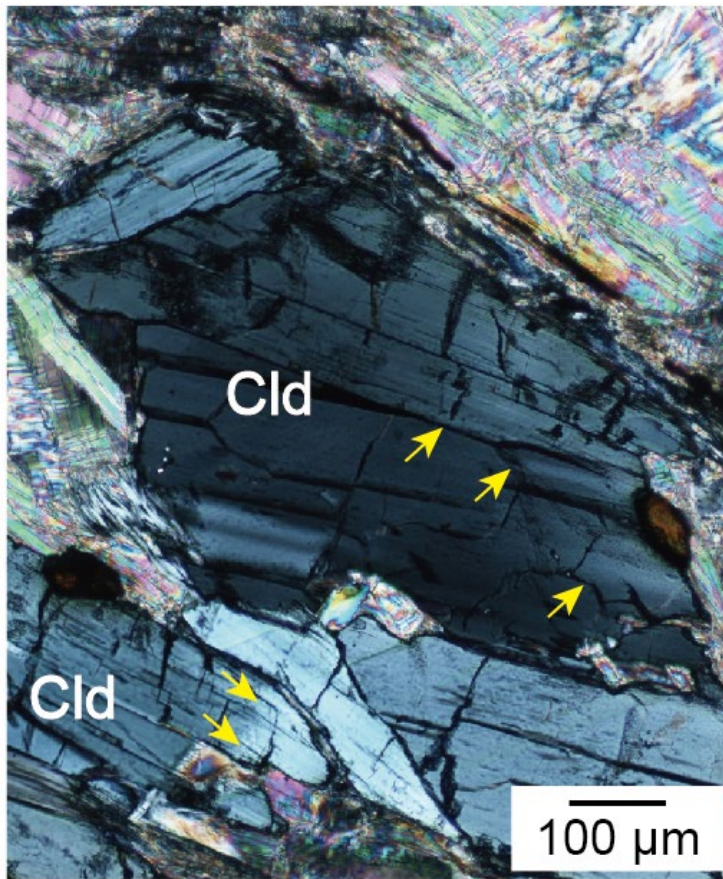


**Figure 3.2** Undulose extinction of chloritoid in sample #10-16 (arrows). Cld: chloritoid.

The chloritoid CPOs in the Grt-Cld-Tlc schist samples were plotted using the MATLAB toolbox MTEX, version 5.4.0. (Mainprice et al., 2011). For plotting the CPO, the orientation distribution functions of the chloritoids were calculated using a de la Vallée Poussin kernel with half widths of  $10^\circ$ . The strength of the CPO was quantified by the J-index (Bunge, 1982) and M-index (Skemer et al., 2005).

### 3.2.3 Elasticity of single-crystal chloritoid

In order to obtain the elastic properties of chloritoid crystal, *first principles* simulations were performed based on the density functional theory (Hohenberg and Kohn, 1964; Kohn and Sham, 1965). The chloritoid was investigated with a widely used approximation of the exchange-correlation functionals –the local density approximation (LDA) and the generalized gradient approximation (GGA) with the highly accurate projector augmented wave (PAW) method as implemented in the Vienna *ab initio* simulation package (VASP) (Kresse and Joubert, 1999). The monoclinic ( $C2/c$  space group) crystal structure (Comodi et al., 1992) was used with a  $\text{Mg}_2\text{Al}_4\text{Si}_2\text{O}_{10}(\text{OH})_4$  stoichiometry and a series of convergence tests was performed by varying the energy cut-off and  $k$ -points. An observed energy cut-off of  $E_{\text{cut-off}} = 900$  eV and a  $k$ -point mesh of the  $2 \times 4 \times 1$  Monkhorst-Pack grid (Monkhorst and Pack, 1976) with six irreducible  $k$ -points were sufficient for describing the energetics of chloritoid. In order to determine the full elastic constant tensor, the lattice parameters were strained by 0.5, 1.0, and 1.5% for one static volume, and it was

observed that an appropriate  $\sim 1\%$  strain was within the elastic limit (e.g. Chheda et al., 2014). The elastic stiffness constants ( $C_{ij}$ s) for monoclinic magnesiochloritoid, calculated using the GGA and LDA methods, are reported in **Table 3.1**.

**Table 3.1** Elastic stiffness tensor ( $C_{ij}$  in GPa) of single crystal chloritoid using the GGA method (P = 0 GPa, density = 3.10 g/cm<sup>3</sup>) and the LDA method (P = 0 GPa, density = 3.30 g/cm<sup>3</sup>).

<b>GGA</b>							
<b>i</b>	<b>j</b>	<b>1</b>	<b>2</b>	<b>3</b>	<b>4</b>	<b>5</b>	<b>6</b>
<b>1</b>		297.7	72.1	45.1	0.0	11.2	0.0
<b>2</b>			275.2	36.6	0.0	-4.4	0.0
<b>3</b>				262.4	0.0	3.1	0.0
<b>4</b>					45.8	0.0	-7.5
<b>5</b>						44.2	0.0
<b>6</b>							112.6
<b>LDA</b>							
<b>i</b>	<b>j</b>	<b>1</b>	<b>2</b>	<b>3</b>	<b>4</b>	<b>5</b>	<b>6</b>
<b>1</b>		336.0	82.0	63.0	0.0	12.9	0.0
<b>2</b>			319.6	56.0	0.0	-6.7	0.0
<b>3</b>				320.2	0.0	2.1	0.0
<b>4</b>					51.8	0.0	-8.0
<b>5</b>						46.8	0.0
<b>6</b>							126.2

### 3.2.4 Calculation of the seismic velocity and anisotropy

The seismic anisotropy of single-crystal chloritoid and that of polycrystalline chloritoid were obtained with the MSAT toolkit (Walker and Wookey, 2012), using elastic constants determined in this study. The elastic constants were determined at ambient pressures ( $P = 0$  GPa) using *first principles* with both the GGA and the LDA. The zero-pressure density predicted using the LDA of  $\sim 3.30 \text{ gcm}^{-3}$  is larger than that using the GGA of  $\sim 3.10 \text{ gcm}^{-3}$ . Also, the elastic constants predicted using the LDA are stiffer than that of using the GGA (**Table 3.1**). This difference between the GGA and the LDA results is expected and has already been reported for other hydrous mineral assemblages (Mookherjee and Bezacier, 2012; Peng and Mookherjee, 2020). It was observed that the aggregate bulk moduli for the GGA was in better agreement with the experimental estimates of the bulk modulus (Grevel et al., 2005).

The seismic velocities ( $V_P$  and  $V_S$ ) were calculated with the Christoffel equation (e.g. Mainprice et al., 2008). A plot of the elastic anisotropies of the single-crystal chloritoid is presented in **Figure 3.3**. The P-wave anisotropy ( $AV_P$ ) for the mineral aggregates was calculated as:

$$AV_P (\%) = \frac{(V_{Pmax} - V_{Pmin})}{(V_{Pmax} + V_{Pmin})/2} \times 100$$

where,  $V_{Pmax}$  refers to the maximum P-wave velocity ( $V_P$ ) and  $V_{Pmin}$  to the minimum P-wave velocity ( $V_P$ ). The S-wave anisotropy for the mineral aggregates ( $AV_S$ ) is defined as

$$AV_s (\%) = \frac{(V_{s1} - V_{s2})}{(V_{s1} + V_{s2})/2} \times 100$$

using the Voigt-Reuss-Hill averaging scheme, where the  $V_{s1}$  and  $V_{s2}$  represent the fast and slow S-wave velocity, respectively (Mainprice, 1990). The seismic anisotropies of the chloritoid aggregates were calculated with the  $C_{ij}$  values determined in this study using the GGA (**Fig. 3.3**). I calculated the seismic properties of other hydrous minerals in the Grt-Cld-Tlc schists, using the single-crystal elastic constants ( $C_{ij}$ ) of chloritoid (this study), chlorite (Mookherjee and Mainprice, 2014) and for phengitic mica, I used the elastic constants of muscovite (Vaughan and Guggenheim, 1986). For consistency, ambient-pressure elastic constants were used for all minerals. To calculate the bulk seismic anisotropy of the Grt-Cld-Tlc schist and a hypothetical blueschist (detailed in **Section 3.4.4**), the elastic constants of the composite minerals were averaged using the Voigt–Reuss–Hill scheme and the modal compositions (see **Table 2.1** and captions of **Table 3.2**).

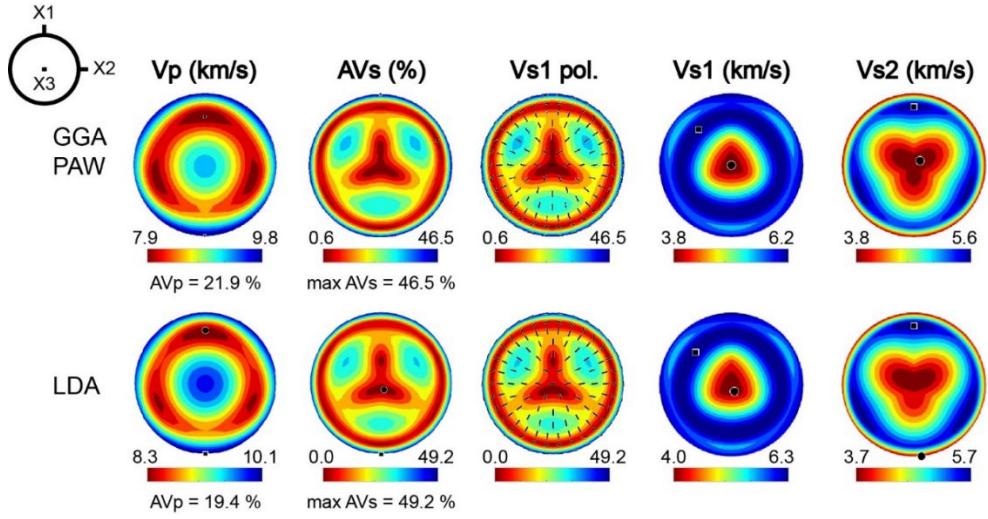


**Figure 3.3** Elastic anisotropy of single-crystal monoclinic chloritoid at a pressure of 0 GPa. The P-wave anisotropy was high ( $AV_p = 21.9\%$  and  $19.4\%$  for the GGA PAW and LDA methods, respectively) and the shear wave anisotropy was very high (max  $AV_s = 46.5\%$  and  $49.2\%$  for the GGA PAW and LDA methods, respectively). The polarization directions of the fast shear wave ( $V_{s1}$  polarized) are shown as black bars. A reference frame for monoclinic symmetry is shown on the left and depicts three orthogonal axes X1, X2 and X3, where X2 is parallel to the crystallographic b-axis and the plane normal to the b-axis is a mirror plane containing X1 and X3 (where X1 corresponds to the reciprocal a\*-axis and X3 is parallel to the crystallographic c-axis).  $V_p$ : P-wave velocity,  $AV_s$ : shear wave anisotropy,  $V_{s1}$  pol: polarization direction of the fast S-wave,  $V_{s1}$ : fast S-wave velocity,  $V_{s2}$ : slow S-wave velocity.

**Table 3.2** Seismic velocity and anisotropy of hydrous minerals and a hypothetical bulk rock.

Mineral	AV <sub>P</sub> (%)	Max AV <sub>S</sub> (%)	V <sub>S1</sub> (km/s)	V <sub>S2</sub> (km/s)	Reference
Cld	10.3	18.1	4.7 – 5.4	4.5 – 5.2	Sample #15R (this study)
Phg	34.1	35.3	3.2 – 4.2	2.9 – 3.5	Sample #15R (Lee et al., 2020)
Chl	12.7	17.0	4.2 – 4.7	3.7 – 4.4	Sample #15R (Lee et al., 2020)
Gln	20.7	11.0	4.4 – 4.9	4.3 – 4.5	Cao et al. (2013)
Lws	10.1	16.3	4.1 – 4.5	3.7 – 4.3	Choi et al. (2021)
Bulk rock*	10.2	9.3	4.1 – 4.5	4.1 – 4.3	Hypothetical one (this study)

\* The hypothetical bulk rock consists of Cld (15 vol%), Phg (15 vol%), Chl (15 vol%), Gln (30 vol%), and Lws (25 vol%).

AV<sub>P</sub>: anisotropy of P-wave, max AV<sub>S</sub>: maximum anisotropy of S-wave, V<sub>S1</sub>: fast S-wave velocity, V<sub>S2</sub>: slow S-wave velocity.

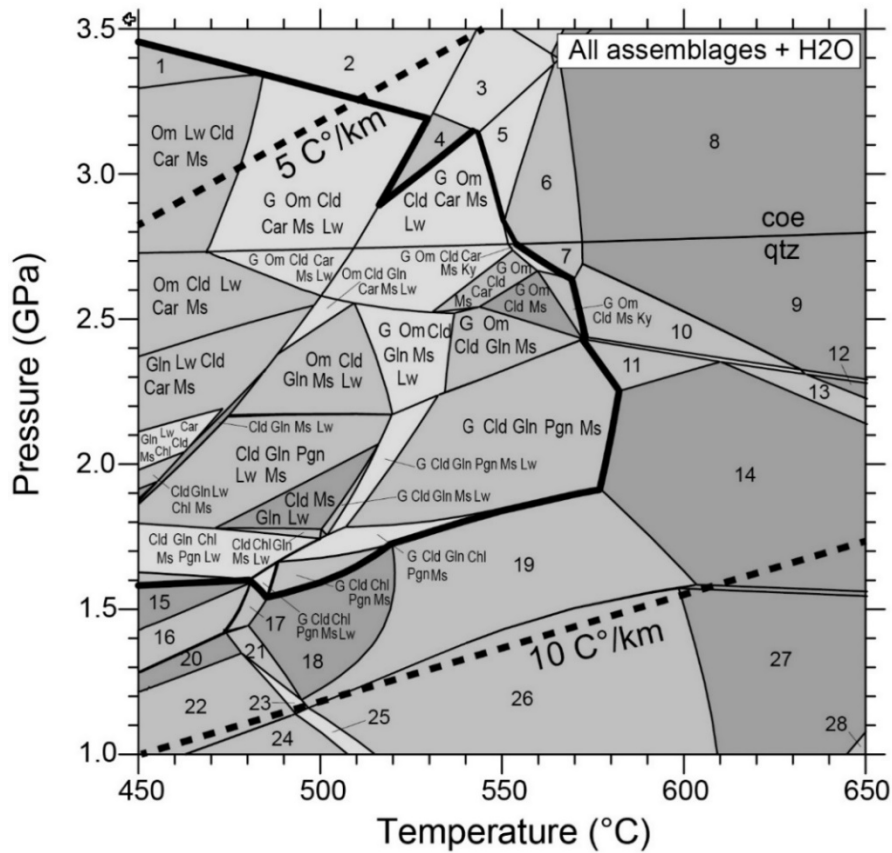
Cld: chloritoid, Phg: phengite, Chl: chlorite, Gln: glaucophane, Lws: lawsonite.



### 3.2.5 Calculation of the thermodynamic stability and modal abundance of chloritoid

I used thermodynamic calculations to obtain the equilibrium pressure-temperature (P-T) stability field for chloritoid, commonly referred to as pseudosections. In addition, I determined the modal abundance (i.e., volume percentage of chloritoid as a function of pressure and temperature) in the different pseudosections calculated in this study. The bulk compositions of three different rock types were considered: (1) Grt-Cld-Tlc schist (this study), (2) average pelite (Shaw, 1956) (**Fig. 3.4**), and (3) aluminous metagabbro (Messiga et al., 1999) (**Fig. 3.5**). For the Grt-Cld-Tlc schist, the effective bulk rock composition of sample #10-16 was used (Meyer et al., 2014). The Theriak-Domino thermodynamic software (Capitani and Petrakakis, 2010) and the recent version of the Holland and Powell (2011) thermodynamic dataset was used to calculate the P-T pseudosections in the CaO-K<sub>2</sub>O-FeO-MgO-Al<sub>2</sub>O<sub>3</sub>-SiO<sub>2</sub>-H<sub>2</sub>O (CKFMASH) and Na<sub>2</sub>O-CaO-K<sub>2</sub>O-FeO-MgO-Al<sub>2</sub>O<sub>3</sub>-SiO<sub>2</sub>-H<sub>2</sub>O (NCKFMASH) model systems with activity models for chloritoid (White et al., 2000), garnet (White et al., 2007), clinopyroxene (Green et al., 2007), amphibole (Diener and Powell, 2012), talc (Holland and Powell, 1998), white mica (Coggon and Holland, 2002), chlorite (Holland et al., 1998), and feldspar (Baldwin et al., 2005). Pure end-member mineral phases include lawsonite, kyanite, quartz/coesite, and water, which was set to be in excess, i.e., all the reactions were considered at water saturated conditions. The P-T range of each pseudosection covers 1.0–3.5 GPa and 450–650 °C.

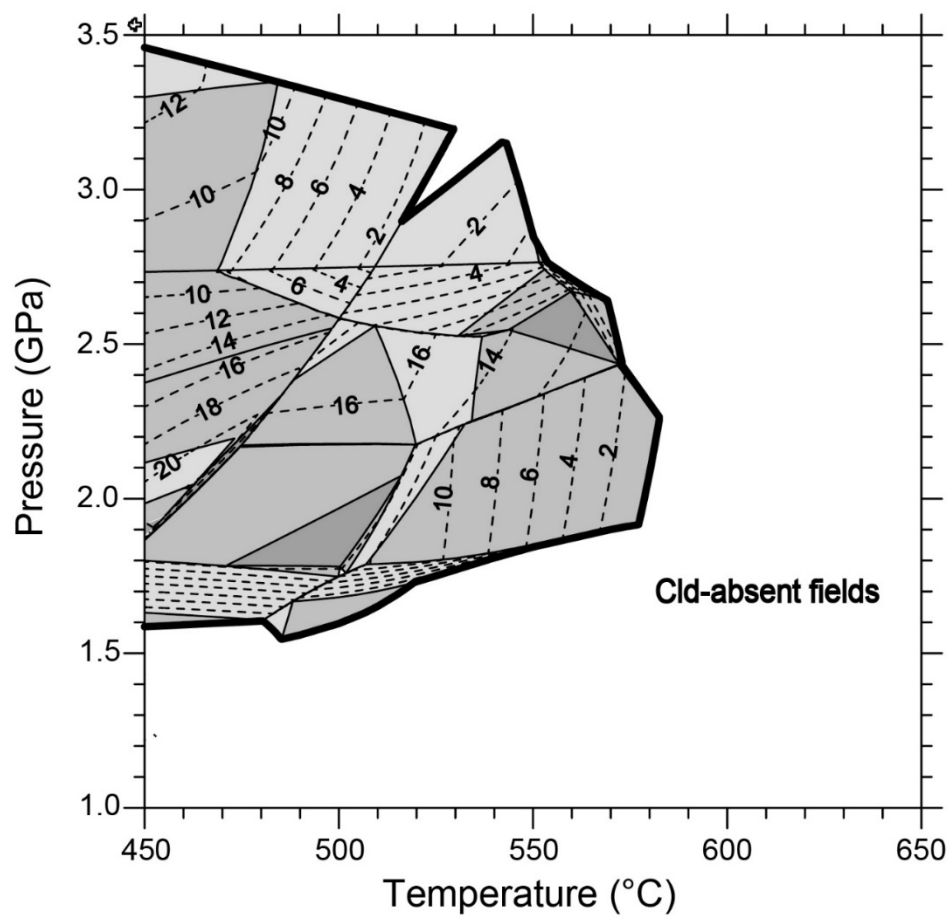
(a) P-T pseudosection of an average of 18 metapelites  
(Shaw et al., 1956)



- |                                |                                  |
|--------------------------------|----------------------------------|
| 1: Om + Ms + Car + Tz + Lw     | 15: Chl + Ms + Pgn + Lw          |
| 2: G + Om + Car + Ms + Tz + Lw | 16: Chl + Ms + Pgn + Gln + Lw    |
| 3: G + Om + Car + Ms + Tz + Lw | 17: G + Chl + Ms + Pgn + Lw      |
| 4: G + Om + Car + Ms + Lw      | 18: G + Chl + Ms + Pgn           |
| 5: G + Om + Car + Ms + Ky + Lw | 19: G + Chl + Ms + Pgn + Gln     |
| 6: G + Om + Car + Ms + Ky      | 20: Chl + Ms + Pgn + Z           |
| 7: G + Om + Car + Ms + Ky      | 21: G + Chl + Ms + Pgn + Z       |
| 8: G + Om + Ms + Ky            | 22: Chl + Ms + Pgn + Gln + Z     |
| 9: G + Om + Ms + Ky            | 23: G + Chl + Ms + Pgn + Gln + Z |
| 10: G + Om + Ms + Gln + Ky     | 24: Chl + Ms + Pgn + Bt + Z      |
| 11: G + Ms + Pgn + Gln + Ky    | 25: G + Chl + Ms + Pgn + Bt + Z  |
| 12: G + Om + Ms + Pgn          | 26: G + Chl + Ms + Pgn + Bt      |
| 13: G + Om + Ms + Pgn + Gln    | 27: G + Ms + Pgn + Bt            |
| 14: G + Ms + Pgn + Gln         | 28: Fls + G + Ms + Pgn + Bt      |

(Continued)

(b) Volume percent of chloritoid (vol. %)



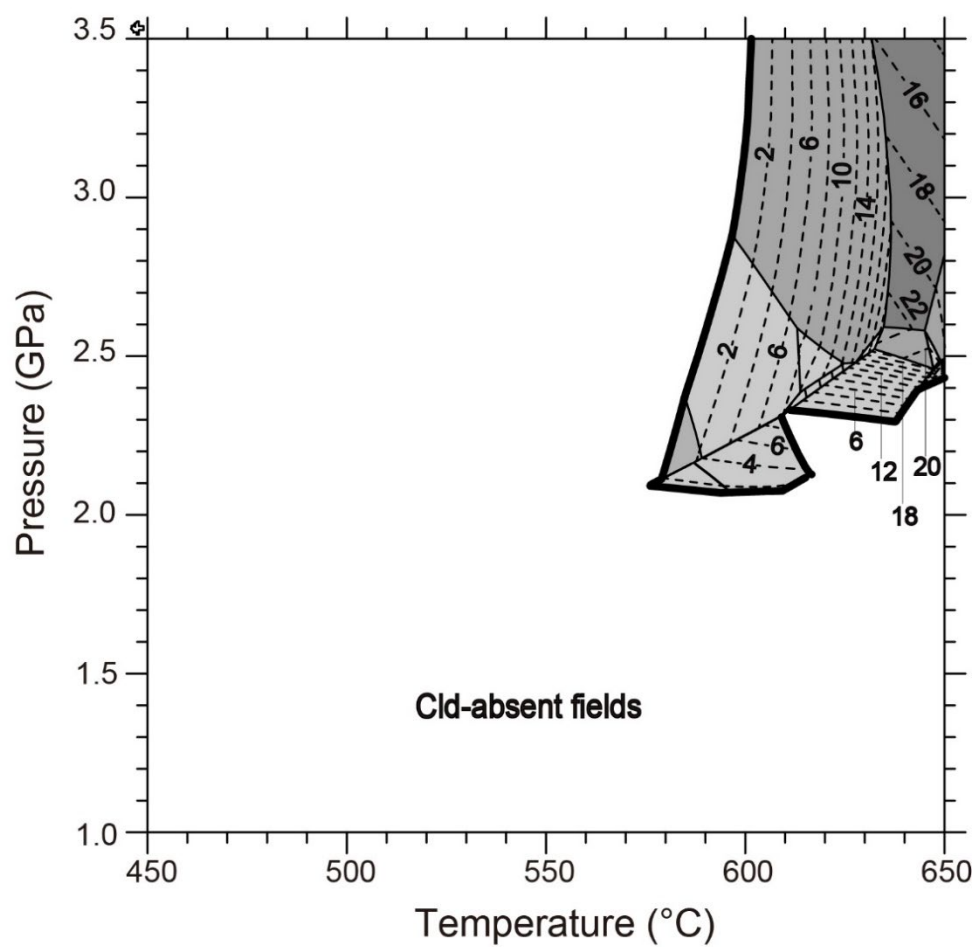
(Caption in the next page)

**Figure 3.4 (a)** P-T pseudosection calculated for an average composition of 18 published metapelites from Shaw (1956) in the model system NCKFMASH. Bulk composition in mol.%: SiO<sub>2</sub>, 71.7; Al<sub>2</sub>O<sub>3</sub>, 13.3; FeO, 6.8; MgO, 3.5; CaO, 0.6; K<sub>2</sub>O, 2.7; Na<sub>2</sub>O, 1.5, H<sub>2</sub>O is excess. Thick dashed lines denote the geothermal gradients at 5 °C/km and 10 °C/km, respectively. Simplified chloritoid-out reaction is indicated by the thicker line. Mineral abbreviation: Cld; chloritoid, G; garnet, Chl; chlorite, Ms; muscovite, Gln; glaucophane, Pgs; pargasite, Pgn; paragonite, Bt; biotite, Lw; lawsonite, Ky; kyanite, Car; carpolite, Z; zoisite. **(b)** Modal volume percentages of chloritoid (vol.%).

- (Continued)

(b)

Volume percent of chloritoid (vol. %)



(Caption in the next page)

**Figure 3.5 (a)** P-T pseudosection calculated for a Mg-Al metagabbro from Messiga et al. (1999) (sample MOE11B) in the model system NCFMASH. Bulk composition in mol.%: SiO<sub>2</sub>, 48.8; Al<sub>2</sub>O<sub>3</sub>, 13.5; Fe<sub>2</sub>O<sub>3</sub>, 2.0; MgO, 21.0; CaO, 11.5; Na<sub>2</sub>O, 3.3; H<sub>2</sub>O is excess. Thick dashed lines denote the geothermal gradients at 5 °C/km and 10 °C/km, respectively, in subduction zones. Simplified chloritoid-out reaction is indicated by the thicker line. Mineral abbreviation: Cld; chloritoid, G; garnet, Om; omphacite, Chl; chlorite. Gln: glaucophane, Pgs; pargasite, Pgn; paragonite, Edn; edenite, Bt; biotite, Lw; lawsonite, Ky; kyanite, Car; Mg-carnopolite, Q; quartz, Z; zoisite. **(b)** Modal volume percentages of chloritoid (vol.%).

### 3.3 Results

#### 3.3.1 CPOs of chloritoid

The chloritoid CPOs are all characterized by a strong alignment of the [001] axes subnormal to the foliation (**Fig. 3.6**). The strongest chloritoid CPO in sample #15R is characterized by the concentration maxima of the [100] axes subparallel to the foliation and subnormal to the lineation, and by the (010) poles subparallel to the lineation. The chloritoid CPO in sample #15R exhibits high J-index (11.16) and M-index (0.17). In samples #10-16 and #12-52, chloritoid showed a weak CPO of the [001] axes subnormal to the foliation and a weak girdle distribution of the [100] axes and (010) poles subparallel to the foliation. The chloritoid CPO of samples #10-16 and #12-52 showed relatively low J-indices (5.90 and 3.31) and M-indices (0.07 and 0.08).



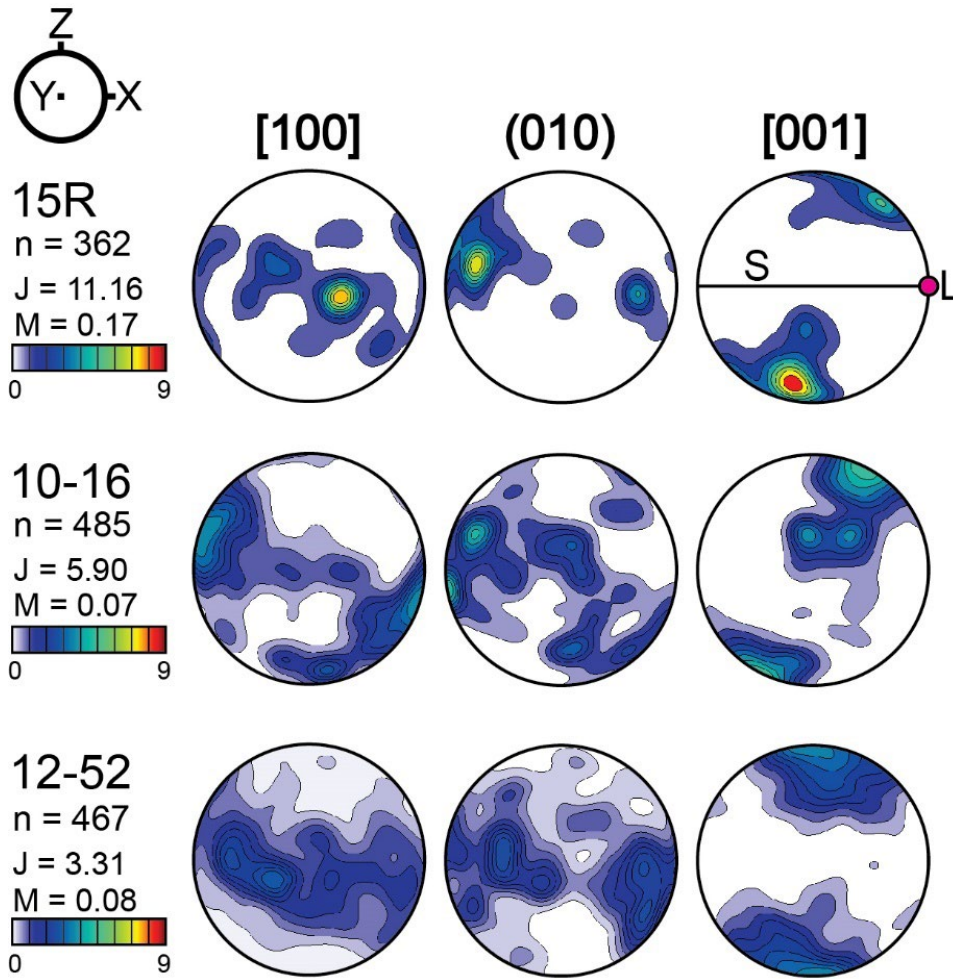


**Figure 3.6** Pole figures showing the CPO of chloritoid in the three UHP Makbal schist samples. Pole figures are presented in the lower hemisphere using an equal area projection. Pole figure density is shown with colorbar in units of multiples of a random distribution. Fabric strengths are also presented as J-index (J) and M-index (M). The X-direction is parallel to the lineation (L), Z-direction normal to the foliation (S), and the Y-direction orthogonal to the X- and Z-direction. To the left of the pole figures, n represents the number of the analyzed grains.

### 3.3.2 Elastic constant and seismic anisotropy of chloritoid

The elastic anisotropy of the single-crystal chloritoid was calculated by using the elastic constant ( $C_{ij}$ ) obtained by *first principles* simulation at ambient pressure conditions ( $P = 0$  GPa) (**Table 3.1 and Fig. 3.3**). The elastic constants show a similar anisotropy of stiffness components between the directions normal to the c-axis ( $C_{11}$ ,  $C_{22}$ ) and the c-axis direction ( $C_{33}$ ), and a strong anisotropy for the shear components associated with the c-axis ( $C_{66}$ ) and normal to this direction ( $C_{44}$ ,  $C_{55}$ ) (**Table 3.1**). The seismic velocities and seismic anisotropies of the single-crystal chloritoid for a given propagation direction were calculated from the  $C_{ij}$ , the contoured stereograms of the P-wave velocity ( $V_P$ ), the percentage shear wave anisotropy ( $AV_S$ ), and the polarization directions of the fastest S-wave ( $V_{S1}$  pol.) for ambient pressures (**Fig. 3.3**). The pattern of the  $V_P$  showed high velocities (maximum  $V_P = 9.8$  km/s) normal to the c-axis, and low velocities (minimum  $V_P = 7.9$  km/s) oblique to the c-axis, displaying a high seismic P-wave anisotropy ( $AV_P = 21.9\%$  and  $19.4\%$  for the GGA and LDA, respectively). The  $AV_S$  normal to the c-axis exhibits maximum  $AV_S = 46.5\%$  and  $49.2\%$  for the GGA and LDA respectively. The  $AV_S$  parallel to the c-axis exhibits a minimum  $AV_S$  of  $0.6\%$  and  $0.1\%$  for the GGA and LDA respectively. The fast S-wave has a polarization in the basal plane, which is typical for layered silicates (e.g. Morales et al., 2013). However, the elastic constants predicted by the LDA are stiffer than those using the GGA, while the elastic anisotropies predicted by the GGA and LDA are similar (**Fig. 3.3 and Table 3.1**).

The seismic anisotropies of the P- and S-waves of the polycrystalline chloritoid were calculated (**Fig. 3.7**) by using the elastic stiffness constant (**Table 3.1**) and the CPOs of chloritoid (**Fig. 3.6**). The magnitudes of the seismic anisotropies of the polycrystalline chloritoid are large (up to  $AV_P = 10.3\%$ ) for the P-waves (sample #15R) and larger (up to  $AV_S = 18.1\%$ ) for the S-waves (sample #15R) (**Fig. 3.7**). The seismic anisotropy of the S-waves is high at angles shallow to the foliation and at a maximum subparallel to the lineation (flow direction) (samples #15R and #10-16), where the polarization direction of the fast S-wave ( $V_{S1}$ ) is nearly perpendicular to the lineation (X-direction).

The fast S-wave polarization direction of the chloritoid strongly depends on the wave propagation direction (**Fig. 3.7**). As the ray path proceeds far-off the Z-direction and close to the direction parallel to the foliation, the polarization direction varies from oblique to nearly perpendicular to the rock lineation (X) (**Fig. 3.7**).

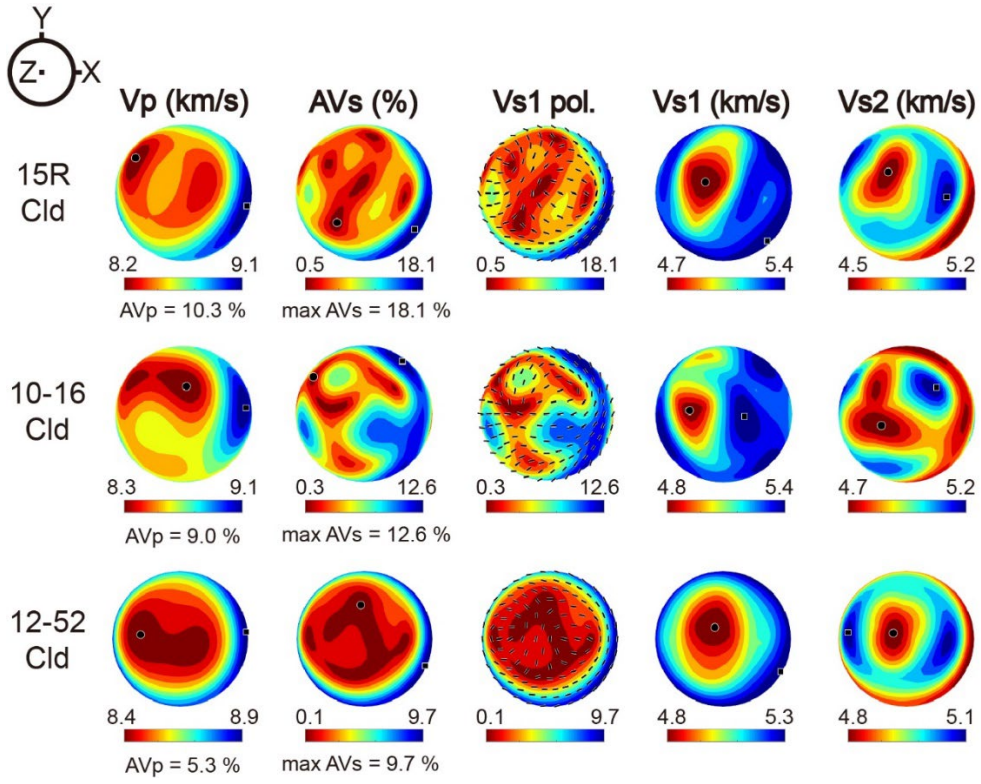


**Figure 3.7** Seismic anisotropies of polycrystalline chloritoid in the UHP Makbal schist samples. The elastic anisotropy using GGA method (**Fig. 3.3**) was applied to the calculation (see Method section). The P-wave anisotropy is up to  $AV_P = 10.3\%$  (sample #15R), and the S-wave anisotropy is up to  $AV_S = 18.1\%$  (sample #15R). The anisotropy is shown on a stereonet, in which the centre of a plot (Z) represents the direction normal to the foliation (X-Y plane), and X corresponds to the lineation.  $V_P$ : P-wave velocity,  $AV_S$ : shear wave anisotropy,  $V_{S1}$  pol: polarization direction of the fast S-wave,  $V_{S1}$ : fast S-wave velocity,  $V_{S2}$ : slow S-wave velocity.

The bulk rock seismic anisotropies of the three Grt-Cld-Tlc schist samples were estimated (**Fig. 3.8**) by averaging the elastic constant of the mineral aggregate, considering the CPOs of the chloritoid and other composite minerals (such as garnet, talc, etc.), their individual single-crystal elastic constant, the densities of the individual phases, and the modal volume percentages of the sample (**Table 2.1**). The magnitudes of the whole-rock seismic anisotropies were found to be very large for the P-waves (up to  $AV_P = 28.1\%$ ) and large for the S-waves (up to  $AV_S = 15.5\%$ ). For all three Grt-Cld-Tlc schist samples, the entire rock  $AV_P$  ( $AV_P = 14.7\text{--}28.1\%$ ) is higher than that of the chloritoid aggregates ( $AV_P = 5.3\text{--}10.3\%$ ). On the other hand, the maximum whole rock  $AV_S$  of samples #15R and #12-52 (max  $AV_S = 15.5\%$  and  $7.0\%$ , respectively) is lower than that of the chloritoid aggregates (max  $AV_S = 18.1\%$  and  $9.7\%$ , respectively). The maximum whole rock  $AV_S$  (max  $AV_S = 14.5\%$ ) of sample #10-16 is higher than that of the chloritoid aggregates (max  $AV_S = 12.6\%$ ). The pattern of the  $V_{S1}$  polarization direction of the bulk rocks is very similar to that of the chloritoid aggregates.

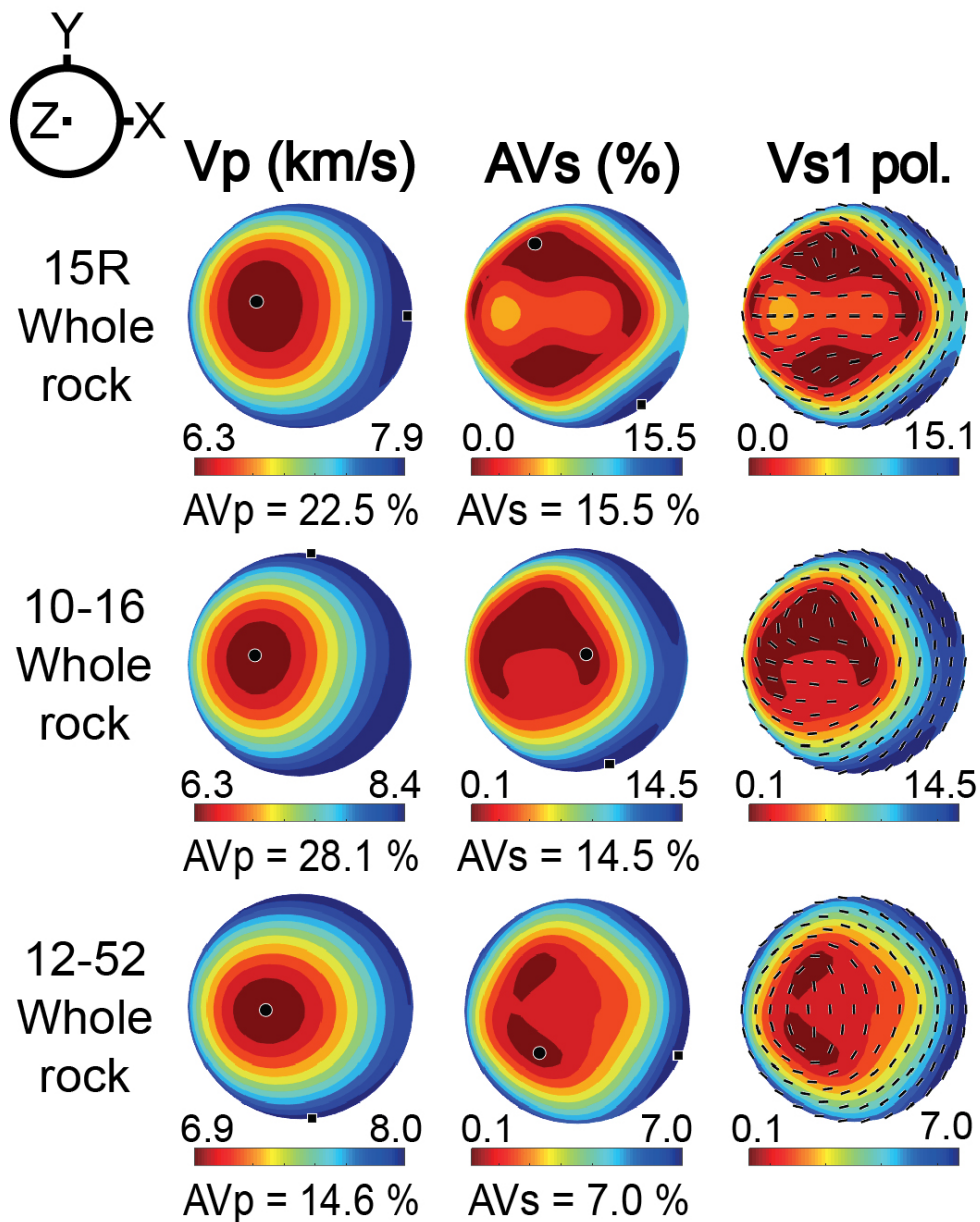


**Figure 3.8** Bulk seismic anisotropy of the whole rock. The modal composition given in **Table 2.1** was used, along with the elastic constants of the composite minerals at ambient pressure and the CPOs of each polycrystalline mineral. Reference frame and abbreviations are the same as those in **Fig. 3.7**.

### 3.3.3 Thermodynamic stability and modal abundance of chloritoid

The P-T pseudosection of the Grt-Cld-Tlc schist (sample #10-16) calculated in this study shows that chloritoid is thermodynamically stable in the temperature range of 450–600 °C (**Fig. 3.9a**). The modal abundance of chloritoid was calculated for the three different bulk compositions (**Figs. 3.4, 3.5 and 3.9b**). The calculations for the Grt-Cld-Tlc schist revealed that the highest amount of chloritoid was 28 vol.% within the given P-T conditions, which is in good agreement with the observed amount of chloritoid in the samples studied here (20–25 vol.% in samples #10-16 and #12-52) (**Fig. 3.9b**). The possible modal amounts of chloritoid in the average pelite (Shaw, 1956) and the Mg-Al metagabbro (Messiga et al., 1999) are up to 20 vol.% and 22 vol.%, respectively. The variation of the chloritoid modal volume shows the development of a complex pattern during pressure increase in all three rock types. Along cold subduction geotherms (5–10 °C/km), the maximum chloritoid amount reaches 26 vol.% (**Fig. 3.9b**), and is highest above the chlorite-out reactions in the Grt-Cld-Tlc schist (**Fig. 3.9**). In the Grt-Cld-Tlc schist, chloritoid is stable at < 600 °C and its amount generally decreases with increasing P-T conditions (**Fig. 3.9**). Other hydrous minerals stable with chloritoid are chlorite, lawsonite, talc, mica, Mg-carpholite, and zoisite. When considering the average pelitic composition, the stability field of chloritoid is constrained to be at  $P > 1.5$  GPa and  $T < 580$  °C (**Fig. 3.4**). Hydrous minerals stable with chloritoid are chlorite, glaucophane, lawsonite, mica, and carpholite. When considering the Mg-Al gabbro composition, chloritoid occurs at relatively high P-T conditions ( $P > 2$  GPa and  $T > 570$  °C) (**Fig.**

**3.5).** Other hydrous minerals stable with chloritoid are chlorite, glaucophane, lawsonite, and zoisite.

## **3.4 Discussion**

### **3.4.1 CPO development of chloritoid**

A strong alignment of the [001] axes of the chloritoid was observed in the UHP schist samples from the Makbal Complex. This is consistent with findings of Haerinck et al. (2015), although they used a different analyzing method for the fabric measurement (synchrotron X-ray diffraction) on only one chloritoid-bearing sample.

The flattening type of fabric is prevalent in previous studies of layered silicates (e.g. Dempsey et al., 2011; Lloyd et al., 2009; Wenk et al., 2010). The basal glide is a dominant deformation mechanism for most phyllosilicates, allowing the basal (001) planes to occur parallel to the rock foliation or the cleavage planes (Wenk et al., 2010). Although chloritoid is classified as orthosilicate, it commonly exhibits the physical and structural properties of phyllosilicates due to the layered structure, which consists of octahedral sheets bonded by layers of isolated silicate tetrahedra (Klein, 2002; Nesse, 2009). The basal glide could, therefore, be a plausible deformation mechanism of the chloritoid. An alternative explanation is the formation of the chloritoid CPO by dislocation creep, manifested by undulose extinction of the chloritoid in sample #10-16 (**Fig. 3.2**).



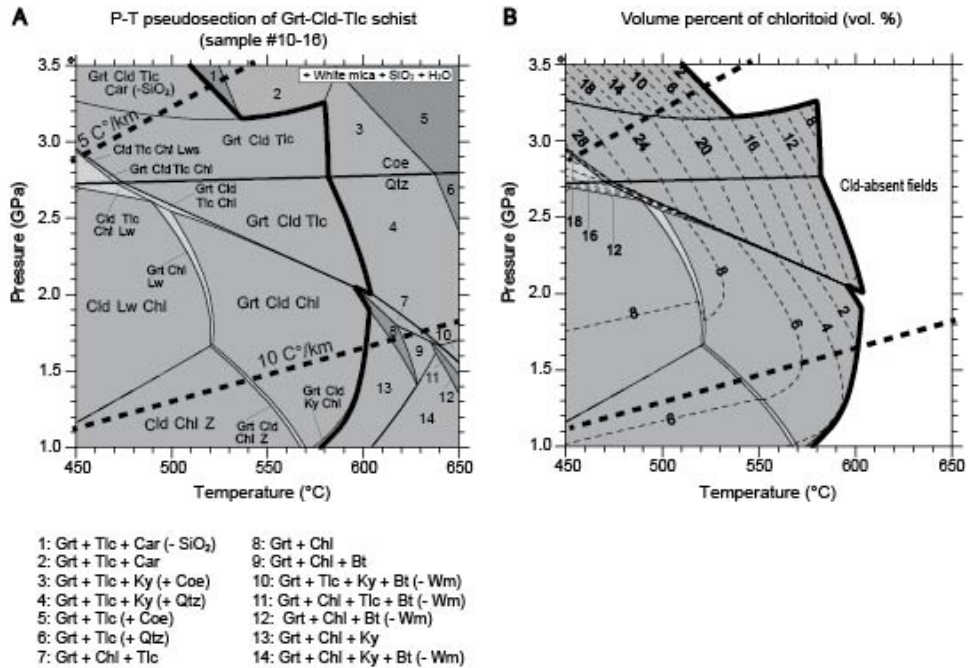


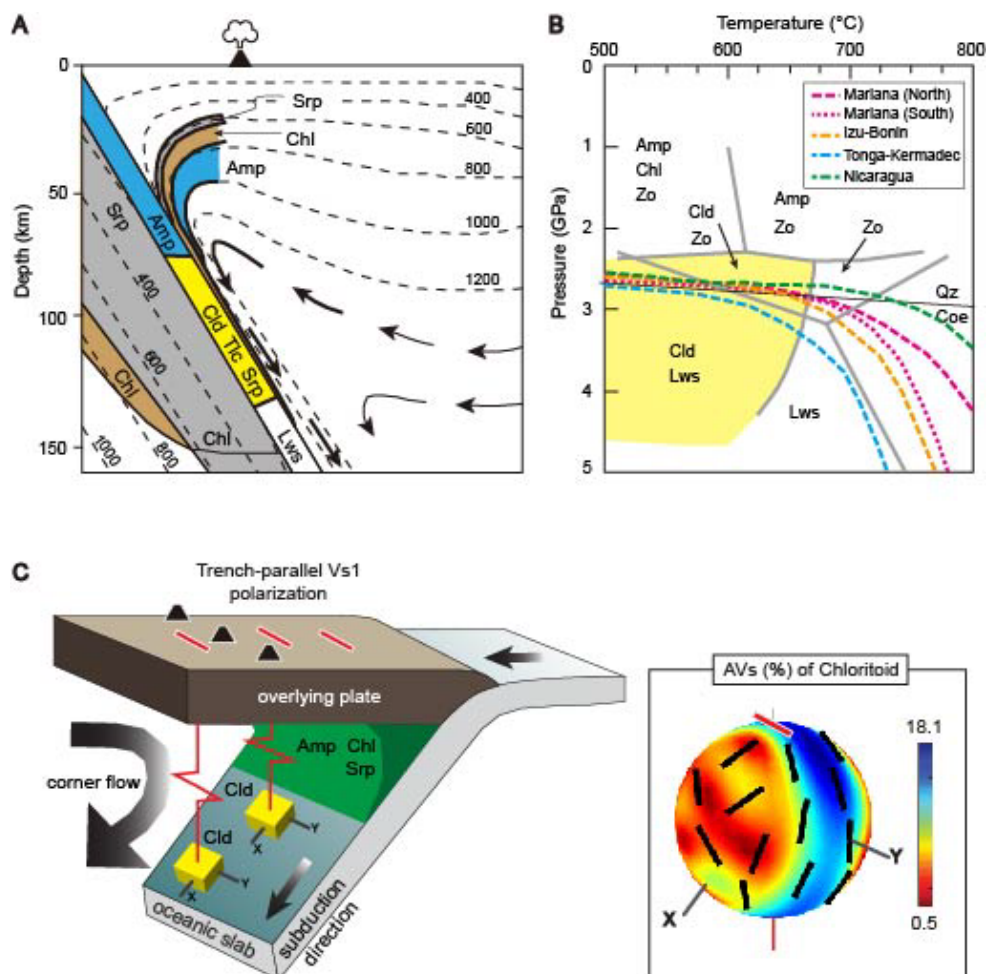
**Figure 3.9** P-T pseudosection showing the chloritoid-stability fields and the volume percentage isopleths of chloritoid. **(a)** P-T pseudosection calculated for the Grt-Cld-Tlc schist (sample #10-16) in the model system CKFMASH. Bulk composition in mol%: SiO<sub>2</sub>, 49.0; Al<sub>2</sub>O<sub>3</sub>, 11.0; FeO, 17.0; MgO, 22.5; CaO, 0.2; K<sub>2</sub>O, 0.2; H<sub>2</sub>O is excess. Dashed bold lines denote the geothermal gradients of 5 °C/km and 10 °C/km, respectively. Chloritoid-out curve is indicated by solid bold line. Mineral abbreviation: Grt, garnet; Cld, chloritoid; Tlc, talc; Chl, chlorite; Wm, white mica; Bt, biotite; Lw, lawsonite; Ky, kyanite; Car, carpholite; Z, zoisite. **(b)** Volume percentage isopleths of chloritoid. The geothermal gradients are the same as in **(a)**.

### 3.4.2 Chloritoid stability and its implication for seismic anisotropy in subduction zones

A strong trench-parallel seismic anisotropy of S-waves has been observed in many subduction zones such as Ryukyu, Izu-Bonin, Mariana, and Tonga (Long, 2013 and references therein). An anisotropic fore-arc mantle has been proposed as the major source in terms of the B-type CPO of olivine in the hydrated mantle (Jung and Karato, 2001; Jung et al., 2006; Karato et al., 2008; Kneller et al., 2005; Nagaya et al., 2014), the trench-parallel flow in the sub-slab mantle (Russo and Silver, 1994), the pressure-induced olivine CPO (Jung et al., 2009; Lee and Jung, 2015; Ohuchi et al., 2011), and the strong CPO of hydro-phyllsilicates (Ha et al., 2018; Jung, 2017; Katayama et al., 2009; Lee et al., 2020; Nagaya et al., 2016). However, the strong seismic anisotropy in some subduction zones cannot be solely due to the CPO of olivine (Wirth and Long, 2012). Recent geodynamic studies using realistic slab parameters showed that pure trench-parallel flow is unlikely to be dominant in the sub-slab mantle (e.g. Alisic et al., 2012). The CPO of anisotropic hydrous minerals in subduction zones may, therefore, be an important manifestation in the trench-parallel seismic anisotropy.

Thermodynamic phase stability indicates that chloritoid is likely to be stable between a depth range of 80–120 km in subducting hydrated MORB (Schmidt and Poli, 1998) (**Fig. 3.10a**). The slab geotherms in steeply dipping subduction zones such as the Mariana (slab-dip angle = 57–62°), the Izu-Bonin (slab-dip angle = 46–63°), the Tonga-Kermadec (slab-dip angle = 52–56°), and the Nicaragua (slab-dip

angle =  $62^{\circ}$ ) (Syracuse et al., 2010) settings, which display a strong trench-parallel seismic anisotropy, suggest that chloritoid is likely to be stable along the interface of the overlying mantle wedge and the hydrated oceanic slab at a depth range between 80 and 120 km (**Fig. 3.10b**) (Schmidt and Poli, 1998; Syracuse et al., 2010). Recent studies suggest that the subducting oceanic crust and the slab-mantle interface are pervasively hydrated (Abers et al., 2017) and thus might be an important source of the trench-parallel anisotropy (Huang et al., 2011).



(Caption in the next page)

**Figure 3.10 (a)** Schematic diagram illustrating a subducting slab with a dipping angle of  $60^\circ$ . Also shown are the thermodynamic stability fields of hydrous phases in the hydrated peridotitic layer, overlying the oceanic crystal layer and the mantle wedge region (modified after Schmidt and Poli, 1998). Stippled lines are isotherms and arrows indicate flow lines in the mantle wedge. **(b)** Pressure-temperature stability fields of hydrous phases in hydrated MORB under subduction zone conditions (modified after Schmidt and Poli, 1998). Dashed lines are the P-T paths of the slab surface for the Mariana, Izu-Bonin, Tonga-Kermadec and Nicaragua settings (Syracuse et al., 2010). Yellow shaded region indicates the stability field of chloritoid based on the pseudosection modelling conducted here (**Figs. 3.4, 3.5 and 3.9**) and also on previous estimates (Schmidt and Poli, 1998). **(c)** Schematic diagram of a subduction zone illustrates the influence of the chloritoid CPO on the seismic anisotropy in the subduction zone. The applied slab-dip is  $60^\circ$  (rotation around the axis parallel to the Y-direction; see the discussion) and the lineation (X-direction) is assumed to be parallel to the subduction direction. Red bars represent the polarization direction of the fast S-wave. Inset figure shows shear wave anisotropy ( $AV_s$ ) and the polarization directions of fast S-waves (red and black bars) going through the chloritoid aggregates (sample #15R). X and Z represent the lineation (flow direction) and the direction perpendicular to the foliation (flow plane), respectively.

To evaluate the effect of chloritoid on the seismic anisotropy observed in subduction zones, the 3-dimensional seismic anisotropy pattern of chloritoid aggregates was calculated using the chloritoid CPO of sample #15R (**Fig. 3.10c**), which showed the strongest  $AV_s$  (up to ~18%) among the samples analyzed here. In the present study, the subduction zone setting was simplified by using a 2-D corner (slab-parallel) flow model that resulted from viscous coupling between the downgoing slab and the overlying mantle (van Keken et al., 2002). Thus, the respective slab-dip angle was applied to the chloritoid CPO and the seismic anisotropy pattern by rotation around the axis parallel to the Y-direction, which is normal to the lineation parallel to the downgoing flow direction (**Fig. 3.10c**). The higher the slab-dip angle, the higher is the strength of the  $AV_s$  using the chloritoid aggregate, which most likely also causes a longer delay time  $> 0.2$  s at a dip-angle  $\theta > 45^\circ$ . Subduction zones that show strong trench-parallel S-wave anisotropies (with a long delay time of up to 1–2 s) are also characterized by large dipping slab angles of  $40\text{--}60^\circ$  as displayed by the Ryukyu, Mariana, Izu-Bonin and Tonga subduction zone settings (Long and Silver, 2008). For example, the Tonga and Mariana slabs have steep subducting angles ( $50\text{--}70^\circ$ ) and show a strong trench-parallel seismic anisotropy under the forearc and arc regions (Pozgay et al., 2007; Smith et al., 2001). Since the  $AV_s$  pattern of the polycrystalline chloritoid was controlled by the chloritoid CPO and implied an importance of high-angle slab dip geometry (**Fig. 3.10c**), the effect of the chloritoid CPO on the seismic anisotropy is thought to be important in cold and high-angle subduction zones.

### 3.4.3 Effect of chloritoid CPO on seismic anisotropy of the Grt-Cld-Tlc schist

Garnet is one of the major minerals in the Grt-Cld-Tlc schists, and is seismically nearly isotropic ( $AV_P = 0.5\%$ ,  $\max AV_S = 1.2\%$  of single garnet crystal) (Babuška et al., 1978). Chloritoid and talc, which are the other major constituent minerals in the Grt-Cld-Tlc schist, are hydrous layered silicates and are elastically anisotropic. Talc in particular has been shown to be an important mineral that influences the strong trench-parallel seismic anisotropy of hydrated slab–mantle interfaces (Lee et al., 2020; Nagaya et al., 2020). The bulk seismic anisotropies of the three Grt-Cld-Tlc schist samples studied here (#15R, #10-16, and #12-52) were determined in an earlier study (Lee et al., 2020), which, however, did not consider the chloritoid CPO due to the lack of elasticity data of single chloritoid crystal at that time. Using the new elasticity data of single-crystal chloritoid and the CPO of chloritoid aggregates, I calculated the complete bulk seismic anisotropy of the Grt-Cld-Tlc schist samples in this study (**Fig. 3.8**). The integration of the chloritoid CPO and its volume fraction revealed that the chloritoid CPOs caused a weakening of the bulk P-wave seismic anisotropies of the Grt-Cld-Tlc schist ( $AV_P = 14.6\text{--}28.1\%$ ) when compared to those determined in the former ‘chloritoid-absent’ whole rock ( $AV_P = 19.1\text{--}31.2\%$ ) study of Lee et al. (2020). This is thought to be associated with the significantly lower P-wave seismic anisotropies of the chloritoid aggregates ( $AV_P = 5.3\text{--}10.3\%$ ), seeing the much higher P-wave seismic anisotropies ( $AV_P = 67.3\text{--}72.3\%$ ) of the abundant talc aggregates (Lee et al., 2020). On the other hand, the chloritoid CPO slightly increased the maximum  $AV_S$  of the entire rock samples #15R

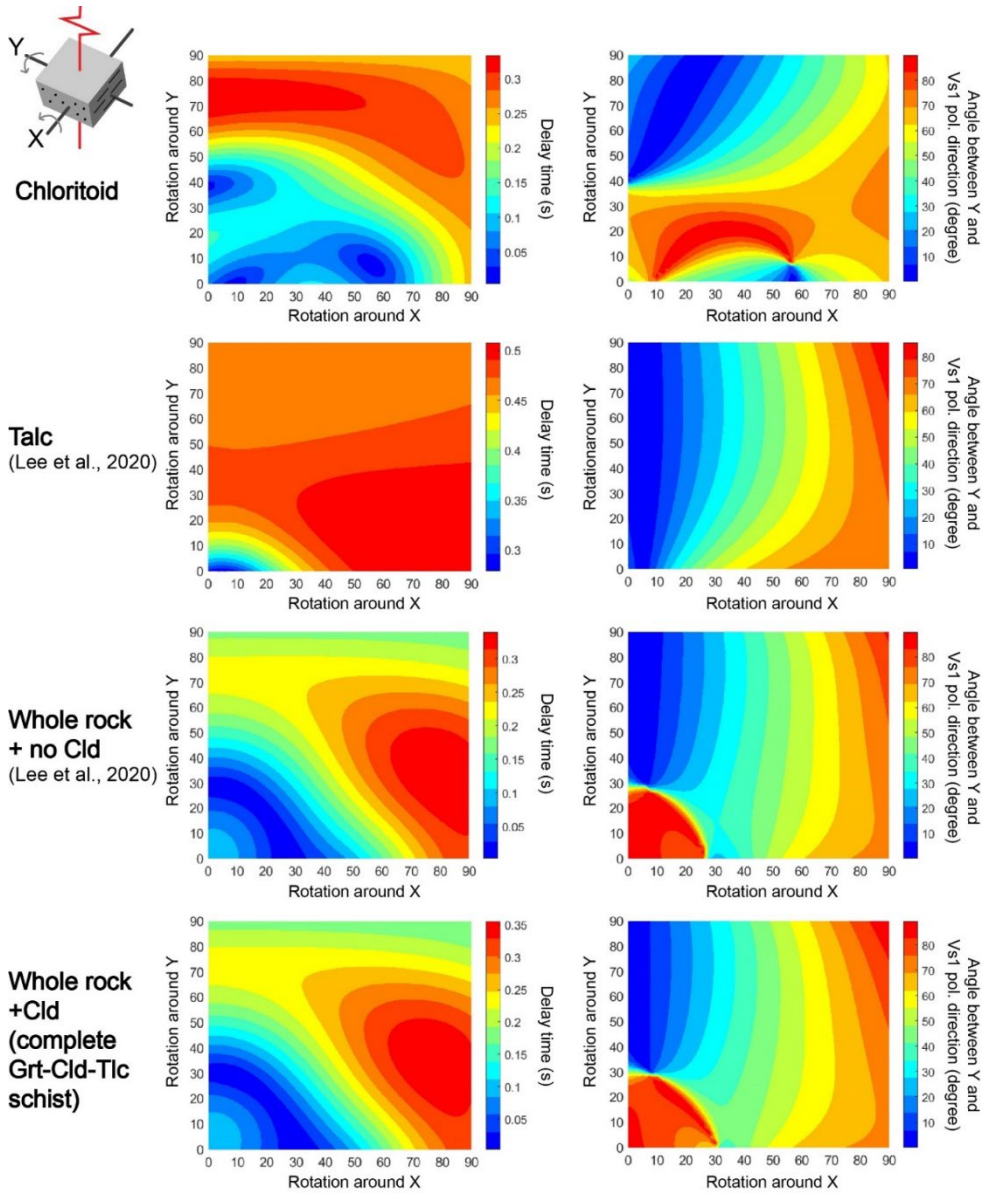
and #12-52, and decreased that of sample #10-16 (Lee et al., 2020). This observation indicates that the whole rock mineral assemblage is important to determine the role of chloritoid in the whole rock S-wave anisotropy.

I used sample #15R, which displayed the strongest chloritoid CPO (**Fig. 3.6**), to calculate the effect of the slab-dip angle and the sample geometries on the ray path of a vertically incident S-wave through chloritoid and the entire rock specimen (**Fig. 3.11**). The sample geometry is defined with respect to the sample foliation (X-Y plane normal to Z) and sample lineation (X). The values approaching  $0^\circ$  correspond to the trench-parallel  $V_{S1}$  polarization direction, and those approaching  $90^\circ$  to the trench-normal  $V_{S1}$  polarization direction (see right column of **Fig. 3.11**). These calculations revealed that under broad sample geometry conditions, the talc CPO produced a longer delay time than the chloritoid CPO. The maximum delay time generated by chloritoid is  $\sim 70\%$  of that generated by talc.

Chloritoid CPO showed trench-parallel  $V_{S1}$  polarization direction at dip-angle  $> 40^\circ$  (**Fig. 3.11**). Talc CPO showed trench-parallel  $V_{S1}$  polarization direction at all dip-angles from slab subduction to vertical subduction, if the foliation of talc layer is subparallel (rotation about X-direction =  $0-20^\circ$ ) (**Fig. 3.11**). In the Grt-Cld-Tlc schist, a trench-parallel  $V_{S1}$  polarization direction is achieved when the shear plane dips at an angle  $> 30^\circ$  from the horizontal plane (i.e., rotation around the Y direction is greater than  $30^\circ$ ). When rotating the shear plane around the shear direction at an angle lower than  $30^\circ$ , the  $V_{S1}$  polarization direction is normal to the trench. The maximum delay time ( $\sim 0.4$  s) of the Grt-Cld-Tlc schist is generated when the shear plane is dipping  $< 50^\circ$  and its rotation around the shear direction is  $> 60^\circ$ .



(**Fig. 3.11**), resulting in a trench-normal  $V_{S1}$  polarization direction of the Grt-Cld-Tlc schist. However, When the shear plane dipped at an angle  $>30^\circ$  (i.e., rotation about the Y-direction  $> 30^\circ$ ), the variation of the whole rock  $V_{S1}$  polarization direction is similar to that of the talc aggregate when using a shear plane dip angle  $> 30^\circ$  (i.e., rotation about the Y-direction  $> 30^\circ$ ). Overall, it was observed that the geometries of the S-wave anisotropy of the Grt-Cld-Tlc schist is significantly more influenced by the talc CPO than by the chloritoid CPO.

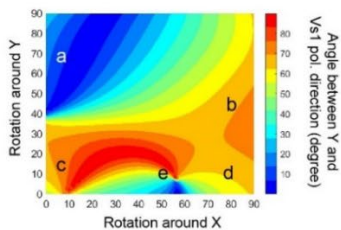
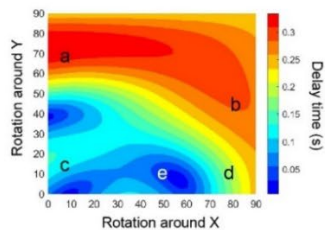
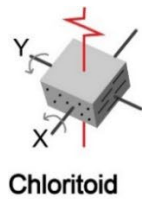


(Caption in the next page)

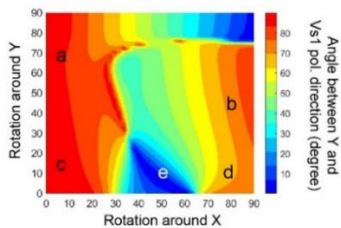
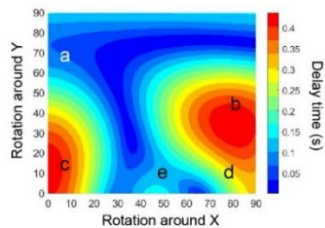
**Figure 3.11** Illustration of the 3-D effect of chloritoid, talc and the Grt-Cld-Tlc schist on a vertically incident S-wave. CPO data of garnet and talc (Lee et al., 2020) and chloritoid (this study) of sample #15R were used for the calculation. An anisotropic layer with a thickness of 10 km was assumed. The rotation around X and Y from 0° to 90° was illustrated to display the effect of the dipping foliation (X-Y plane) where X is parallel to the shear direction and Y is parallel to the strike of the hypothetical trench. The left column shows contour plots displaying the effect of sample orientation on the delay time (dt), with blue (short delay times) to red (long delay times) colors. The right column shows contour plots displaying the variation of the angle between the fast S-wave polarization direction ( $V_{SI}$  pol. direction) and the hypothetical strike of the trench (Y) as the sample is rotated around X and Y. Colors range from blue (trench-parallel fast directions) to red (trench-normal fast directions). In the uppermost left, the schematic sample geometry is illustrated to show how the sample (X-Y plane = foliation, dots, and lines = lineation) is rotated with respect to the incoming S-waves (red line).

### 3.4.4 Effect of hydrous minerals in blueschist-facies rock on seismic anisotropy

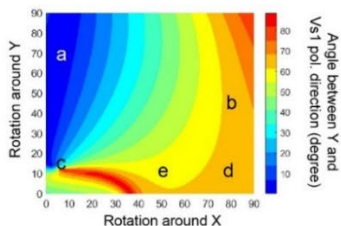
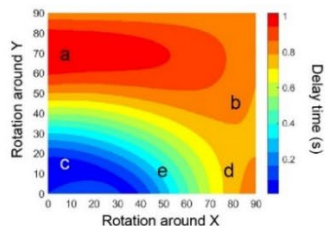
Considering previous geothermobarometrical studies (see Meyer et al., 2014 and references therein) and the pseudosections calculated here, chloritoid is found to be stable under high-pressure conditions ranging from the blueschist to the eclogite facies. The here calculated pseudosections for metapelites and metagabbros revealed that a number of hydrous minerals such as glaucophane (Gln), lawsonite (Lws), chlorite (Chl), and phengitic white mica (Ms) are stable with chloritoid under high-pressure conditions (**Figs. 3.4 and 3.5**). In order to compare the contributions of these minerals to the seismic anisotropy of a subducted slab, I calculated the delay time and the polarization directions of the fast S-waves, with a vertically incident S-wave ray path traveling through the hydrous minerals, and various sample geometries and slab-dip angles (**Fig. 3.12**). In addition, these data were compared with the whole-rock seismic anisotropy of a hypothetical blueschist, comprising the respective hydrous mineral assemblages (**Fig. 3.12**) with a modal composition of Gln:Lws:Chl:Phg:Cld = 30:25:15:15:15 (vol%). For sample geometry consistency, the foliations of the different rock samples were assumed to be parallel, and, furthermore, I followed the previously published original 2-D plots of the seismic anisotropy of both glaucophane and lawsonite (c.f. Cao et al., 2013; Choi et al., 2021). The magnitude of the seismic anisotropies and the S-wave velocities are summarized in **Table 3.2**.



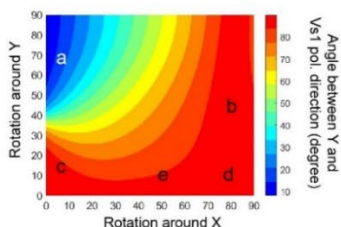
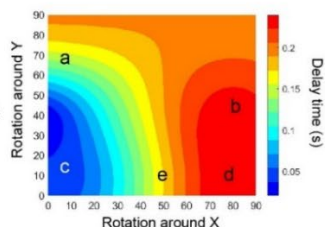
**Chlorite**



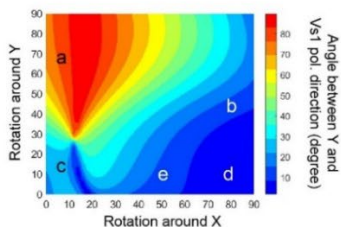
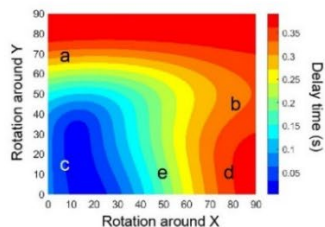
**Phengite**



**Glaucophane**

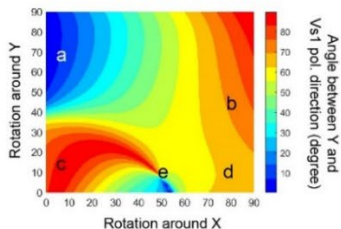
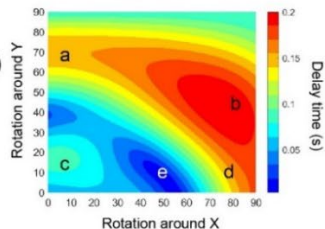


**Lawsonite**



**Blueschist  
(hypothetical)**

Gln 30 vol%  
Lws 25 vol%  
Cld 15 vol%  
Chl 15 vol%  
Phg 15 vol%



(Caption in the next page)

**Figure 3.12** Representation of the effect of the glaucophane, lawsonite, chlorite, phengite, and chloritoid on the delay time and fast S-wave polarization direction of a vertically incident S wave, and that of the bulk seismic anisotropy of a hypothetical blueschist, consisting of glaucophane (Gln):lawsonite (Lws):chlorite (Chl):phengite (Phg):chloritoid (Cld) = 30:25:15:15:15 (vol%). The CPO data of each polycrystalline mineral were obtained from previous studies on naturally deformed blueschists (glaucophane aggregate from Cao et al. (2013) and lawsonite aggregate from Choi et al. (2021)) and this study (CPOs of chlorite, phengite, and chloritoid in sample #15R). An anisotropic layer thickness of 10 km was assumed for consistency. The reference frame for the rotation and the sample orientation (schematics in the upper left) is the same as in **Fig. 3.11**. Color ranges describe the same parameters as in **Fig. 3.11** for both delay time and fast polarization direction. Symbols marked with “a”–“e” indicate five different ray paths and sample geometries.

The calculations demonstrated that the ray path (a, b, c, d, and e) and the sample geometries, which can generate a long delay time with the trench-parallel S-wave anisotropy, were different for the five hydrous minerals. The chloritoid and phengite CPOs produced their maximum delay time ( $\sim 0.3$  and  $\sim 1.0$  s, respectively) with a trench-parallel or -subparallel  $V_{S1}$  polarization direction, a steep dipping shear plane  $> 60^\circ$  (i.e., rotation around Y direction was greater than  $60^\circ$ ), and a shear plane rotation around the shear direction (i.e., rotation around the X-direction) at an angle lower than  $30^\circ$  (ray path “a” in **Fig. 3.12**). The chlorite CPO (cf. sample #15R) displayed its maximum delay time ( $\sim 0.4$  s) with a trench-normal  $V_{S1}$  polarization direction, a shear plane dip angle  $< 40^\circ$ , and a rotation angle of  $< 10^\circ$  or  $> 70^\circ$  around the shear direction (ray path near “c” and “d”, respectively in **Fig. 3.12**). The glaucophane CPO generated its maximum delay time ( $\sim 0.2$  s) with a trench-normal  $V_{S1}$  polarization direction, a shear plane dip-angle below  $\sim 40^\circ$  and a rotation angle  $> 70^\circ$  around the shear direction (ray path near “d” in **Fig. 3.12**). The lawsonite CPO generated its maximum delay time ( $\sim 0.4$  s) with a steep shear plane dip-angle greater than  $\sim 70^\circ$  (ray path from “a” to “b” in **Fig. 3.12**), or with a shear plane rotation around the shear direction at an angle of  $> 70^\circ$  (ray path from “b” to “d” in **Fig. 3.12**). The latter case corresponds to a high-angle fault present in subducting slabs. The lawsonite CPO also produced a trench-parallel anisotropy at a shear plane rotation angle  $> 50^\circ$  around the shear direction. Among the different minerals considered here, the chloritoid and phengite CPOs mainly contribute to the trench-parallel polarization of the  $V_{S1}$  with a long delay time (near the ray path “a” in a wide field of blue color in the right column plots in **Fig. 3.12**) at a large slab dip angle, corresponding to a cold and old subducted slab.

The hypothetical blueschist displayed the maximum delay time of  $\sim 0.2$  s, which is the shorter than that of all the composite minerals studied here (see the bottom of **Figure 3.12**). This is thought to be due to the following two characteristics: (1) the presence of large amounts of glaucophane, which displays the shortest maximum delay time of the minerals studied here, in the blueschist (**Fig. 3.12**), and (2) the low absolute values of the S-wave velocities of the polycrystalline phengite, lawsonite, and chlorite (**Table 3.2**). The presence of “slow” phengite (i.e. minimum  $V_{S1} = 3.2$  km/s and minimum  $V_{S2} = 2.9$  km/s) seems to significantly decrease the maximum S-wave velocity of the blueschist (**Table 3.2**), thereby causing a decrease of the maximum S-wave anisotropy and the shorter delay time of the blueschist (**Fig. 3.12**). Thus, the S-wave velocities of seismically anisotropic minerals such as chlorite and phengite with different velocity ranges may reduce the entire rock’s seismic anisotropy. In the present study, chloritoid is the only hydrous mineral ( $V_{S1} = 4.7\text{--}5.4$  km/s,  $V_{S2} = 4.5\text{--}5.2$  km/s) that displayed higher S-wave velocities than glaucophane ( $V_{S1} = 4.4\text{--}4.9$  km/s,  $V_{S2} = 4.3\text{--}4.5$  km/s) (**Table 3.2**).

The delay time pattern of the hypothetical blueschist was mostly similar to that of the chloritoid compared to the other hydrous minerals, i.e. long delay times were generated by the ray paths “a” and “b,” and short delay times by the ray paths “c” and “e,” with the shortest delay time along the ray path “e.” The pattern of the  $V_{S1}$  polarization direction of the blueschist was also similar to that of the chloritoid (**Fig. 3.12**). In order to generate trench-parallel polarization of the blueschist with a measurable delay time of  $> 0.1$  s near the ray path of “a,” a shear plane dip-angle of  $> \sim 50^\circ$  to a horizontal surface (i.e., rotation around the Y direction  $> 50^\circ$ ) was



required. Similar conditions were required to generate trench-parallel anisotropy in the CPOs of chloritoid, phengite, and glaucophane (**Fig. 3.12**). On the other hand, the trench-normal S-wave anisotropy with a measurable delay time of the blueschist is mostly affected by the CPO of the chlorite, phengite, and glaucophane near the ray path of “b”. Chloritoid and phengite mostly contribute to the S-wave anisotropy of blueschists and, can influence the trench-parallel anisotropy with a long delay time in cold subducting slabs.

### 3.5 Conclusion

The elastic anisotropy of chloritoid single-crystals was calculated for the first time and used to examine the seismic anisotropy for chloritoid-bearing rocks in subducting oceanic crust. The elastic stiffness tensor of single-crystal monoclinic chloritoid showed a high elastic anisotropy of chloritoid reflected by  $AV_P = 22\%$  and  $\max AV_S = 47\%$ . The CPO of the polycrystalline chloritoid from the UHP schists showed a strong alignment of the  $[001]$  axes of chloritoid subnormal to the foliation. The strongest chloritoid CPO showed a concentration or girdle distribution of the  $[100]$  axes and the  $(010)$  poles subparallel to the foliation. The re-evaluated stability field of the chloritoid revealed the stability of a significant amount of chloritoid in high-pressure and low-temperature subduction zones, particularly in Al-rich metapelites and metagabbros. The CPOs of the polycrystalline chloritoid produced a strong trench-parallel seismic anisotropy. The chloritoid CPOs tend to reduce the bulk seismic anisotropy of the Grt-Cld-Tlc schists due to their lower volume fraction and lower seismic anisotropy compared to other abundant hydrous minerals such as talc. However, depending on the mineral assemblage and slab geometry, chloritoid, in association with glaucophane and phengite, can influence the seismic anisotropy of blueschist-facies rocks in cold subduction zones.

# **CHAPTER 4. Deformation fabrics of diopside and antigorite in serpentinites and implications for seismic anisotropy in subduction zones**

## **Abstract**

Antigorite serpentinites have been known to contribute to the strong seismic anisotropy ubiquitously observed in worldwide subduction zones, especially because of the strong lattice preferred orientation (CPO) of antigorite in hydrated forearc mantle. Antigorite generally coexists with olivine and pyroxene in serpentinites, and diopside is an important pyroxene group mineral in ultramafic rocks. However, the CPO of diopside and its deformation mechanism in serpentinites are poorly understood. In this chapter, diopside and antigorite CPOs in foliated serpentinites from Monte San Petrone in Alpine Corsica (France) were analyzed using the SEM-EBSD technique. The antigorite CPOs showed strong maxima of the [001] axes subnormal to the foliation with a weak girdle subnormal to the lineation. The diopside CPOs showed a strong alignment of (100) poles normal to the foliation and a weak girdle of (010) poles and [001] axes within the foliation, which have been rarely reported. Orientation analysis of diopside porphyroclasts and adjacent antigorite grains indicates that the formation of antigorite CPO was initially affected by topotactic growth after diopside porphyroclasts, showing the parallelism between

diopside (100) poles and antigorite [001] axes. The (001) basal glide of antigorite would then lead to the grain rotation of diopside so that (100) planes of diopside are parallel to the foliation. High angles of grain reference orientation deviation (GROD) data of diopside porphyroclasts indicate that diopside was deformed by dislocation creep. Different chemical compositions between diopside porphyroclasts and diopside neoblasts suggest that the CPO formation of diopside and antigorite was influenced by dissolution-precipitation creep. Seismic anisotropies calculated using the CPOs showed that antigorite CPO could cause a strong trench-parallel seismic anisotropy in forearc mantle in subduction zones, and that strong CPO of diopside in serpentinites would significantly decrease the delay time of S-wave in subduction zones.

**Keywords:** antigorite, diopside, CPO, creep, topotactic growth, subduction zones.

## 4.1. Introduction

Seismic anisotropy observed in worldwide subduction zones has been known to be influenced by CPOs of composite minerals, cracks, mantle flow, etc. (Healy et al., 2009; Long, 2013; Zhao et al., 2016). Particularly, the CPO of antigorite has been highlighted as an important factor for high seismic anisotropy observed in forearc mantle and continental shear zones, because of its high single-crystal elastic anisotropy and strong CPOs developed in intensely foliated rocks originated from subduction zones (Bezacier et al., 2010a; Brownlee et al., 2013; Jung, 2011, 2017; Katayama et al., 2009; Liu et al., 2020b). The formation of antigorite CPO has been attributed to plastic strain by dislocation creep (Amiguet et al., 2014a; Auzende et al., 2015; Katayama et al., 2009), fluid-assisted anisotropic growth (Mizukami et al., 2014; Nozaka, 2005) and topotactic growth after parent olivine (Horn et al., 2020; Morales et al., 2018; Nagaya et al., 2014; Padrón-Navarta et al., 2015; Soda and Wenk, 2014).

Diopside is one of the most abundant mafic minerals present in lithosphere. In antigorite serpentinites, the presence of diopside up to 11 vol.% has been reported in large amount of natural data (Auzende et al., 2006; Dlingan, 1979; Li et al., 2004; Liu et al., 2020a; Menzel et al., 2019; Nishiyama et al., 2017; Oyanagi et al., 2018; Padrón-Navarta et al., 2012; Zhou et al., 2022). It was also reported that diopside can comprise 10 – 15 vol.% of convecting mantle (Bystricky and Mackwell, 2001). Natural and experimental studies have found that diopside can be serpentitized by Ca release during fluid-assisted metamorphism of (ultra)mafic rocks (Velde, 1988; Zhou et al., 2022). As diopsidic clinopyroxene is one of the major mineral phases in

mantle rocks, the CPO study of diopside in antigorite serpentinites would be helpful to understand the seismic anisotropy observed in subduction zones.

Several researches have reported diopside CPOs in naturally foliated peridotites, and there have been two conventional types of diopside CPO in deformed rocks: (1) [001] axes aligned parallel to the lineation and a maxima of (010) poles aligned normal to the foliation (Jung et al., 2014; Le Roux, 2008; Lee and Jung, 2021; Park et al., 2020), and (2) [001] axes aligned parallel to the lineation and a maxima of [100] axes aligned normal to the foliation (Liu et al., 2020a; Skemer et al., 2006). An experimental study using diopside single crystal explained those conventional types of diopside CPO by considering diopside [001] dislocation glide in mantle pressure and mantle temperature conditions (Amiguet et al., 2009; Ingrin et al., 1992). However, the explanation for the alignment of (100) planes and (010) planes of diopside has been still controversial.

This chapter presents a new deformation mechanism for a girdle type antigorite CPO in association with diopside CPOs in foliated serpentinite samples from Monte San Petrone area in Corsica (France), using EBSD analysis. These data provided a detailed account for the deformation mechanism of antigorite and diopside during syn-kinematic serpentinization. CPO-induced seismic anisotropies of antigorite and diopside were also analyzed in order to understand the effect of diopside CPO in the seismic properties of antigorite serpentinites in subduction zones.

## 4.2. Geological setting and sample description

The serpentinite samples were collected in the Monte San Petrone area which is located in Alpine Corsica (the northeastern part of Corsica), France (**Fig. 4.1**). The Alpine Corsica underwent high-pressure/low-temperature (eclogite facies) metamorphism during the Alpine orogeny, and the Monte San Petrone unit (called MSP unit) has been defined by a basal body of serpentinitized basement of Alpine Corsica (Brovarone et al., 2011; Brovarone et al., 2013). The MSP serpentinites comprise highly strained mylonites, and the rock samples were collected near a fault zone in the mylonitic serpentinite body. The serpentinite fault has been attributed to the formation of ocean-continent transition zone during Alpine orogeny (Brovarone et al., 2011). The serpentinites in Alps have been studied to be strongly sheared during Alpine metamorphism and dominated by high-pressure antigorite serpentinite (Auzende et al., 2006). Peak metamorphic condition of the MSP area was well constrained as  $P = 2.2 - 2.5$  GPa and  $T = 490 - 550$  °C estimated from the ophiolites (metabasalts and metasediments) and continental rocks overlying the MSP serpentinitized basement (Brovarone et al., 2011).

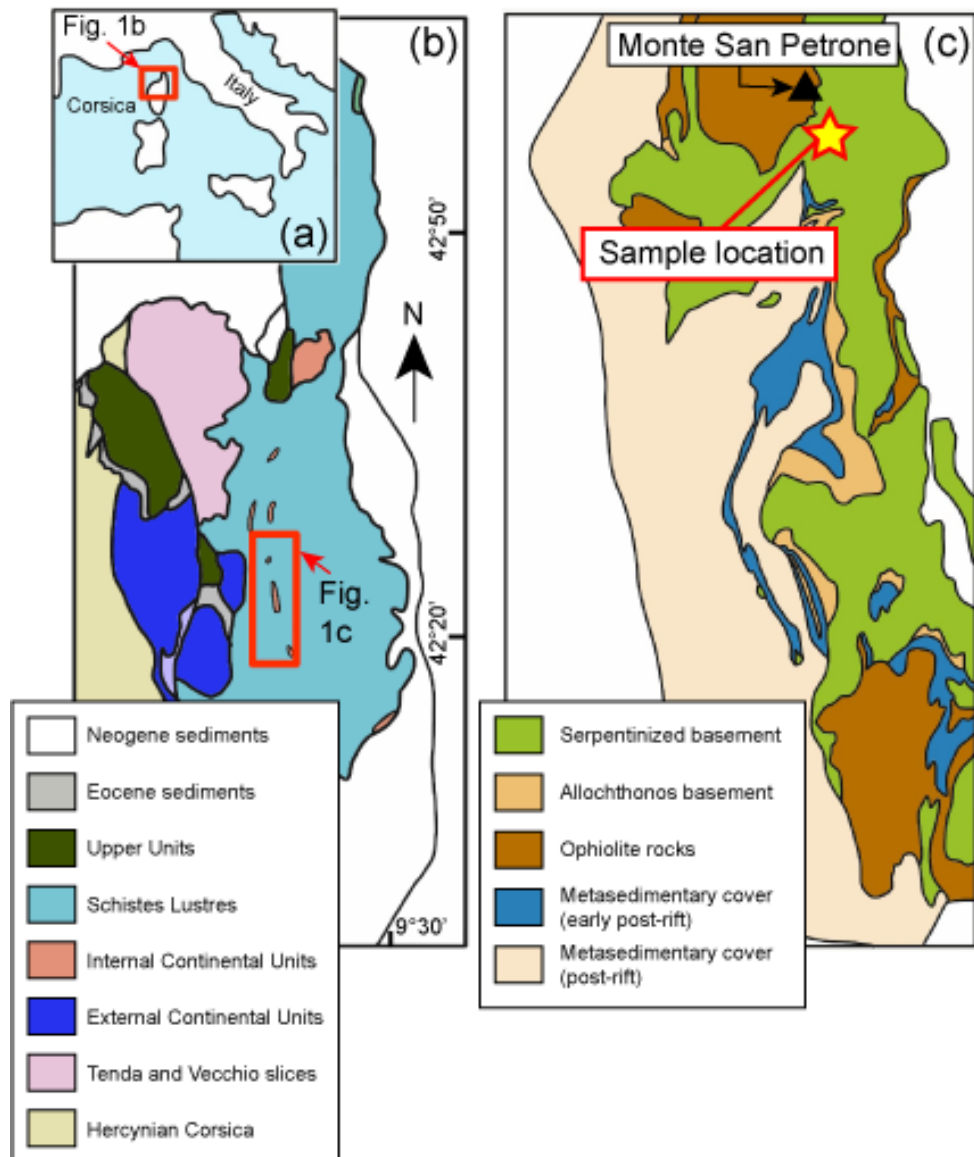
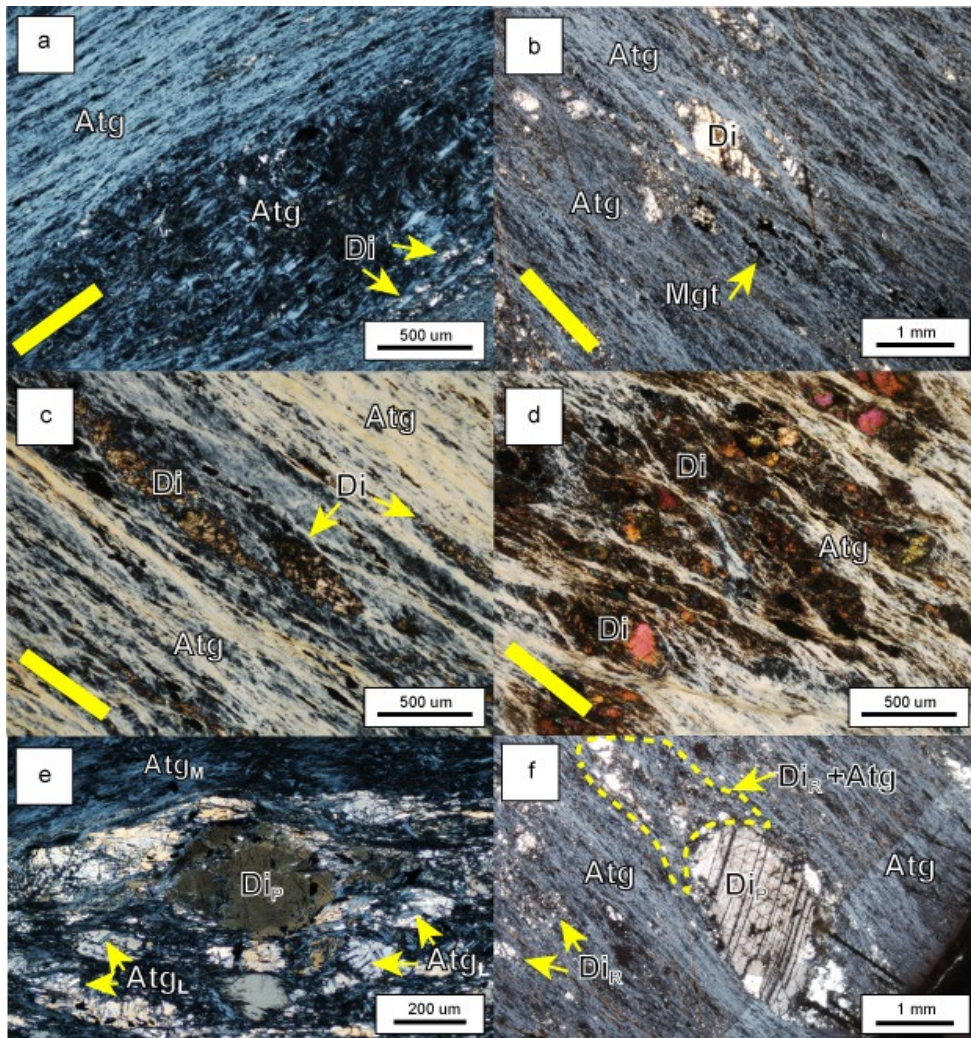


**Figure 4.1.** Maps showing the sample location of diopside serpentinites (modified after Brovarone et al., 2011). **(a)** Location of northern Corsica. **(b)** Simplified geological map of northern Corsica, showing the location of Monte San Petrone area. **(c)** Sample location of diopside serpentinites, collected from the serpentinized basement of Monte San Petrone area.



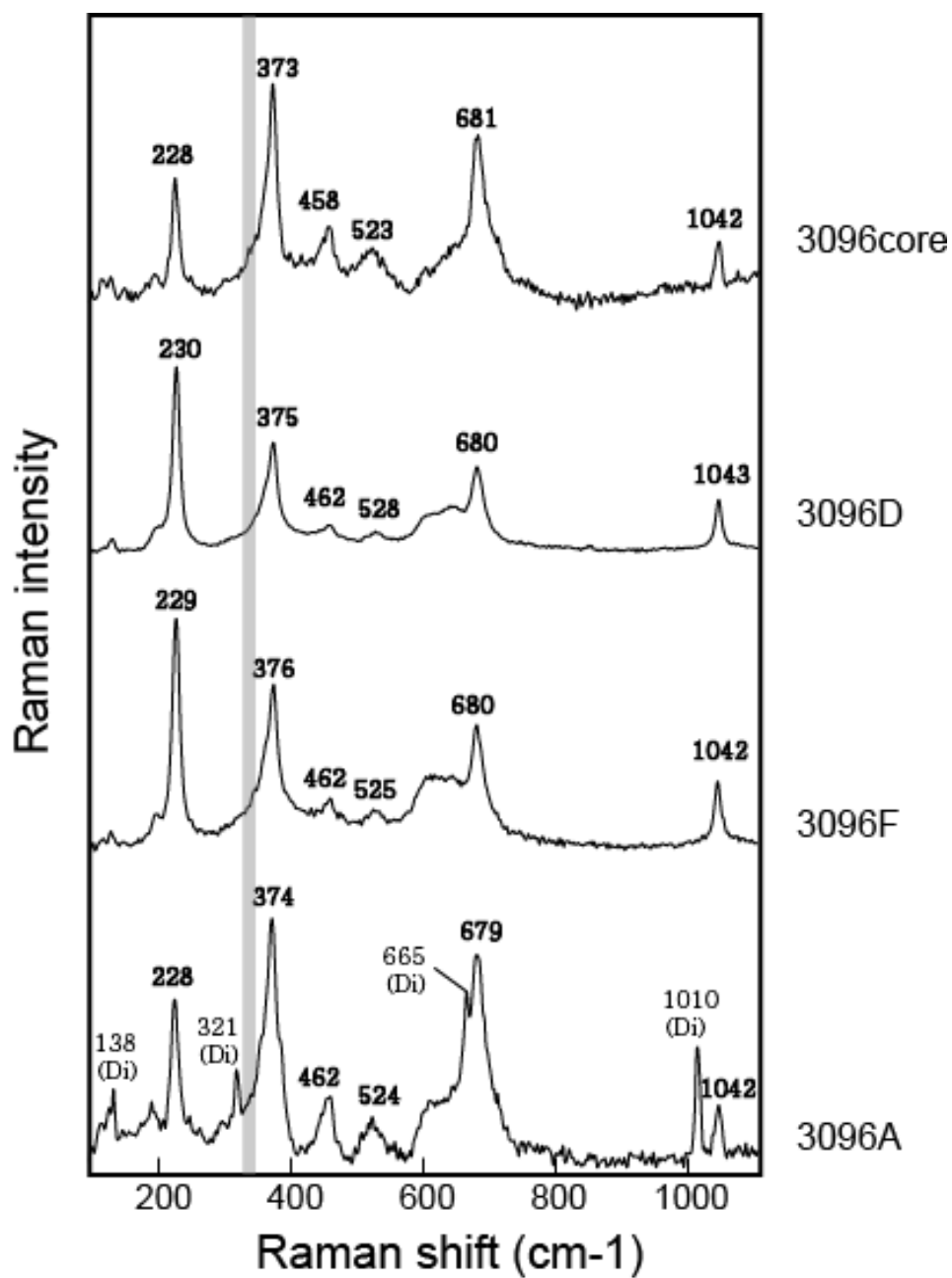
Four serpentinite samples were collected from a fault in the MSP serpentinite basement. One sample was collected near the fault core (3096core), and other three samples (3096D, 3096F and 3096A) were collected in order of distance from the fault core (3096A was the sample farthest from the fault), with each distance of 20 – 30 cm. Microphotographs of the samples were shown in **Figure 4.2**. The rock samples mainly contained 70 – 90 vol% of serpentine, 10 – 30 vol% of clinopyroxene (**Table 4.1**). Raman spectrum analysis (**Fig. 4.3**) showed that serpentine minerals are antigorite with no lizardite and chrysotile in the serpentinite samples. It indicated that the serpentinization of the MSP area occurred at the temperatures of  $T > 300\text{ }^{\circ}\text{C}$ . Clinopyroxenes in the samples were identified as diopside by electron probe micro analysis (EPMA) and Raman spectrum analysis (**Table 4.2 and Fig. 4.3**). Minor amount ( $< 1\text{ vol.}\%$ ) of chlorite, apatite, and opaque minerals (magnetite, ilmenite) were observed in all samples. Minor talc ( $< 1\text{ vol.}\%$ ) was observed only in sample 3096A. No olivine, orthopyroxene, and brucite were observed.

The diopside aggregates in samples were characterized by a shape of strongly elongated patches parallel to the lineation (**Figs. 4.2b – 4.2f**). Most of the matrix comprised of fine-grained antigorite grains, which showed a moderate to strong foliation and a strong lineation. Lens of interpenetrating texture of antigorite were observed (**Fig. 4.2a**), and any replacement texture after olivine and orthopyroxene (mesh texture or bastite texture) was not observed. No diopside pseudomorph of antigorite was observed.



(Caption in the next page)

**Figure 4.2.** Microphotographs of Corsica diopside-bearing serpentinite samples. All sections of microphotographs were parallel to the lineation and perpendicular to the foliation. Yellow bar indicates the lineation which was defined by elongation of antigorite grains and relict diopsides. **(a)** Serpentine-rich matrix (sample 3096core). Less strongly foliated lens of antigorite was wrapped by intensely foliated antigorite grains. The dark colored lens showed interpenetrating texture of antigorites. **(b)** Porphyroclastic diopsides and foliated diopside aggregates surrounded by fine-grained antigorites (sample 3096D). Both diopside aggregates and antigorite grains were strongly foliated parallel to the lineation. Opaque minerals such as magnetite and ilmenite were observed. **(c, d)** Diopside porphyroclasts and matrix antigorites in **(c)** sample 3096F and **(d)** sample 3096A, which were also strongly elongated parallel to the lineation. **(e, f)** Magnified view to show representative features of porphyroclastic clinopyroxene ( $Di_P$ ) and recrystallized diopside ( $Di_R$ ) in the MSP serpentinites **(e)**, sample 3096core and **f**, sample 3096D). Both samples were strongly sheared with surrounding antigorite-rich matrix. Long antigorite blades ( $Atg_L$ ) were invading coarse diopside grains and fine-grained antigorite grains ( $Atg_M$ ) comprised the matrix. Atg: antigorite, Di: diopside, and Mgt: magnetite.



(Caption in the next page)

**Figure 4.3.** Raman spectra of serpentine grains in the MSP diopside serpentinite samples (3096core, 3096D, 3096F and 3096A). The Raman spectra were shown as representative ones from each sample, and note that those spectra were almost identical. Strong peaks of  $373 - 376 \text{ cm}^{-1}$ ,  $680 - 681 \text{ cm}^{-1}$  and  $1042 - 1043 \text{ cm}^{-1}$  of antigorite and no peak around  $350 \text{ cm}^{-1}$  of lizardite/chrysotile (gray colored range) allowed the identification of antigorite in the samples. Several Raman spectra of antigorite included peaks of adjacent diopside grains (Di).

**Table 4.1.** Summary of sample description (mineral volume percentage and average grain size), large-area CPO type, and CPO strength (M-index) of antigorite and diopside in MSP serpentinite samples.

	Mineral volume percentage		Average grain size	
	Atg (vol%)	Di (vol%)	Atg ( $\mu\text{m}$ )	Di ( $\mu\text{m}$ )
3096core	84	16	12.3	43.7
3096D	77	23	13.0	42.6
3096F	73	27	14.6	27.3
3096A	69	31	15.3	16.9
Average	76	24	13.8	32.6

	CPO type		M-index	
	Atg	Di	Atg	Di
3096core	(001) L S	(100) L S	0.05	0.03
3096D	(001) L S	(100) L S	0.04	0.07
3096F	(001) L S	(100) L S	0.07	0.05
3096A	(001) L S	(100) L S	0.05	0.06
Average			0.05	0.05

Atg: antigorite, Di: diopside.

**Table 4.2.** Chemical composition of bulk rock, diopside and antigorite in four serpentinite samples from Monte San Petrone area. Bulk rock composition (BR) was determined by averaging the chemical compositions of diopside (rim) and antigorite (Atg) using the mineral modal percentages (**Table 4.1**) and small chlorite composition (5 vol.%) in CaO-FeO-MgO-Al<sub>2</sub>O<sub>3</sub>-SiO<sub>2</sub> system (with assumption of water saturated condition).

Sample	3096core				3096D				3096F				3096A							
Minerals	Atg	Di <sub>R</sub>	Cpx <sub>P</sub>		BR	Atg	Di <sub>R</sub>	Cpx <sub>P</sub>		BR	Atg	Di <sub>R</sub>	Cpx <sub>P</sub>		BR	Atg	Di <sub>R</sub>	Cpx <sub>P</sub>		BR
wt. %			core	rim				core	rim				core	rim				core	rim	
SiO <sub>2</sub>	41.4	55.4	50.4	50.8	48.6	41.0	55.0	51.2	54.5	49.1	43.4	55.1	50.5	51.0	49.7	40.9	54.2	51.3	51.8	49.3
TiO <sub>2</sub>	b.d.	b.d.	0.9	1.1		0.0	0.0	0.9	0.6		b.d.	0.2	0.9	0.7		0.0	0.0	0.6	0.6	
Al <sub>2</sub> O <sub>3</sub>	3.3	0.0	5.4	5.2	4.1	3.1	0.6	4.6	3.0	3.8	3.2	0.9	5.3	4.5	3.9	2.8	0.1	5.2	4.6	3.5
Cr <sub>2</sub> O <sub>3</sub>	0.3	0.0	1.1	1.2		0.6	0.3	0.9	0.6		0.5	b.d.	1.1	1.0		0.3	0.1	1.1	1.1	
FeO *	5.7	1.3	3.0	2.8	5.8	5.6	2.0	3.0	2.5	5.5	5.6	2.9	3.1	3.1	5.4	5.8	1.4	2.9	2.9	5.2
MnO	0.1	0.1	0.1	0.0		0.1	0.1	0.1	0.1		0.1	0.2	0.0	0.1		0.1	0.1	0.1	0.1	
MgO	35.8	17.8	15.1	15.2	37.0	35.8	17.1	16.0	16.5	35.4	37.3	16.0	14.7	15.9	34.0	36.3	18.5	15.8	15.8	33.8
CaO	0.0	26.2	22.9	22.9	4.5	0.1	24.5	22.2	23.8	6.2	0.1	24.4	23.2	22.4	7.1	0.0	25.3	22.3	22.8	8.2
Na <sub>2</sub> O	0.0	0.1	0.7	0.7		0.0	0.2	0.6	0.4		0.0	0.2	0.6	0.5		0.0	0.1	0.7	0.6	
K <sub>2</sub> O	b.d.	0.0	b.d.	b.d.		0.0	0.0	0.0	b.d.		0.0	0.0	b.d.	b.d.		0.0	0.0	b.d.	b.d.	

Total	86.5	100.9	99.6	99.8	86.3	99.8	99.4	101.9	90.3	99.8	99.3	99.2	86.2	99.8	99.8	100.2
#Mg	0.92	0.96	0.90	0.91	0.92	0.94	0.90	0.92	0.92	0.91	0.89	0.90	0.92	0.96	0.91	0.91
Al/8 apfu	0.38				0.36				0.36				0.32			

\* Total Fe as FeO.

Atg; antigorite, Di<sub>R</sub>; recrystallized small-sized diopside, Cpx<sub>P</sub>; porphyroclastic clinopyroxene, b.d.; below detection limit.



## 4.3. Method

### 4.3.1. Analysis of chemical composition of minerals

Chemical compositions of minerals in samples were measured by Field-Emission electron probe microanalyzer at National Center for Inter-university Research Facilities (Seoul National University). Point analyses were carried out using a 15 kV accelerating voltage, a 20 nA beam current with a 3  $\mu\text{m}$  spot size. Representative analyses of antigorite and diopside from point analysis are presented in **Table 4.2**.

### 4.3.2. P-T pseudosection of sample

P-T pseudosection for the serpentinite (bulk-rock composition of sample 3096core, **Table 4.2**) was illustrated by Perple\_X 6.9.1 software and the recent version of the Holland and Powell (2011) thermodynamic dataset. Solid solution models of antigorite (Padrón-Navarta et al., 2013), clinopyroxene (Holland and Powell, 1996), olivine (Holland and Powell, 1998), orthopyroxene (Holland and Powell, 1996), garnet (Holland and Powell, 1998) and chlorite (White et al., 2014) were used for this work. The normalized modal composition of  $\text{SiO}_2 = 48.6$ ,  $\text{Al}_2\text{O}_3 = 4.1$ ,  $\text{FeO} = 5.8$ ,  $\text{MgO} = 37.0$ ,  $\text{CaO} = 4.5$  (wt. %) (3096core in **Table 4.2**) was used in the  $\text{CaO-FeO-MgO-Al}_2\text{O}_3\text{-SiO}_2$  (water saturated) system.

### **4.3.3. Determination of foliation, lineation, and grain sizes**

The foliation of the MSP serpentinites was determined by compositional layering of antigorite and diopside. The lineation was defined by the elongation of diopside aggregates and antigorite grains. Thin sections of samples were cut parallel to the lineation and normal to the foliation. Thin sections were mechanically polished with 1  $\mu\text{m}$  polycrystalline diamond pastes and then chemically polished using a colloidal silica suspension on a rotational polisher for more than 2 h.

Grain sizes of diopside and antigorite were obtained by averaging all diopside grains and antigorite grains measured by large-area EBSD mapping of each samples. Size of diopside grains was determined by their diameter, based on the longest distance between two vertices of the grain boundary. As the shape of antigorite grains was elongated and strongly ellipsoidal in the samples, size of antigorite grains was defined as the length of long axis of the ellipsoidal grains.

### **4.3.4. Measurement of CPO**

The CPOs of composite minerals were measured by the Oxford Instruments EBSD system (AZtec v. 3.4 software) using the field-emission SEM (FE-SEM) JEOL JSM-7100F at the School of Earth and Environmental Sciences at the Seoul National University. The SEM was operated with an accelerating voltage of 15 kV, a working distance of 20 mm and a probe current of  $\sim 5$  nA. Large-area mapping was conducted in relatively large area ( $> 1$  cm x 1 cm area) of each thin section with a

step size of 1.0 – 1.5  $\mu\text{m}$ . CPOs and misorientation data were plotted using the MTEX software (version 5.7.0) (Mainprice et al., 2011). Seismic properties of mineral aggregates were calculated using the CPO results and MSAT software (version 1.1.1) (Walker and Wookey, 2012). Elastic stiffness tensor of single-crystal mineral of antigorite (Bezacier et al., 2010a) and diopside (Sang et al., 2011) were used for the calculation of seismic anisotropies of polycrystalline minerals and bulk rocks. The number of analyzed mineral grains were obtained by considering a cut-off misorientation angle of  $10^\circ$  and a minimum number of indexed pixels of 5 per grain. To plot the CPOs, the orientation distribution functions were calculated with a half-width of  $10^\circ$ . CPO strengths were indexed by M-index (Skemer et al., 2005) and pfJ index using the MTEX software.

#### **4.3.5. Calculation of misorientations**

To describe the extent of lattice distortions, several parameters were calculated such as grain reference orientation deviation (GROD), grain orientation spread (GOS), misorientation angle distributions, and subgrain misorientation axes. GROD was calculated as a “point” misorientation angle between an EBSD orientation point within a single grain and the mean orientation of the grain which includes the EBSD point. GOS is defined as an “area” misorientation angle of an individual grain, in other words, the averaged value of all GROD angles in the individual grain. Therefore, the distribution of GROD values can show the position of intragranular fabric like subgrain boundaries and twinning, and the GOS values

can imply the average degree of intragranular strains in each deformed grain. Grain boundaries were defined by misorientation angles larger than 10 degrees.

#### **4.3.6. Calculation of seismic velocities and anisotropies**

Seismic velocities and seismic anisotropies were calculated for polycrystalline antigorite, polycrystalline diopside, and bulk rock of the four diopside- serpentinite samples using CPOs of each mineral and single-crystal elastic stiffness constant of diopside crystal (Sang and Bass, 2014) and antigorite crystal (Bezacier et al., 2010a). P-wave anisotropy (AVp), S-wave anisotropy (AVs) and fast S-wave polarization directions (Vs1 pol.) were calculated in all 3-D directions of incident seismic wave through the mineral aggregates and bulk rocks.

## 4.4. Results

### 4.4.1. Mineral chemistry

Chemical analysis showed that the clinopyroxene in samples was diopside ( $X_{Mg} = 0.91 - 0.96$ ) (**Table 4.2**). Other Ca-bearing minerals such as tremolite were not observed in the samples, which inferred the removal of Ca cations by fluid during the alteration of clinopyroxene (Menzel et al., 2019; Oyanagi et al., 2018). The porphyroclastic Cpx grains showed high Al content both in core and rim, however they also showed diopsidic compositions (**Table 4.2**). The smaller recrystallized Cpx grains had low Al contents which clearly indicate the composition of diopside (**Table 4.2**).

### 4.4.2. Pressure-temperature estimates

P-T pseudosections (CFMASH system) for the Cpx-serpentinite samples obtained by this study showed that the mineral assemblage of antigorite + diopside + chlorite + talc was stable in a P-T range of  $P > 26$  kbar and  $T < 550$  °C (**Fig. 4.4**). Observations of no olivine and orthopyroxene indicated that the MSP serpentinites were altered and deformed at the temperature conditions of  $T < 570$  °C (**Fig. 4.4**). The Al contents of antigorites in the samples indicated that the serpentinization and deformation of the Cpx-serpentinites would take place at the pressures of  $P > 2.3$  GPa (**Fig. 4.4**).

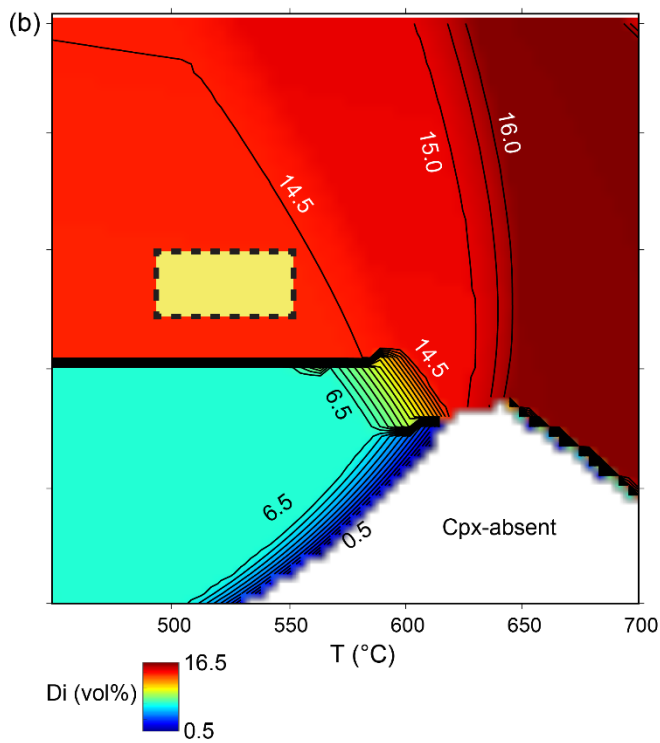
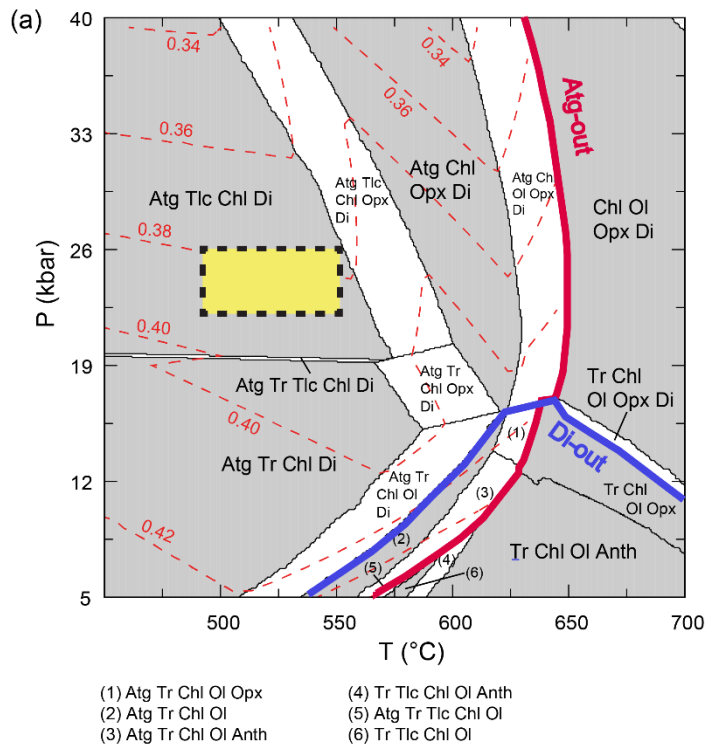


**Figure 4.4. (a)** P-T pseudosection for the serpentinite (bulk-rock composition of sample 3096core, **Table 4.2**). The normalized modal composition of  $\text{SiO}_2 = 48.6$ ,  $\text{Al}_2\text{O}_3 = 4.1$ ,  $\text{FeO} = 5.8$ ,  $\text{MgO} = 37.0$ ,  $\text{CaO} = 4.5$  (wt. %) (**Table 4.2**) was used in the  $\text{CaO-FeO-MgO-Al}_2\text{O}_3\text{-SiO}_2$  (water saturated) system. Solid solution models used for this work were described in Method. Contours of the Al-content in antigorite (Al/8 apfu.) are shown in red dashed lines, using the antigorite solid solution model (Padrón-Navarta et al., 2013). Yellow box indicates peak P-T metamorphic conditions ( $P = 22 - 26$  kbar,  $T = 490 - 550$  °C) of the Monte San Petrone area (Brovarone et al., 2011). The Al-content in the serpentinite (Al/8 a.p.f.u. = 0.380 of sample 3096core; **Table 4.2**) was in a good agreement with the P-T range of peak metamorphism recorded in Monte San Petrone. Mineral abbreviation: Atg, antigorite; Di, diopside; Ol, olivine; Opx, orthopyroxene; Tr, tremolite; Tlc, talc; Anth, anthophyllite. **(b)** Volume fraction of diopside in the same bulk composition used in (a). Yellow dashed box indicates the same peak metamorphic condition of the Monte San Petrone area in (a).

### 4.4.3. Microstructures of antigorite and diopside

Antigorite showed strong foliations and lineations in the thin section scales, and were strongly aligned parallel to the foliation. The antigorite grains associated with the Cpx porphyroclasts showed relatively large grain size and were oriented subparallel to the lineation (**Fig. 4.2e**).

Diopside in the MSP serpentinites showed porphyroclastic texture (**Figs 4.2b – 4.2f, 4.5a and 4.5b**). The porphyroclastic diopside grains were wrapped by small antigorite aggregates parallel or subparallel to the foliation (**Figs. 4.2a – 4.2d**) and those diopside porphyroclasts were partially serpentinized by coarse antigorite grains (**Figs. 4.2e and 4.2f**). Most of the diopsides were recrystallized in smaller grains, and the recrystallized diopside aggregates were present with fine-grained antigorites in the matrix (**Fig. 4.2f**).

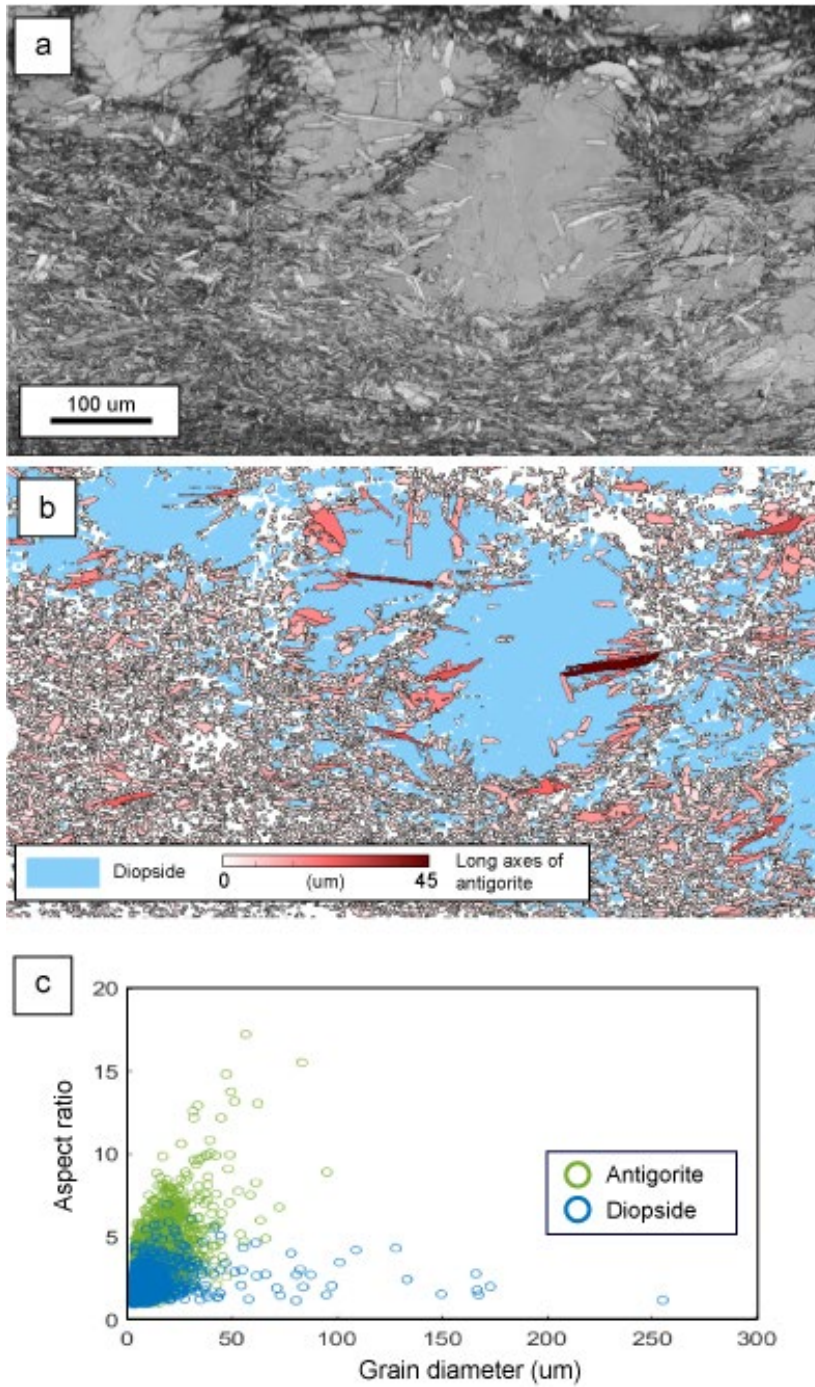
All four serpentinite samples were characterized by the presence of weakly foliated area (WFA) and strongly foliated area (SFA) (**Figs. 4.6 and 4.7**). WFAs were characterized by several large porphyroclastic diopsides, adjacent small grains of diopside, and inclusions of coarse-grained antigorite in the porphyroclasts. SFAs were characterized by diopside aggregates which were recrystallized and strongly foliated parallel/subparallel to the lineation. In both WFAs and SFAs, antigorite-diopside phase boundaries were mostly straight. Grain boundaries of both diopsides and antigorites were also straight and not concave.

In all serpentinite samples, antigorite also showed bimodal grain sizes. **Figure 4.5** showed variable lengths of antigorite long axes associated with diopside



porphyroclasts in a WFA (sample 3096A). Antigorite grains transecting diopside porphyroclasts showed a large grain size (20 – 100  $\mu\text{m}$ ) compared to those in the matrix (**Figs. 4.3b and 4.5a**). Fine-grained antigorites in the matrix showed a clear alignment of long axes parallel or subparallel to the lineation of each rock sample. Grain diameter versus aspect ratio of a sample (**Fig. 4.5c**) showed that coarse antigorite grains had a high aspect ratio, and diopside grains had much smaller aspect ratio regardless of their grain sizes (**Fig. 4.5c**).

As the sample being closer to the fault outcrop (from 3096A to 3096core), the grain size of antigorite was decreased but the grain size of diopside was increased (**Table 4.1**). Average grain sizes of antigorite in the analyzed samples were in the range of 12.3  $\mu\text{m}$  to 15.3  $\mu\text{m}$ , and average grain size of diopside (porphyroclasts + recrystallized grains) ranged from 16.9  $\mu\text{m}$  to 43.7  $\mu\text{m}$ .

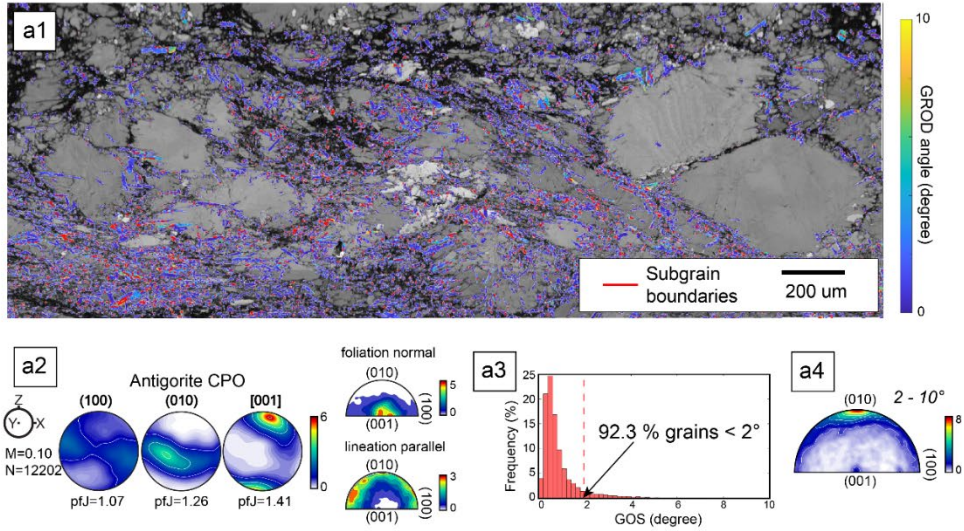


(Caption in the next page)

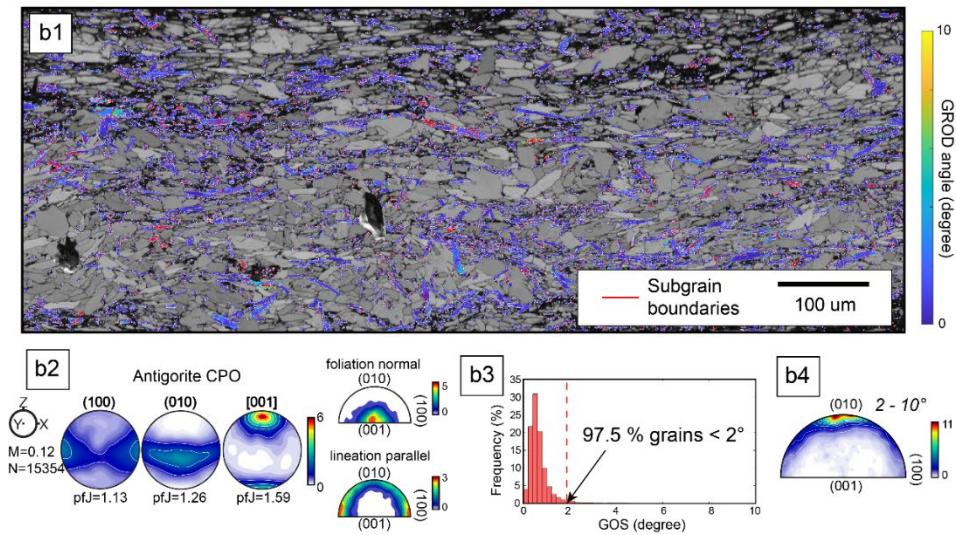
**Figure 4.5.** Representative grain shapes of diopside and antigorite in serpentinite samples (sample 3096A). **(a)** Band contrast image of an area of sample 3096A, including diopside porphyroclasts partly replaced by antigorite grains and antigorite-rich matrix. **(b)** Long axes of antigorite grains (um) associated with diopside porphyroclasts. Notice that the long axes of antigorite transecting porphyroclastic diopsides are exceptionally larger than that of antigorites in the matrix, and randomly oriented. **(c)** Relationship between aspect ratio and grain diameter of diopside and antigorite.

## Antigorite grains

(a) Weakly foliated area (WFA)



(b) Strongly foliated area (SFA)



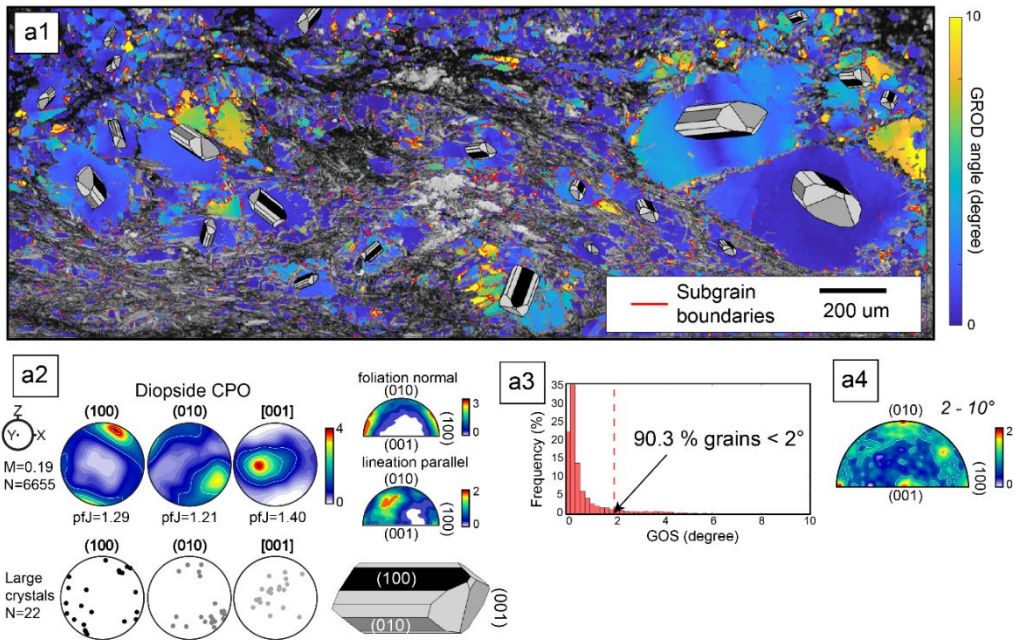
(Caption in the next page)

**Figure 4.6. (a1, b1)** GOS maps of antigorite in a **(a1)** weakly foliated area (WFA) and **(b1)** strongly foliated area (SFA) obtained from EBSD mapping (sample 3096core) overlaying the gray-scaled band contrast map. Blue-to-yellow color bars at the right side indicate GOS values (0 – 10 degrees) of each grain. Red lines in grains are subgrain boundaries, constructed by thresholds of 2 – 10 degrees of misorientation angle. Yellow arrows in **(b1)** indicate antigorite grains showing high GOS values ( $> 3^\circ$ ). **(a2, b2)** CPOs and inverse pole figures of antigorite in the **(a2)** WFA and **(b2)** SFA. CPOs were plotted for one-point-per-grain. M-index (M) for CPO strength, number of analyzed grains (N), and pfJ index (pfJ) are shown. Colorbars of CPOs and inverse pole figures indicate the strength of preferred orientations in units of multiples of random distribution (MRD). For CPOs, X-direction is parallel to the lineation and Z-direction is normal to the foliation. Inverse pole figures corresponding to the CPOs were presented in two directions: normal to the foliation and parallel to the lineation. **(a3, b3)** Histograms for GOS distribution of antigorite in the **(a3)** WFA and **(b3)** SFA. Modal percentages of low-GOS grains ( $\text{GOS} < 2^\circ$ ) were written in each histogram. **(a4, b4)** Subgrain rotation axes (subgrain boundaries with misorientation angles of 2 – 10 degrees) of antigorite in the **(a4)** WFA and **(b4)** SFA. Colorbars indicate the strength of axes concentration in MRD.

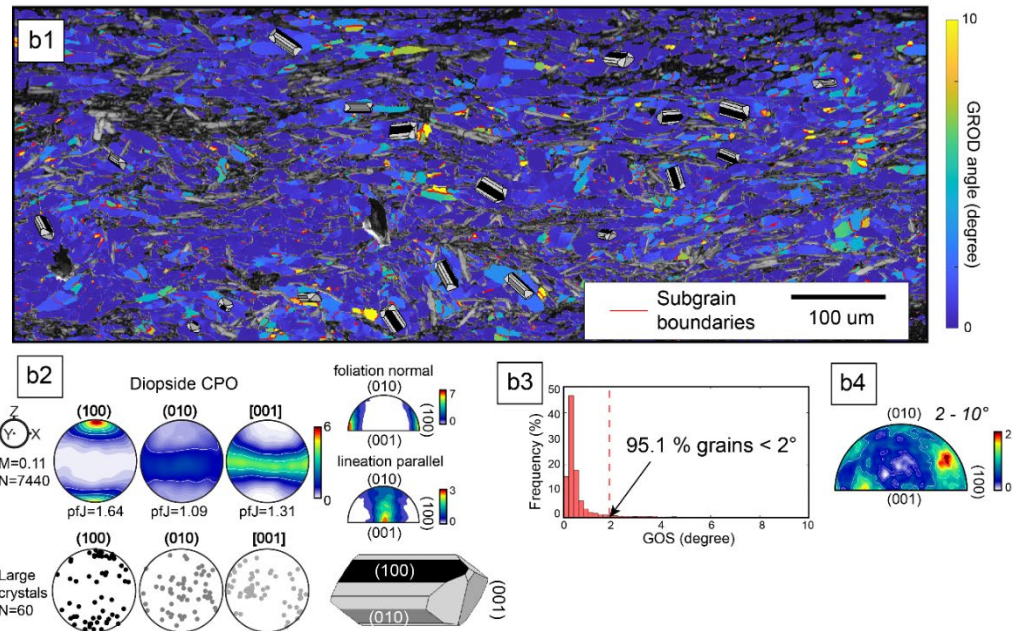


## Diopside grains

(a) Weakly foliated area (WFA)



(b) Strongly foliated area (SFA)



(Caption in the next page)

**Figure 4.7. (a1, b1)** GOS maps of diopside in a **(a1)** weakly foliated area (WFA) and **(b1)** strongly foliated area (SFA) (sample 3096core) overlaying the gray-scaled band contrast map. Each analyzed area is the same as the WFA and SFA in **Fig. 4.6**, respectively. Orientations of large diopside crystals (grain size  $> 500 \mu\text{m}^2$ ) were illustrated with colored crystallographic planes of diopside (black = (100) plane, dark gray = (010) plane, gray = (001) plane, light gray = other crystallographic planes). **(a2, b2)** CPOs and inverse pole figures of diopside in the **(a2)** WFA and **(b2)** SFA. In (a2), CPOs for large diopside crystals were also plotted. **(a3, b3)** Histograms for GOS distribution of diopside in the **(a3)** WFA and **(b3)** SFA. **(a4, b4)** Subgrain rotation axes (subgrain boundaries with misorientation angles of 2 – 10 degrees) of diopside in the **(a4)** WFA and **(b4)** SFA. Explanations for all plots, markers, colorbars and reference frame for CPOs are the same as those in **Figure 4.6**.

#### 4.4.4. CPO of antigorite and diopside

CPOs of antigorite and diopside were measured at the scale of local areas as well as large areas of samples for both WFAs and SFAs.

##### 4.4.4.1. CPO of antigorite

CPO of antigorite in WFAs of sample 3096core is shown in **Fig. 4.6a2**. The [001] axes of antigorite were strongly concentrated subnormal to the foliation. The other two poles of (100) and (010) formed a girdle distribution subparallel to the foliation, accompanied by weak maxima of (100) poles subparallel to the lineation and by weak maxima of (010) poles subnormal to the lineation. Inverse pole figures of antigorite were characterized by strong alignment of (001) poles normal to the foliation and (100) poles subparallel to the lineation.

In SFAs, antigorite grains showed the stronger CPO of (001) poles (**Fig. 4.6b2**) normal to the foliation, compared to that in WFAs. The (100) poles were moderately aligned subparallel to the foliation with maxima subparallel to the lineation. The (010) poles showed a girdle subparallel to the foliation with a moderate concentration subnormal to the lineation. Inverse pole figure of antigorite showed that (001) poles were strongly oriented normal to the foliation and (100) poles were preferentially aligned subparallel to the lineation.

At the thin section scale of all serpentinite samples, large-area CPOs of antigorite were characterized by a strong concentration of [001] axes subnormal to



the foliation with a weak girdle distribution normal to the lineation (**Fig. 4.8**). The (100) and (010) poles of antigorite showed a girdle distribution subparallel to the foliation (**Fig. 4.8**).

#### 4.4.4.2. CPO of diopside

In the WFAs, CPOs of diopside showed a concentration of (100) poles (**Fig. 4.7a2**) subnormal to the foliation. The (010) poles of diopside showed a weak alignment subparallel to the lineation and the [001] axes displayed the stronger alignment subnormal to the lineation. Inverse pole figures of diopside were characterized by (100) poles subnormal to the foliation, however the concentration was weak (max m.r.d. = 3 in **Fig. 4.7a2**). For the large diopside crystals in WFAs, all crystallographic axes seemed to be weakly oriented, but some grains were oriented forming concentrations similar to the CPO of all diopside grains in the WFA.

Diopside CPOs in the SFAs (**Fig. 4.7b2**) showed a strong alignment of (100) poles normal/subnormal to the foliation, and both (010) poles and [001] axes of diopside showed a girdle distribution parallel to the foliation. Compared to the WFAs (**Fig. 4.7a**), the (100) poles were more strongly concentrated normal to the foliation but the distribution of [001] axes was significantly dispersed within the foliation (**Fig. 4.7b**). Inverse pole figures of diopside in SFAs showed the strong concentration of (100) poles (max m.r.d. = 7 in **Fig. 4.7b2**) normal to the foliation and the alignment of (001) poles parallel to the lineation. CPOs of large diopside crystals showed the strong concentration of (100) poles subnormal to the foliation

which was similar to the CPO of all diopside grains, and the (010) poles and [001] axes were weakly oriented.

In the thin section scale of all four samples, the large-area CPOs of diopside (**Fig. 4.8**) displayed a strong alignment of (100) poles normal to the foliation, with a weak girdle subnormal to the lineation (samples 3096core and 3096F). The (010) poles and [001] axes of diopside showed a girdle distribution subparallel to the foliation in all samples, with a weak concentration of [001] axes subparallel to the lineation (sample 3096A), or subnormal to the lineation (samples 3096D) (**Fig. 4.8**). Here, M-index of diopside CPOs ranged from 0.03 to 0.05, and pfJ index of (100) poles of diopside ranged from 1.26 to 1.59.

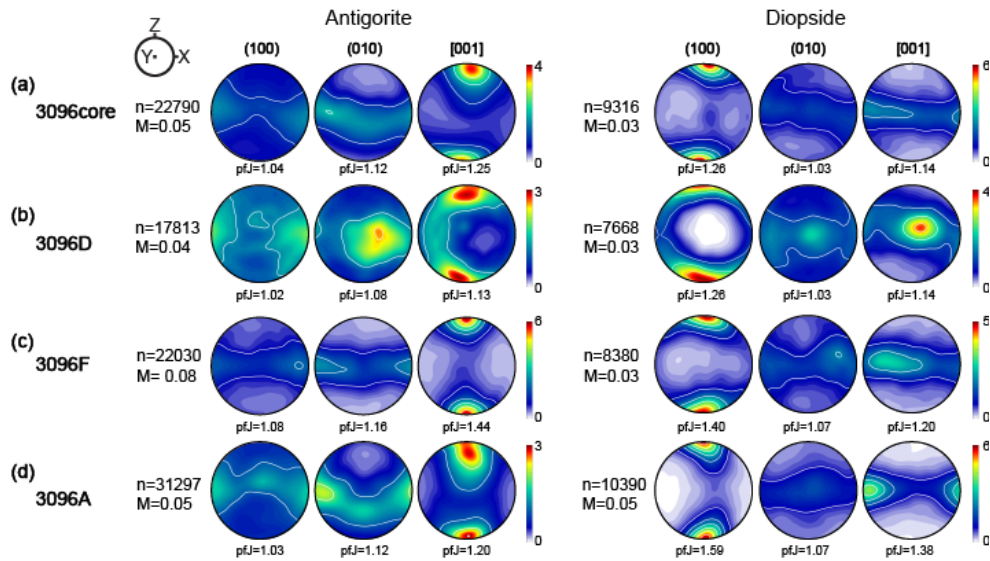


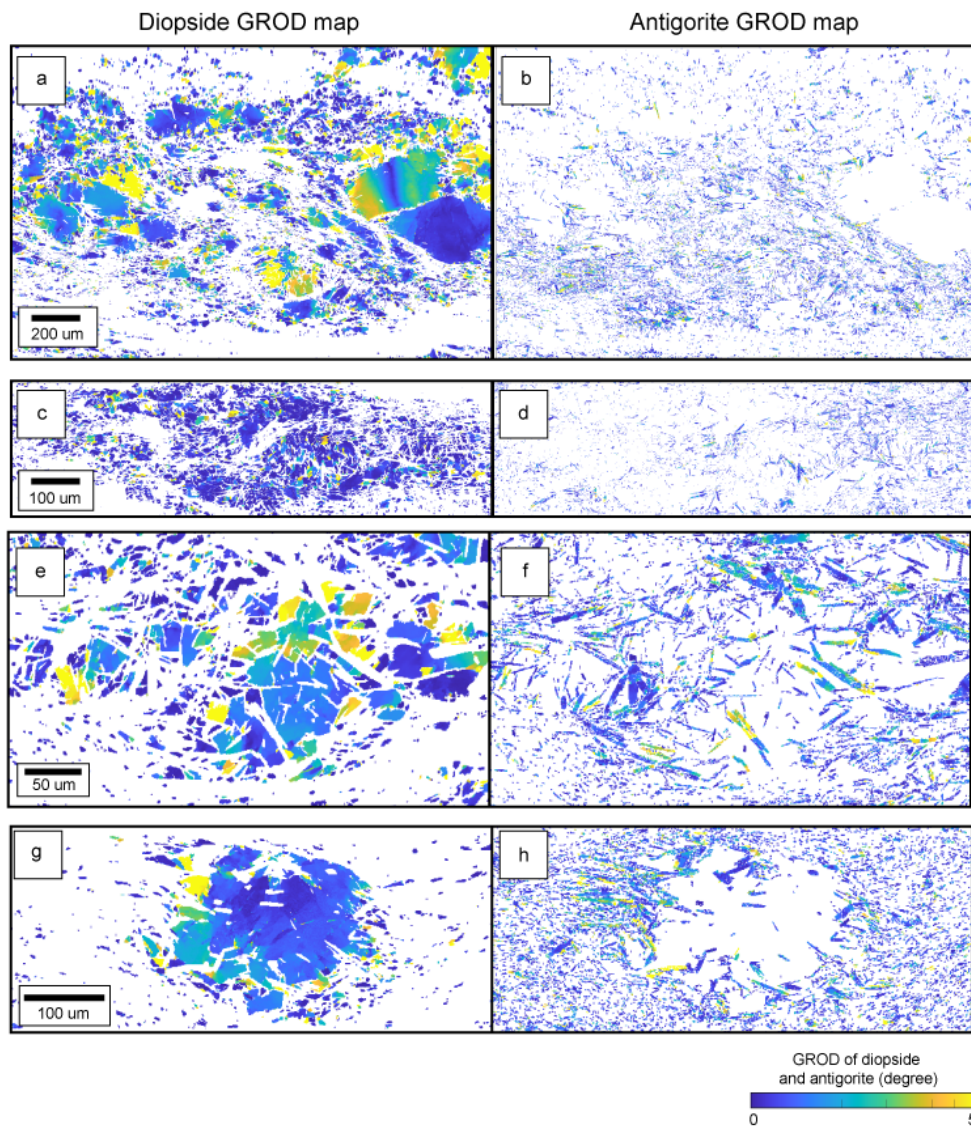
**Figure 4.8.** Large-area CPOs of antigorite and diopside at thin section scale in serpentinite samples **(a)** sample 3096core, **(b)** sample 3096D, **(c)** sample 3096F, and **(d)** sample 3096A. Pole figures are presented in the lower hemisphere using an equal area projection. Pole figure density is shown with color bars in units of MRD. Fabric strengths are also presented as M-index (M) and pfJ index (pfJ). Reference frame in the upper left indicated that the X-direction is parallel to the lineation (L), Z-direction normal to the foliation (S), and the Y-direction orthogonal to the X- and Z-direction. To the left of the pole figures, n represents the number of the analyzed grains. All CPOs were plotted by one-point-per-grain.

## 4.4.5. Misorientations of diopside and antigorite

### 4.4.5.1. Weakly foliated area

To compare the features of misorientations in the WFAs and SFAs, sample 3096core were used as a representative for the analysis. In the WFA, 90 % of diopside grains and 92 % of antigorite grains showed GOS values lower than 2 degrees (**Figs. 4.6a3 and 4.7a3**). Diopside grains can be segmented in two types in all four diopside-serpentine samples based on the GOS values. Large-sized diopside grains showed high GROD and high GOS values, and diopside aggregates with smaller grain sizes showed low GROD and low GOS values. Therefore, GOS can be used to distinguish between porphyroclastic grains (coarse-grained diopside with high GOS) and recrystallized grains (small sized grains with low GOS). Especially, the margin of porphyroclastic diopside showed the relatively high GROD values (**Fig. 4.9**), associated with long antigorite grains. Long antigorite grains associated with the diopside porphyroclast also displayed the high GROD and high GOS values, and most antigorite grains in the matrix showed the low GROD and low GOS values (**Figs. 4.9 and 4.10**).

Subgrain boundaries were also analyzed, which were defined by misorientation angles from 2 to 10 degrees (**Figs. 4.6a4 and 4.7a4**). Most of subgrain boundaries in the WFA were formed in the margins of the porphyroclastic diopsides and long antigorite grains (**Figs. 4.6 and 4.7**). Subgrain misorientation axes of diopside porphyroclasts were weakly oriented (**Fig. 4.7a4**), while those of antigorite grains displayed a strong alignment parallel to the (010) poles of antigorite (**Fig. 6a4**).



(Caption in the next page)

**Figure 4.9.** Grain reference orientation deviation (GROD) angle maps of diopside and antigorite grains in **(a, b)** sample 3096core, **(c, d)** sample 3096D, **(e, f)** sample 3096F, and **(g, h)** sample 3096A. To distinguish the highly strained area in grains, the range of plotted misorientation angle was limited to 5 degrees (see the colormap at the bottom). High GROD values and low GROD values were indexed by yellow-green color and blue color, respectively.

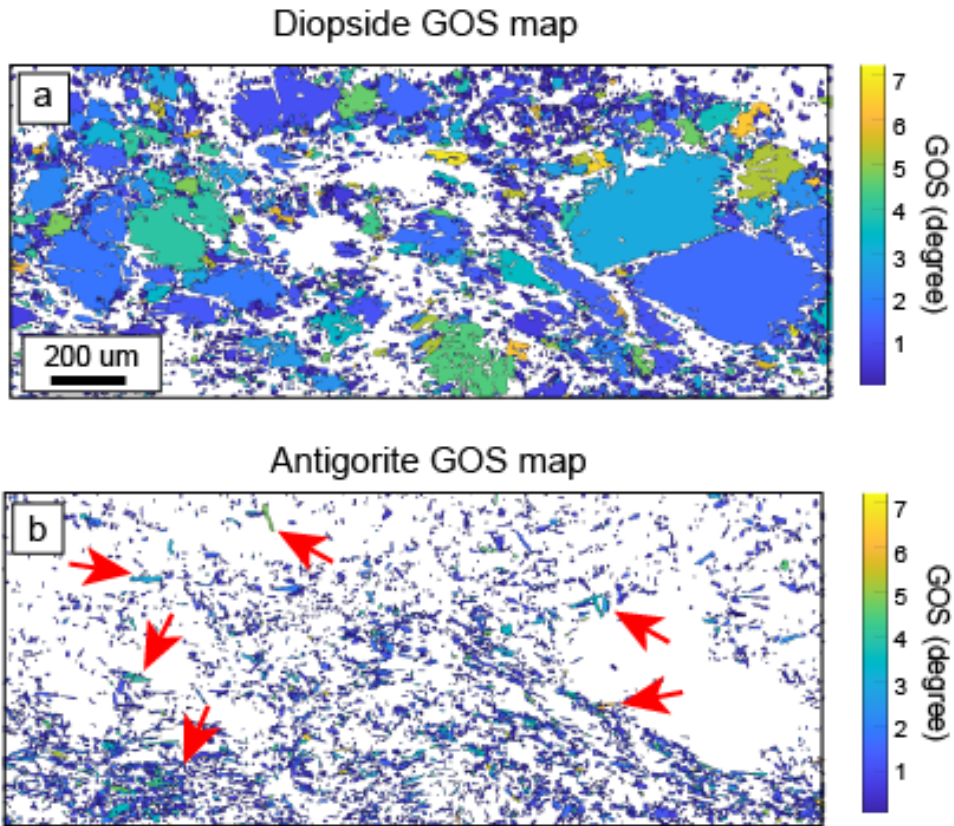


**Figure 4.10. (a, b)** Representative GOS maps of **(a)** diopside and **(b)** antigorite in the WFA (sample 3096core). The analyzed area is a magnified part of Figs. 4a and 4b. High GOS values and low GOS values were indexed by yellow-green color and blue color, respectively. Red arrows indicate large antigorite grains showing high GOS values, associated with large diopside porphyroclasts. Notice the high GOS values of porphyroclastic diopside ( $> 3^\circ$ ).

#### **4.4.5.2. Strongly foliated area**

SFAs were characterized by strongly recrystallized antigorite and diopside grains with low GROD and low GOS values (**Figs. 4.6b1 and 4.7b1**). In the SFA, 97 % of antigorite grains and 96 % of diopside grains and showed GOS values lower than 2 degrees (**Figs. 4.6b3 and 4.7b3**). However, several long antigorite grains showed high values of both GROD and GOS values (**Figs. 4.9 and 4.10**).

In most SFAs, antigorite showed misorientation axes of subgrain boundaries mainly parallel to the antigorite (010) axis (**Fig. 4.6b4**). On the other hand, recrystallized diopside grains were characterized by subgrain misorientation axes subparallel to the diopside (100) poles (**Fig. 4.7b4**).

#### **4.4.6. Seismic velocities and anisotropies of diopside and antigorite**

Seismic velocities and seismic anisotropies of diopside aggregates and antigorite aggregates are shown in **Figure 4.11 and Table 4.3**. Antigorite aggregates showed high seismic anisotropies of  $AV_p = 10.3 - 16.4\%$  and maximum  $AV_s = 7.2 - 14.3\%$ . P-wave velocities of antigorite aggregates were low at the incident wave direction subnormal to the XY plane (foliation) and gradually increased to the XY plane. Fast S-wave polarization directions of antigorite aggregates were subnormal



to the X-direction (lineation) at the incident waves normal to the foliation (at the center of the XY plane).

Diopside aggregates showed relatively low seismic anisotropies of  $AV_p = 3.3 - 4.6 \%$  and maximum  $AVs = 1.8 - 2.9 \%$ . P-wave velocities of diopside aggregates were high at the incident wave direction subparallel to the Z direction and became slower at incident directions subparallel to the Y direction. Fast S-wave polarization directions of diopside aggregates were oblique to the X-direction at the incident waves normal to the foliation (at the center of the XY plane).

Bulk-rock seismic velocities and anisotropies in the serpentinite samples were also calculated (**Fig. 4.11**), using modal compositions of antigorite and diopside of each serpentinite sample (**Table 4.1**). Patterns of bulk rock  $V_p$  and bulk rock  $AVs$  were very similar to those of antigorite aggregates. The bulk seismic anisotropies showed  $AV_p = 6.6 - 11.0 \%$  and maximum  $AVs = 4.8 - 9.5 \%$  which were significantly lower than those of antigorite aggregates. Fast S-wave polarization directions of bulk rocks were also similar to those of antigorite aggregates, but the associated  $AVs$  values of bulk rocks were lower than those of antigorite aggregates.

To estimate the seismic properties of mineral aggregates, single-crystal elastic constants of the mineral were essential. Elastic constants of antigorite from Bezacier et al. (2010a) have been ubiquitously used for the calculation of antigorite seismic properties (**Fig. 4.12**), and they were utilized for our calculation of polycrystalline seismic anisotropies (**Fig. 4.11**). Recent elastic constants of antigorite from Satta et al. (2022) were also used for the calculation of seismic properties and compared with the data obtained by using the elastic constants from Bezacier et al.

(2010a) (**Fig. 4.12**). The antigorite seismic anisotropies using the elastic constants (Satta et al., 2022) was slightly higher by  $AV_p = 1.4\%$  and  $AV_s = 1.6\%$ . The patterns of  $V_p$  and  $AV_s$  using the elastic constants of Satta et al. (2022) were very similar to those using Bezacier et al. (2010a).

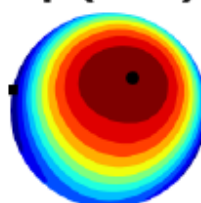
(a)

## Antigorite



**3096core**

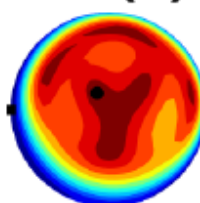
**Vp (km/s)**



6.3 7.2

AVp = 14.2 %

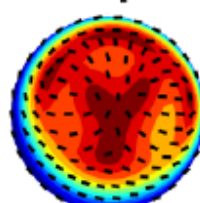
**AVs (%)**



0.2 12.1

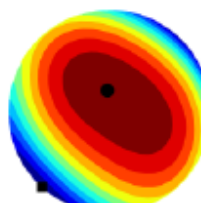
max AVs = 12.1 %

**Vs1 pol.**



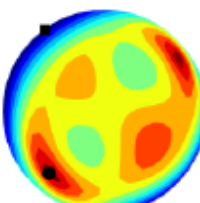
0.2 12.1

**3096D**



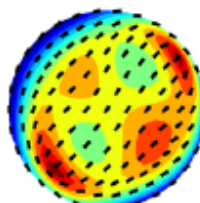
6.5 7.2

AVp = 10.3 %



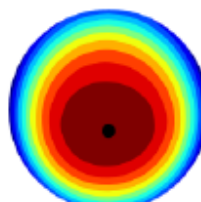
0.2 7.2

max AVs = 7.2 %



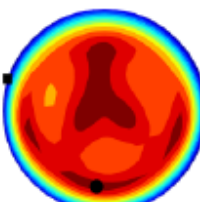
0.2 7.2

**3096F**



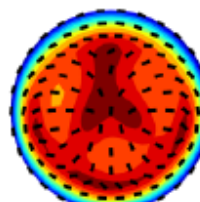
6.2 7.3

AVp = 16.4 %



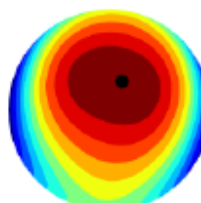
0.1 14.3

max AVs = 14.3 %



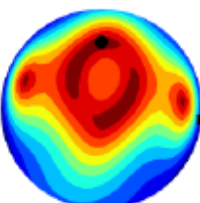
0.1 14.3

**3096A**



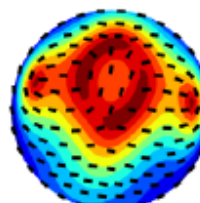
6.3 7.3

AVp = 14.6 %



0.1 10.0

max AVs = 10.0 %



0.1 10.0

(Continued)

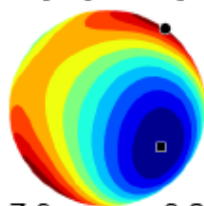
(b)

## Diopside



**3096core**

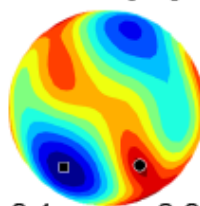
**Vp (km/s)**



7.9 8.2

AVp = 3.3 %

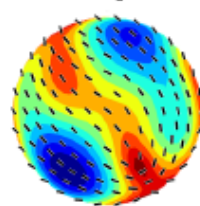
**AVs (%)**



0.1 2.0

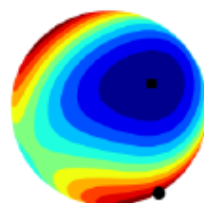
max AVs = 2.0 %

**Vs1 pol.**



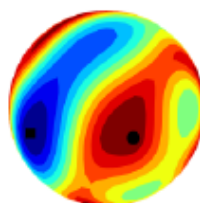
0.1 2.0

**3096D**



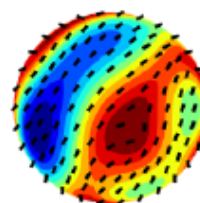
7.9 8.2

AVp = 4.5 %



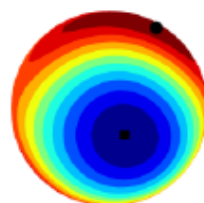
0.0 2.8

max AVs = 2.8 %



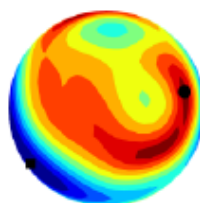
0.0 2.8

**3096F**



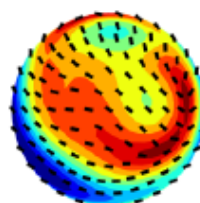
7.9 8.3

AVp = 4.6 %



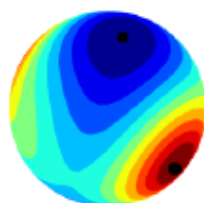
0.0 1.8

max AVs = 1.8 %



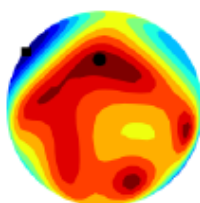
0.0 1.8

**3096A**



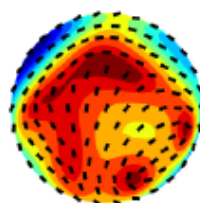
7.9 8.2

AVp = 3.8 %



0.1 2.9

max AVs = 2.9 %



0.1 2.9

(Continued)

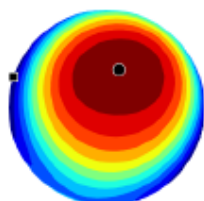
(c)

## Whole rock



**3096core**

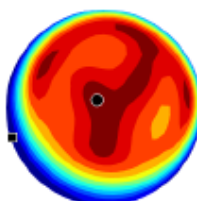
**Vp (km/s)**



6.6 7.4

AVp = 11.0 %

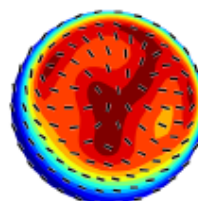
**AVs (%)**



0.1 9.5

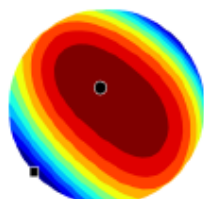
max AVs = 9.5 %

**Vs1 pol.**



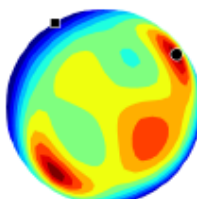
0.1 9.5

**3096D**



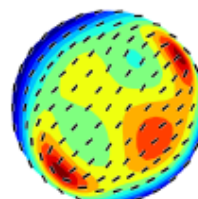
7.0 7.4

AVp = 6.6 %



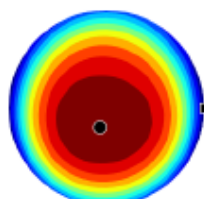
0.1 4.8

max AVs = 4.8 %



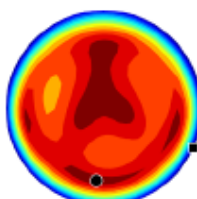
0.1 4.8

**3096F**



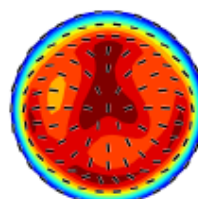
6.9 7.5

AVp = 9.2 %



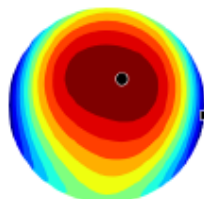
0.1 9.1

max AVs = 9.1 %



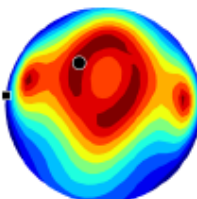
0.1 9.1

**3096A**



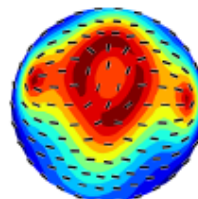
7.0 7.6

AVp = 7.8 %



0.1 6.4

max AVs = 6.4 %



0.1 6.4

(Caption in the next page)

**Figure 4.11 (a – c)** Seismic velocities and seismic anisotropies of **(a)** antigorite, **(b)** diopside and **(c)** bulk rock (whole rock) of the MSP diopside serpentinite samples. P-wave velocities ( $V_p$ ), P-wave anisotropy ( $AV_p$ ), S-wave anisotropy ( $AV_s$ ) and fast S-wave polarization directions ( $V_{s1}$  pol.) were plotted. X-direction is parallel to the lineation and Z-direction is perpendicular to the X-Y plane which is parallel to the foliation.

**Table 4.3.** Summary of seismic anisotropies of antigorite, diopside and bulk rocks of the serpentinite samples.

	P-wave anisotropy (%)			Max S-wave anisotropy (%)		
	Atg	Di	Bulk	Atg	Di	Bulk
3096core	14.2	3.3	11.0	12.1	2.0	9.5
3096D	10.3	4.5	6.6	7.2	2.8	4.8
3096F	16.4	4.6	9.2	14.3	1.8	9.1
3096A	14.6	3.8	7.8	10.0	2.9	6.4
Average	13.9	4.1	8.7	10.9	2.4	7.5

Atg; antigorite, Di; diopside, Bulk; bulk rock.

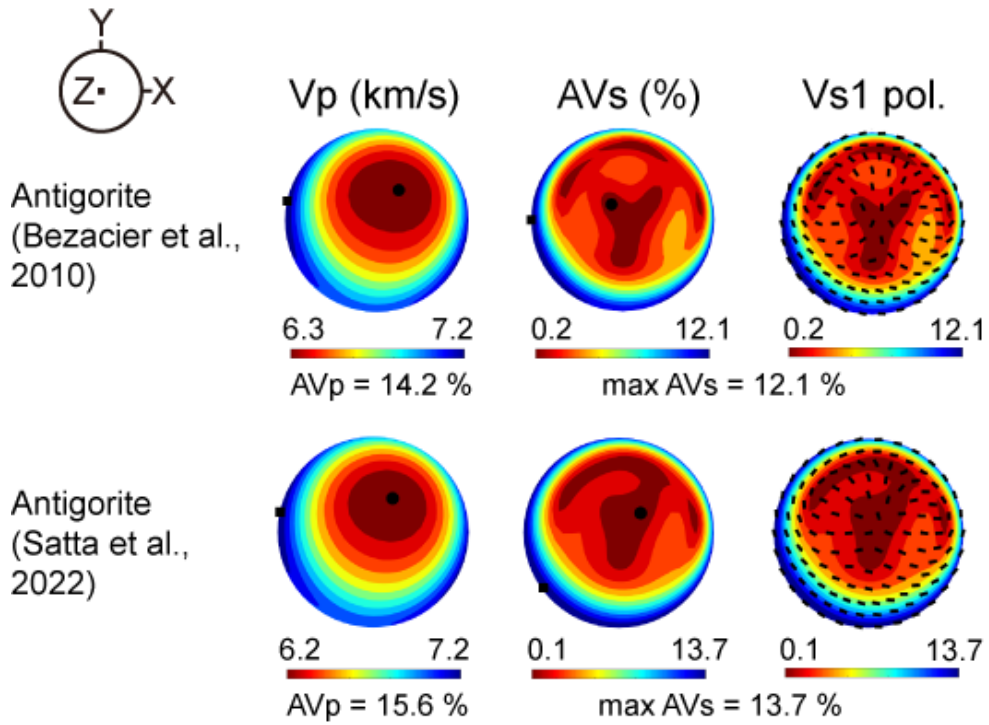


**Figure 4.12.** Comparison of seismic properties of antigorite aggregates (sample 3096core) using the antigorite single-crystal elastic constants of Bezacier et al. (2010a) and Satta et al. (2022). P-wave anisotropy (AVp), S-wave anisotropy (AVs) and fast S-wave polarization directions (Vs1 pol.) were plotted. X-direction is parallel to the lineation and Z-direction is perpendicular to the X-Y plane which is parallel to the foliation.



## 4.5. Discussion

### 4.5.1. Serpentinization and grain size of diopside

Based on the petrological observation of the MSP serpentinite samples, most of the diopside grains were preserved as a relict after serpentinization. Serpentinization of diopside in ultramafic rocks could occur by the reaction :  $3\text{CaMgSi}_2\text{O}_6$  (diopside) +  $6\text{H}^+$  (fluid) =  $\text{Mg}_3\text{Si}_2\text{O}_5(\text{OH})_4$  (serpentine) +  $3\text{Ca}^{2+}$  +  $\text{H}_2\text{O}$  +  $4\text{SiO}_2$  (fluid), which is available with decreasing temperature or decreasing silica activity (Frost and Beard, 2007). In the serpentinite samples, diopside porphyroclasts were cracked, moderately elongated, recrystallized with forming sheared aggregates and mostly replaced by antigorite grains.

Average grain sizes of antigorite and diopside in the samples showed a variation from the fault-remote sample (sample 3096A) to the fault-core sample (sample 3096core). The grain size of antigorite was decreased from sample 3096A to sample 3096core, however the grain size of diopside was increased from sample 3096A to sample 3096core (**Table 4.1**). Because a fault core is commonly characterized by a decreasing of grain size of minerals by localized deformation, those results seemed to be an odd trend. The increase of diopside grain size toward the fault core could be caused by replacement of small diopside grains to antigorite grains during the serpentinization. Toward the sample 3096core, the modal composition of antigorite was increased but that of diopside was decreased (**Table 4.1**). It implies that the serpentinization proceeded most actively in the fault core and might have erased the fine-grained recrystallized diopside first.

The serpentinization might have been occurred during deformation (“synkinematic”) which is supported by (1) increase of volume percentage of antigorite toward the fault, (2) strong foliation in the serpentinite body subparallel to the fault, (3) strong elongation of both diopside and antigorite grains parallel/subparallel to the foliation. Therefore, it could be evidence for the occurrence of fault-related serpentinization during the deformation which is related to the recrystallization of diopsides. The fault-related serpentinization would be activated by fluid flow along the fault core. The absence of Ca-bearing minerals as a product of the hydration of diopside can provide an evidence of fluid flow along the fault. The contribution of fluid along the fault can remove the  $\text{Ca}^{+}$  out of the regional system during the serpentinization (Oyanagi et al., 2018).

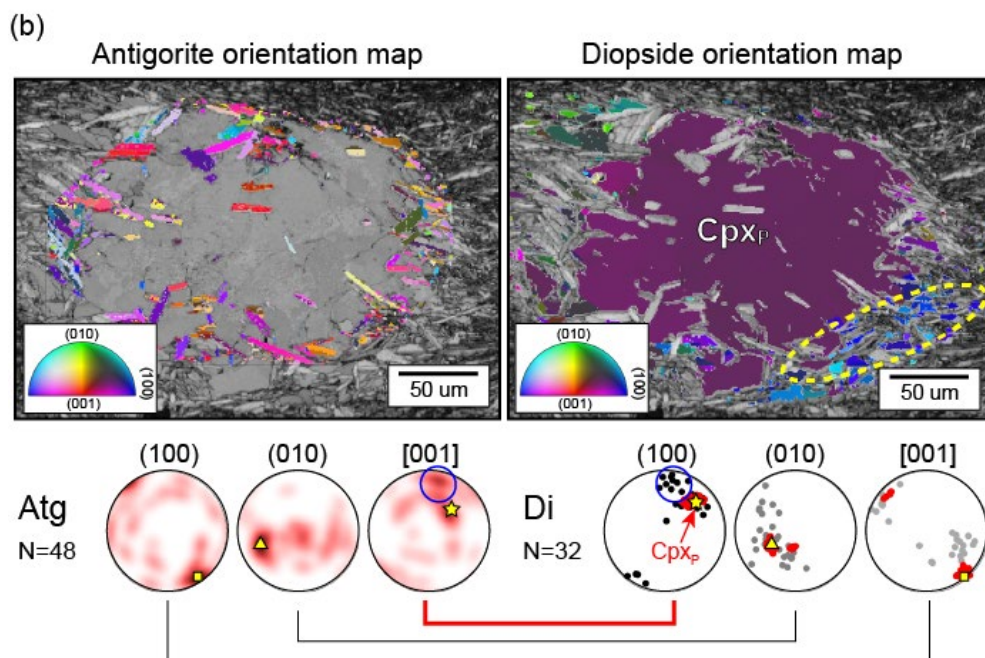
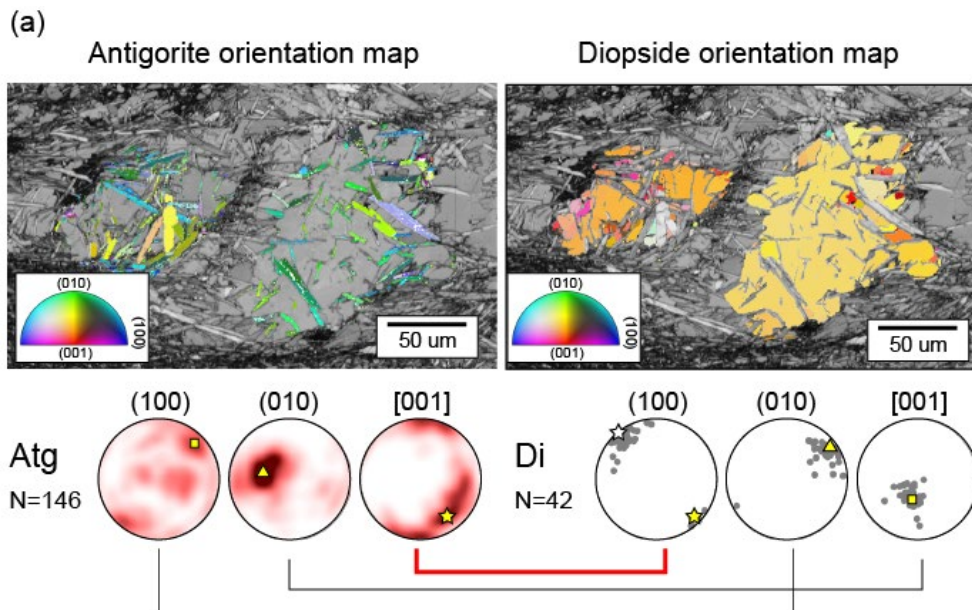
#### **4.5.2. Relationship between diopside CPO and antigorite CPO**

The diopside CPO in this study was characterized by a strong concentration of [100] axes normal to the foliation. This type of diopside CPO is apparently different from the conventional CPO of diopside found in naturally deformed rocks, showing its [010] axes aligned normal to the foliation and [001] axes clustered parallel to the lineation (Jung et al., 2014; Lee and Jung, 2021; Park et al., 2020), or a weak and random diopside CPO (Park and Jung, 2015). Skemer et al. (2006) reported diopside CPOs similar to our observations, however, their CPOs showed much stronger alignment of [001] axes parallel to the lineation and the number of

analyzed diopside grains was too limited (analyzed points  $n=44$  and  $n=81$  in two samples) (Skemer et al., 2006) to discuss about the deformation mechanism.

In the serpentinite samples, the large-area EBSD map showed that both [100] axes of diopside and [001] axes of antigorite were strongly aligned perpendicular to the foliation, both accompanied by a weak girdle normal to the lineation (**Fig. 4.8**). Antigorite CPO can be formed by preferential nucleation following the previously existed CPOs of olivine or orthopyroxene in ultramafic rocks by topotaxy (Boudier et al., 2010; Horn et al., 2020; Morales et al., 2018). Therefore, the antigorite CPO can be also influenced by the CPO of coexisting diopside during the active growth of antigorite from diopside.

**Figure 4.13** showed inverse pole figure maps and corresponding CPOs of Cpx porphyroclasts and the associated antigorite grains. It displayed that the [001] axes of antigorite were aligned parallel or subparallel to the orientation of [100] axes of diopside porphyroclasts (**Fig. 4.13**). EBSD maps in the WFA (**Figs. 4.6a and 4.7a**) also showed that antigorite [001] axes were preferentially aligned parallel to the maxima of diopside (100) poles. These observations indicated that the formation of antigorite CPO was influenced by topotactic growth  $[100]_{\text{di}} // [001]_{\text{atg}}$  from diopside.



(Caption in the next page)

**Figure 4.13. (a, b)** Orientation maps (inverse pole figure color-coded, direction of view normal to the screen) and pole figures for antigorite (Atg) and diopside (Di). Inverse pole figure (IPF) color-codes were in the inset. N indicates the number of analyzed grains. Yellow marks represent the maximum alignment of orientations. Notice that the c antigorite grains are closely related to the [001] axes of the associated diopside porphyroclast (Cpx<sub>P</sub>). Two topotactic relationships **(a)** and **(b)** were observed and they showed the common relationship of (001)Atg // (100)Di (red broken lines). Yellow dotted lines indicate the recrystallized area of diopside forming pressure-shadow texture. Blue circles in CPOs in **(b)** indicate the orientations of the recrystallized area.

### **4.5.3. Deformation mechanism of diopside and antigorite**

#### **4.5.3.1. Deformation of diopside**

Previous experimental studies have shown that diopside can be deformed by mechanical twinning (Avé Lallemant, 1978; Griggs et al., 1960; Kollé and Blacic, 1982), dislocation creep (Bystricky and Mackwell, 2001; Ingrin et al., 1992) and/or diffusion creep (Bystricky and Mackwell, 2001), depending on temperature conditions and secondarily on its grain size. However, experiments on diopside have been conducted at high temperature conditions up to 1150 °C, which is not consistent with relatively low-temperature environment of the serpentinization of diopside in this study.

#### **4.5.3.2. Deformation of diopside in the WFA**

In the WFAs, diopside showed high GROD values and a lot of subgrain boundaries in the grain margin of porphyroclasts (**Figs. 4.5 and 4.8**). Those features are clear indicators for the predominance of dislocation creep in porphyroclastic diopside in the WFA. In addition, the chemical compositions of core and rim in porphyroclastic diopside were very similar in the WFAs (**Table 4.2**) and the grain boundaries between diopside and antigorite were very clean without any concave (zig-zag) boundaries. Those characteristics suggest that dislocation creep would be the most prominent deformation mechanism of diopside in the WFA.

GOS maps and GOS histograms of diopside in the WFAs showed the higher GOS values than those in the SFAs (**Figs. 4.6 and 4.7**). They indicated that diopside porphyroclasts were deformed by accumulating internal strain energy, and finally in SFA, the strain was released (decrease of GOS) with grain size reduction during recrystallization process of diopside. Particularly, the strain was initially localized at the margin of porphyroclasts inferred by its higher GROD values compared to that in the core part (**Fig. 4.8**). This margin area of porphyroclastic diopside is also the area of active serpentinization, implying that the initial deformation of diopside was closely related to the growth of antigorite. The possible relationship was also inferred by the diopside (100) poles showing weak maxima oblique to the foliation (**Fig. 4.7a**) and the same oblique direction of the maximum alignment of the antigorite [001] axes in the same area (**Fig. 4.6a**).

#### **4.5.3.3. Deformation of diopside in the SFAs**

Diopside CPO in SFAs was characterized by (100) poles strongly aligned normal to the foliation (**Fig. 4.7b**). This strong concentration was also observed in the large-area diopside CPO in thin section scale (**Fig. 4.8**). Such CPO of (100) poles of diopside is a rarely reported feature in nature. Previously, several types of diopside CPOs have been reported in naturally deformed rocks: (1) (010) poles aligned normal to the foliation and [001] axes parallel to the lineation (Jung et al., 2014; Park et al., 2020), and (2) (100) poles normal to the foliation and [001] axes parallel to the lineation (Liu et al., 2020a; Skemer et al., 2006). Our results were roughly

consistent with the second type of diopside CPO, however a strong alignment of [001] axes subparallel to the lineation was observed only in the sample 3096A (**Fig. 4.8**).

Ingrin et al. (1992) reported that the (100)[001] slip system of diopside was the easiest dislocation slip at the experimental temperature conditions of 800 – 900 °C. At the high temperature conditions, dislocation creep of diopside at the high temperatures of  $T = 800 - 900$  °C might cause the strong alignment of (100) poles perpendicular to the foliation, prior to the serpentinization ( $T < 700$  °C where antigorite is stable). It would be an evidence for the pre-Alpine extensional tectonics in the MSP area, which was also consistent with the plastic deformation of Cpx porphyroclasts observed in the Val Malenco peridotite massif (Liu et al., 2020a). The GROD patterns of porphyroclastic diopside (**Figs. 4.9a and 4.9g**) indicated the initiation of dislocation creep at the margins of porphyroclasts. Therefore, the CPO of recrystallized diopside grains would be initially formed by dominant (100)[0vw] dislocation glide at the margins of porphyroclastic diopside. However, diopside cannot coexist with antigorite in such high temperature conditions. In addition, the CPO of porphyroclastic diopsides showed a weak CPO of (100) poles (**Fig. 4.7a2**), thus the dislocation creep of diopside cannot fully explain the strong CPO of (100) poles in the diopside serpentinites.

The alignment of (100) poles of diopside was changed from “oblique to the foliation” in the WFAs to “normal to the foliation” in the SFAs (**Fig. 4.7**). In a recrystallized zone adjacent to diopside porphyroclasts, the recrystallized small diopside grains showed the orientations of (100) poles subnormal to the foliation, regardless of the orientation of its parent porphyroclastic diopside (**Fig. 4.13b**). As



the large-area diopside CPO contained the oblique diopside CPO in the WFAs and the strong CPO of (100) poles in SFAs, it would cause the girdle type CPO of diopside in thin section scale (**Fig. 4.8**). As the SFAs were dominant in all serpentinite samples, the strong (100) maxima normal to the foliation would seem to be dominant (**Fig. 4.8**).

The diopside CPO in the WFAs was strong (**Fig. 4.7a2**), however the diopside CPO in the SFAs was weaker and could be related to dynamic recrystallization. Recrystallized small diopside crystals displayed low GROD and GOS values (**Fig. 4.7**), implying the release of intracrystalline strain after dynamic recrystallization. The recrystallized diopside grains showed a much lower Al content than that of porphyroclastic diopside (**Table 4.2**), implying a possible contribution of dissolution-precipitation creep in diopside during the syn-kinematic recrystallization. The chemical change between primary clinopyroxene and metamorphic clinopyroxene has been also observed in other natural serpentinites (Li et al., 2004; Liu et al., 2020a). Such compositional change can form the strain shadow or pressure shadow texture around porphyroclasts (**Figs. 4.9g and 4.13b**), by an adjustment to new equilibrium (Liu et al., 2020a). Liu et al. (2020a) also showed the (100) clusters of diopside neoblasts subnormal to the foliation regardless of the orientation of porphyroclastic Cpx, however in that study, the CPO of diopside was described by a limited number of grains (only one case of porphyroclastic Cpx and surrounding neoblasts in one sample were analyzed) (Liu et al., 2020a).

On the other hand, grain boundary rotation and/or phase boundary sliding can be also active to form the diopside (100) alignment normal to the foliation in

SFAs, accompanied by dominant basal glide of antigorite (001) plane parallel to the foliation. If topotaxy between (001)atg and [100]di is dominant during the synkinematic serpentinization of diopside and recrystallization of diopside and antigorite, the preferential basal glide of antigorite (001) poles could influence the phase boundary sliding of recrystallized diopside with recrystallized antigorite. Regardless of coexisting olivine CPOs and topotaxy type of antigorite [001] axes with olivine crystallographic axes, previous studies commonly showed strong maxima of antigorite [001] axes normal to the foliation (Bezacier et al., 2010a; Horn et al., 2020; Morales et al., 2018). It is inferred that basal (001) glide of antigorite is mostly important to form the final CPO of antigorite, however, topotaxy of antigorite would be still effective until the end of synkinematic serpentinization. It is suggested that the parent mineral (ex. olivine or diopside) would be deformed by grain rotation or phase boundary sliding along the easiest movement of antigorite basal (001) planes, after or simultaneously with the topotactic growth of antigorite. Therefore, the topotaxy between antigorite and diopside would be also active during serpentinization and recrystallization in SFAs.

#### 4.5.3.4. Deformation of antigorite

Antigorite CPOs showed the strong alignment of their [001] axes normal to the foliation (**Fig. 4.8**). Numerous subgrain boundaries in antigorite grains (**Figs. 4.6a1 and 4.6b1**), strong concentration of misorientation axes of subgrain boundaries (**Figs. 4.6a4 and 4.6b4**), high GROD values of coarse-grained antigorites replacing diopside porphyroclasts (**Figs. 4.9f and 4.9h**) suggest that dislocation

creep is a major deformation mechanism of antigorite in the MSP diopside serpentinites. Combined with the antigorite CPO, however, dislocation activity might not be the only dominant deformation mechanism for antigorite in the MSP serpentinites. The subgrain rotation axes of antigorite were mostly parallel to the antigorite (010) poles in both WFAs and SFAs (**Figs. 4.6a4 and 4.6b4**). If dislocation activity was the most dominant deformation mechanism, the slip system of antigorite inferred by the subgrain rotation axis should be (001)[100] slip system. However, this contrasted to the CPO results displaying a girdle distribution of (100) poles (**Fig. 4.8**), implying the contribution of other deformation mechanism to form the strong antigorite CPO. The euhedral grain shape and low GOS values of antigorite (except for some coarse-grained antigorite) implied that antigorites were also deformed by nondislocation-dominated mechanism.

Despite of the easiest basal glide of (001) plane of antigorite parallel to the rock foliation, a girdle distribution of [001] axes of antigorite has been observed in some studies. Those studies have suggested that topotactic growth from coexisting oriented olivine grains can cause the [001] girdle CPO type of antigorite (Amiguet et al., 2014b; Boudier et al., 2010; Brownlee et al., 2013; Horn et al., 2020). Crystallographic relationships by topotaxy between antigorite and olivine has been already identified, and their CPOs were found to be closely related; for example, (001)Atg // [010]Ol and [010]Atg // [001]Ol (Bezacier et al., 2010a; Boudier et al., 2010; Soda and Wenk, 2014), (010)Atg // (100)Ol and [100]Atg // [001]Ol (Horn et al., 2020; Morales et al., 2018). However, any orientation relationship between antigorite and clinopyroxene in serpentinitized ultramafic rocks has been unknown.

There is a report on the topotaxy between antigorite and orthopyroxene by dehydration of serpentinites :  $(001)\text{Atg} // [100]\text{Opx}$  (Padrón-Navarta et al., 2015).

In Discussion Chapter 5.2., the possible topotaxy of antigorite after parent diopside was suggested as an important deformation mechanism of antigorite. WFAs displayed the CPO of antigorite  $[001]$  axes oblique to the foliation (**Fig. 4.6a2**), following the CPO of diopside  $[100]$  maxima (**Fig. 4.7a2**). Such parallelism was continuously observed in the SFAs (**Figs. 4.6b2 and 4.7b2**). It would be strongly affected by the topotaxy  $(001)\text{atg} // (100)\text{di}$  during the serpentinization of diopside.

The girdle CPOs of antigorite  $[001]$  axes were observed in large-area CPOs in this study (**Fig. 4.8**) and have been observed in weakly deformed serpentinites (Brownlee et al., 2013; Hirauchi et al., 2010) or olivine-rich layer in natural serpentinites, implying the participation of grain rotation in low-strain conditions or topotaxy with olivine or dissolution-precipitation creep (Hirauchi et al., 2021; Liu et al., 2020b; Tulley et al., 2022). In the MSP serpentinite samples, several antigorite lenses displayed an interpenetrating texture (**Fig. 4.2a**) implying the contribution of dissolution process. However, no chemical zoning of antigorite grains was observed. It indicated that the dissolution-precipitation creep was not a major deformation mechanism for antigorites.

Grain rotation and/or phase boundary sliding of antigorite in olivine-rich layer has been suggested as a deformation mechanism to form a girdle of  $[001]$  axes (Liu et al., 2020b). In this study, antigorite-rich matrix is volumetrically larger than the diopside-rich aggregates in thin sections and antigorite grains shared their grain boundaries with the adjacent antigorites in the antigorite-rich matrix, thus grain

boundary rotation can play an important role to form the thin-section scale CPO of antigorite. In the diopside aggregates, a lot of antigorite grains shared their grain boundaries with diopside grains. Thus, antigorite-diopside phase boundary sliding would be also important to form the antigorite CPO.

The strong alignment of antigorite [001] axes normal/subnormal to the foliation has been regarded to be formed by dominant basal glide of (001) plane of planar antigorite crystals. In the SFAs, antigorite grains showed the stronger CPO of [001] axes normal to the foliation, the smaller grain sizes, and the much lower GOS values (**Fig. 4.6**) compared to those in WFAs. Those features suggested that grain size reduction of antigorite in SFAs would relax the intragranular strain of antigorite, and enhance the basal (001) glide parallel to the foliation.

The large-area CPOs of antigorite showed a strong alignment of antigorite [001] axes subnormal to the foliation and both (100) and (010) poles aligned as a girdle subparallel to the foliation (**Figs. 4.8b and 4.8c**). Such a CPO of antigorite has been accounted by activation of both (001)[010] and (001)[100] slip system (Jung, 2011; Liu et al., 2020b; Padrón-Navarta et al., 2012). The girdle CPO of antigorite can show different intensities of (100) and (010) maxima, reflecting the relative contribution of antigorite (001)[100] and (001)[010] dislocation creep system, respectively (Padrón-Navarta et al., 2012). In this study, the pfJ index of antigorite (010) poles were higher than that of (100) poles in thin section scales of all serpentinite samples, indicating the possible stronger contribution of (001)[010] slip system than (001)[100] system. This contrasts to the subgrain boundary analysis which showed the predominance of [010]-axis-parallel rotation axes (**Fig. 4.6**),

implying the activation of the strong (001)[100] slip system. Our data indicate that antigorite in the MSP serpentinites was deformed mainly by (001)[hk0] dislocation creep, accompanied by subgrain boundary rotation.

In the antigorite-rich matrix, some antigorite lenses were observed showing interpenetrating texture (**Fig. 4.2a**). Some antigorite grains replacing diopside porphyroclasts showed an oblique alignment to the foliation, forming a “strain shadow” at the margins of the porphyroclasts (**Fig. 4.9h**). The interpenetrating fabric and strain-shadow-like structure of antigorite implied a low-strain environment and dissolution-precipitation creep (Hirauchi et al., 2021; Tulley et al., 2022). However, the coarse-grained antigorite forming the strain shadow displayed especially high GROD values (**Figs. 4.9f and 4.9h**), indicating that those antigorite grains were mainly deformed by dislocation creep with a minor contribution of dissolution-precipitation creep.

#### **4.5.3.5. Deformation history of syn-kinematic serpentinization in the MSP serpentinites**

Microtextural observations revealed that the serpentinite schists were deformed by the combination of various deformation mechanisms. The series of intracrystalline deformation in the MSP serpentinites can be summarized: (1) dislocation creep of diopside porphyroclasts at high-temperature conditions, (2) topotactic growth of antigorite adjacent to diopside with decreasing temperature, (3) dynamic recrystallization of diopside and antigorite, (4) phase boundary sliding and

grain rotation of antigorite and diopside at low temperature, accompanied by minor dissolution-precipitation.

Dislocation creep of diopside can take place at the temperature of  $T > 800\text{ }^{\circ}\text{C}$  (Amiguet et al., 2009; Ingrin et al., 1992). In the margins of diopside porphyroclasts, high GROD values and the presence of subgrain boundaries are clear indicators for the activation of dislocation creep of diopside at the high-temperature conditions.

Because no olivine and orthopyroxene were observed in the serpentinite samples, the serpentinization would have occurred at the temperature lower than  $550\text{ }^{\circ}\text{C}$  (**Fig. 4.4**). The Al-contents of antigorite indicated that the serpentinization occurred at the pressure conditions of  $\sim 26\text{ kbar}$  (**Fig. 4.4**). Such P-T conditions were similar to the peak metamorphic conditions of Mesozoic metaophiolites and metasediments ( $P = 22 - 26\text{ kbar}$  and  $T = 220 - 260\text{ }^{\circ}\text{C}$ ) overlying the MSP serpentinite basement (Brovarone et al., 2011). The dislocation-based deformation of diopsides might take place at much higher temperatures before the formation of the MSP serpentinites. During the syn-kinematic serpentinization, diopside might be recrystallized accompanied by dissolution-precipitation creep. Combination of serpentinization and dissolution-precipitation creep would be capable of strain localization in diopside serpentinites by fluid-assisted process (Liu et al., 2020a). The strain localization would be important for the occurrence of aseismic events and/or exhumation of rocks along hydrated subduction zone interface.

#### **4.5.4. Serpentinization and stability field of the samples in MSP area**

For Alpine orogen, previous studies have shown that the serpentinization of Alpine ultramafic rocks occurred during the pre-Alpine emplacement of mantle rocks into shallow crustal levels (Katzir et al., 2022), and the serpentinization of clinopyroxene (diopside) would take place in mantle wedge P-T conditions in supra-subduction zone settings (Liu et al., 2020a). Diopside-bearing serpentinites would be stable in metamorphic conditions from greenschist facies to eclogite facies in CaO-MgO-SiO<sub>2</sub> system (Evans, 1977), and previous petrological studies have shown the high-pressure stability of antigorite with diopside (Blanco-Quintero et al., 2011; Menzel et al., 2019; Padrón-Navarta et al., 2013). This is consistent with the pseudosection results of the MSP serpentinite sample (sample 3096core) where diopside + antigorite assemblage was stable at the pressures up to  $P = 40$  kbar and temperatures up to  $T = 650$  °C (**Fig. 4.4**). The Al content of antigorite in the serpentinite sample (3096core) indicates that the serpentinization and deformation would have occurred during the peak metamorphism of the MSP area, which recorded the P-T conditions of  $P = 2.2 - 2.6$  GPa and  $T = 490 - 550$  °C. For the sample 3096A, the lower Al content of antigorite and the presence of talc indicated that the syn-kinematic serpentinization would occur at much higher-pressure conditions up to 3.7 GPa. The comprehensive results suggest that the diopside + antigorite assemblage can be stable at high-P-low-T mantle wedge, which can represent the low-temperature and high-pressure subduction zones.

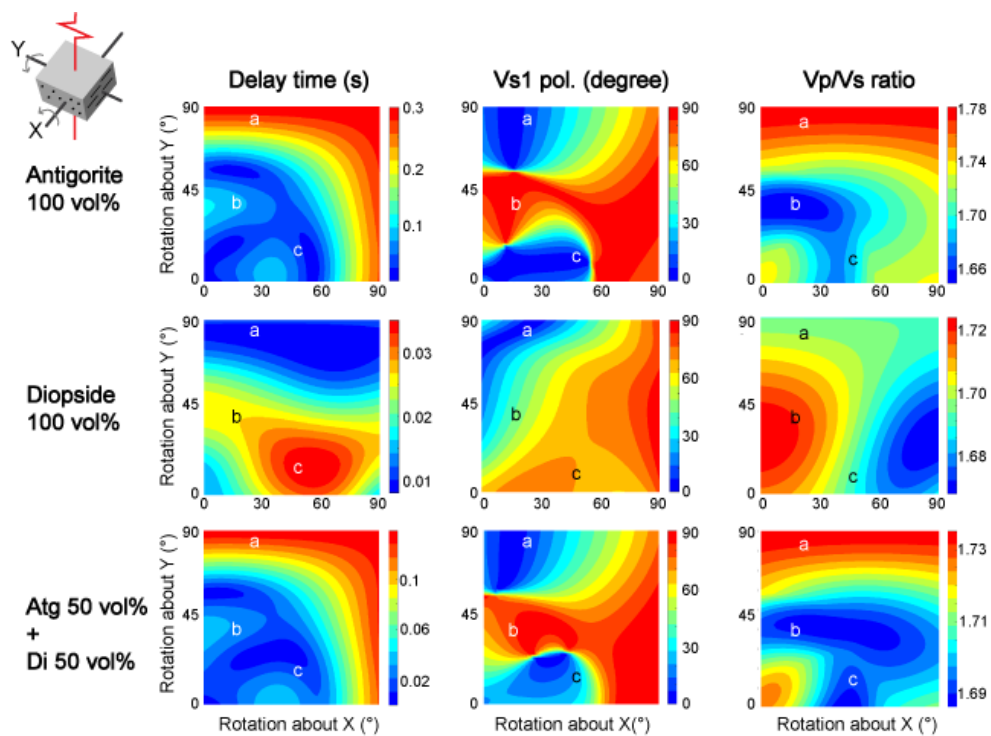


#### 4.5.5. Implications of diopside and antigorite for seismic anisotropy in subduction zones

The seismic anisotropies of polycrystalline antigorite have been reported in many previous studies, ranging  $AV_p = 5.7 - 46.3 \%$  and  $\max AV_s = 4.9 - 50.5 \%$ , which were significantly varied depending on their CPO strength (Jung, 2017). Compared to the other study areas, the diopside serpentinites from MSP showed relatively low seismic anisotropy values of antigorite ( $AV_p = 10.3 - 16.4 \%$ ,  $\max AV_s = 7.2 - 14.3 \%$ ; **Table 4.3**). However, the antigorite aggregates in this study showed much higher seismic anisotropies than those of diopside aggregates ( $AV_p = 4.1 \%$ ,  $\max AV_s = 2.4 \%$  in average), although the CPO strength of antigorite ( $M = 0.4 - 0.7$ ) is similar to that of diopside ( $M = 0.3 - 0.7$ ) (**Table 4.1**). It implied that CPO of antigorite is important for the high seismic anisotropy of serpentinites, compared to that of diopside.

For a detailed study about the effect of antigorite and diopside CPOs on seismic properties in subduction zones, the delay time, fast S-wave polarization directions, and  $V_p/V_s$  ratio of both antigorite and diopside were calculated using their CPOs with a geographical reference frame for a subduction zone (**Fig. 4.14**). When the diopside serpentinite was strongly foliated by a high-angle to the Earth surface (e.g. high-angle subduction interfaces or high-angle faults developed in subducting slab; *a* area in **Fig. 4.14**), antigorite aggregates showed a long delay time ( $dt = 0.25 - 0.3$  s) but diopside aggregates showed a very short delay time ( $dt = 0.01$  s). In the same geometry (*a* area), both antigorite and diopside showed trench-

parallel polarization direction at the dip angle of  $\theta > 50^\circ$ . When the subducting slab is moderately dipping ( $\theta = 20 - 50^\circ$ ) (*b* area in **Fig. 4.14**), antigorite aggregates showed trench-normal polarization directions but diopside aggregates showed trench-oblique polarization directions. When the slab dip angle is small  $\theta < 20^\circ$  (*c* area in **Fig. 4.14**), antigorite aggregates showed trench-parallel polarization with short delay time, and diopside aggregates showed trench-oblique polarization with long delay time which is still much shorter than the delay time of antigorite. By adding antigorite aggregates to diopside aggregates (Atg 50 vol % + Di 50 vol %) at high-angle subducting angle (*a* area), its delay time increased and Vp/Vs ratio also increased, however the fast polarization direction remained as trench-parallel. These comparisons revealed the importance of antigorite CPO for strong trench-parallel anisotropy and high Vp/Vs ratio observed in high-angle cold subduction zones (Long, 2013).



(Caption in the next page)

**Figure 4.14.** The 3-dimensional seismic properties of antigorite and diopside CPO on delay time between fast S-wave and slow S-wave (Delay time), fast S-wave polarization direction ( $V_{s1}$  pol.) and the ratio between P-wave velocity and fast S-wave velocity ( $V_p/V_s$  ratio) using representative large area CPO data (sample 3096core). In the uppermost left, the schematic rock geometry is illustrated to show how the serpentinite (X–Y plane = foliation, dots and lines = lineation) is rotated with respect to the incoming S-waves (red solid line). For simplicity, X is assumed to be parallel to the subducting direction and Y parallel to the strike of the hypothetical trench. Rotation of mineral aggregates around X and Y from 0 degree to 90 degrees was considered to display the effect of the dipping foliation (X–Y plane) in subduction zones. An anisotropic layer thickness of 10 km and a vertically incident S-wave were assumed for the calculation. All contoured plots are illustrated by a color range from blue to red. In the plots of delay time, blue color and red color indicate short delay times and long delay times, respectively. In the plots of  $V_{s1}$  pol., blue color and red color indicate trench-parallel polarization directions and trench-normal polarization directions, respectively. In the plots of  $V_p/V_s$  ratio, blue color and red color indicate low  $V_p/V_s$  ratios and high  $V_p/V_s$  ratio, respectively.

Olivine is also one of the major minerals in subduction zones with a B-type CPO in water-rich condition (Jung and Karato, 2001). To understand the combined effect of olivine, serpentine, and diopside CPOs on seismic properties in subduction zones, this study used a B-type CPO of olivine (Jung et al., 2014) and compared with the results of antigorite and diopside (**Fig. 4.15**). The results showed that the contribution of antigorite increased the delay time and  $V_p/V_s$  ratio, and caused trench-parallel polarization directions at a high-angle subduction zone (*a* area in **Figs. 4.15a and 4.15b**). Those patterns remained regardless of the contribution of diopside (Atg 40 vol% + Ol 30 vol% + Di 30 vol%) (**Fig. 4.15c**). The results suggested that antigorite is an important factor to cause strong trench-parallel anisotropy in cold subduction zones.

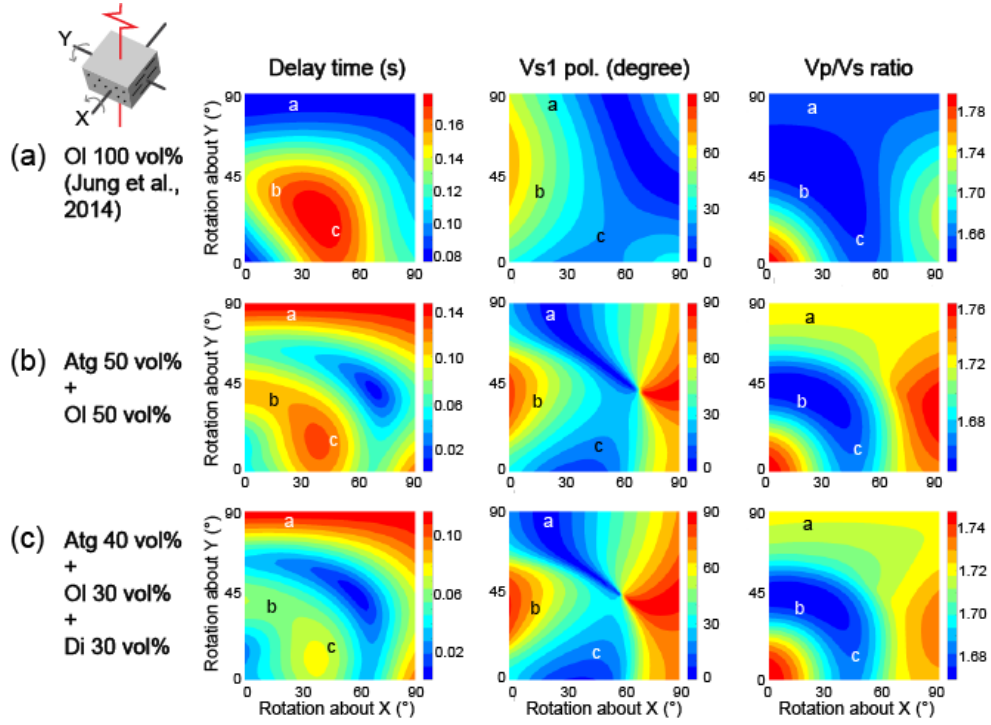


**Figure 4.15.** The 3-dimentional seismic properties of olivine, diopside and antigorite CPO on delay time, Vs1 polarization directions, and Vp/Vs ratio. Assumptions for rock mineral assemblage of **(a)** olivine 100 vol%, **(b)** antigorite 50 vol% + olivine 50 vol%, and **(c)** antigorite 40 vol% + olivine 30 vol% + diopside 30 vol% were described. CPO data of antigorite and diopside (sample 3096core in this study) and an B-type olivine CPO in sample 374 (Jung et al., 2014). The geometric reference frame and color code are the same as in **Fig. 4.14**.

## 4.6. Conclusions

In this chapter, microstructures and seismic anisotropies of antigorite and diopside in the serpentized basement of MSP area in Alpine Corsica, France, were studied. CPO results showed strong maxima of antigorite [001] axes normal to the foliation, and diopside [100] axes normal to the foliation with a weak girdle. Detailed EBSD study showed that [001] axes of antigorite were preferentially aligned parallel to the (100) poles of diopside, indicating that the CPO formation of antigorite was influenced by a topotactic growth from diopside. The EBSD study on strongly foliated areas showed that the CPO of (100) poles of diopside was influenced by phase boundary sliding and grain rotation following the antigorite (001) basal glide. The high GROD values in the margins of porphyroclastic diopside and the low GOS values of small diopside grains indicated that dislocation creep of diopside would cause dynamic recrystallization of diopside porphyroclasts starting in the margin of porphyroclasts. The analysis of subgrain rotation axis of minerals and different chemical compositions between porphyroclastic diopside and recrystallized diopside, indicate a contribution of dissolution-precipitation to the CPO formation of diopside and antigorite. The CPO-induced seismic properties of antigorite showed that syn-kinematic serpentization in mantle wedge would be important for strong trench-parallel seismic anisotropies and high  $V_p/V_s$  ratio observed in cold subduction zones. On the other hand, it was found that the strong diopside CPO in the foliated serpentinites would decrease the delay time of S-wave.

## CHAPTER 5. Summary and conclusion

Deformation microstructures of talc, chloritoid, and serpentine in naturally deformed rocks were studied to understand the effect of hydrous minerals on the seismic properties observed in subduction zones. Presented are the studies of talc CPO and its seismic anisotropy, especially P-wave anisotropy in subduction zones (Chapter 2), chloritoid CPO and its seismic properties (Chapter 3), and antigorite CPOs which were developed with diopside CPOs (Chapter 4).

In Chapter 2, the metabasaltic Grt-Cld-Tlc schist samples from Makbal complex (Kazakhstan-Kyrgyzstan) and metasomatic talc schist samples from Unst Island (Scotland) were analyzed by EBSD technique to measure the CPOs of talc and determine the effect of talc CPO on seismic anisotropy in subduction zones. The CPO of talc was characterized by strong maxima of [001] axes normal/subnormal to the foliation. The CPO-induced P-wave anisotropy of talc was very high ( $AV_p = 67 - 72 \%$ ) and the radial anisotropy of P-wave of talc was negative at the high-angle subduction geometries. It was found that the strong CPO of talc would be important for interpreting the P-wave anisotropy in subduction zones.

In Chapter 3, elastic properties of chloritoid were first calculated and the CPO of chloritoid was measured in the Grt-Cld-Tlc schist samples from Makbal complex (Kazakhstan-Kyrgyzstan). The elastic anisotropy of single-crystal chloritoid showed a high elastic anisotropy of chloritoid reflected by  $AV_p = 22 \%$  and  $\max AV_s = 47 \%$ . The CPO of chloritoid showed strong concentration of [001] axes subnormal to the foliation. The P-T stability of chloritoid was re-evaluated by



pseudosection studies, which revealed the wide stability of chloritoid up to the blueschist-facies metamorphic condition. The results of seismic anisotropies of chloritoid suggested that the CPO of chloritoid would influence the trench-parallel seismic anisotropy in high-pressure-low-temperature conditions in subduction zone interfaces, in association with glaucophane and phengite in blueschist-facies conditions.

In Chapter 4, deformation microstructures of antigorite and diopside in the serpentized basement of MSP area in Alpine Corsica (France) were studied to investigate the deformation mechanism of serpentine in diopside serpentinites. The CPO of antigorite showed strong maxima of antigorite [001] axes normal to the foliation with a weak girdle. Detailed EBSD study showed that [001] axes of antigorite were preferentially aligned parallel to the alignment of (100) poles of diopside. The CPO-induced seismic anisotropy of antigorite showed the strong trench-parallel S-wave anisotropy in high-angle subduction geometries, and the participation of diopside CPO decreased the delay time of serpentinites. The results indicate that the CPO of serpentine can be influenced by a topotaxy from the CPO of diopside in mantle rocks, and the strong trench-parallel anisotropy can be caused by antigorite CPO formed by syn-kinematic serpentization in subduction zones.

## REFERENCES

- Abers, G.A., Van Keken, P.E., Hacker, B.R., 2017. The cold and relatively dry nature of mantle forearcs in subduction zones. *Nature Geoscience* 10, 333-337.
- Alisic, L., Gurnis, M., Stadler, G., Burstedde, C., Ghattas, O., 2012. Multi-scale dynamics and rheology of mantle flow with plates. *Journal of Geophysical Research* 117.
- Almqvist, B.S.G., Mainprice, D., 2017. Seismic properties and anisotropy of the continental crust: Predictions based on mineral texture and rock microstructure. *Reviews of Geophysics* 55, 367-433.
- Amiguet, E., Raterron, P., Cordier, P., Couvy, H., Chen, J., 2009. Deformation of diopside single crystal at mantle pressure. 1: Mechanical data. *Physics of the Earth and Planetary Interiors* 177, 122-129.
- Amiguet, E., Van De Moortèle, B., Cordier, P., Hilairret, N., Reynard, B., 2014a. Deformation mechanisms and rheology of serpentines in experiments and in nature. *Journal of Geophysical Research: Solid Earth* 119, 4640-4655.
- Amiguet, E., Van de Moortèle, B., Cordier, P., Hilairret, N., Reynard, B., 2014b. Deformation mechanisms and rheology of serpentines in experiments and in nature. *Journal of Geophysical Research* 119, 1-16.

- Antonijevic, S.K., Wagner, L.S., Beck, S.L., Long, M.D., Zandt, G., Tavera, H., 2016. Effects of change in slab geometry on the mantle flow and slab fabric in Southern Peru. *Journal of Geophysical Research* 121, 7252-7270.
- Auzende, A.-L., Escartin, J., Walte, N.P., Guillot, S., Hirth, G., Frost, D.J., 2015. Deformation mechanisms of antigorite serpentinite at subduction zone conditions determined from experimentally and naturally deformed rocks. *Earth and Planetary Science Letters* 411, 229-240.
- Auzende, A.-L., Guillot, S., Devouard, B., Baronnet, A., 2006. Serpentinities in an Alpine convergent setting: Effects of metamorphic grade and deformation on microstructures. *European Journal of Mineralogy* 18, 21-33.
- Avé Lallemant, H.G., 1978. Experimental deformation of diopside and websterite. *Tectonophysics* 48, 1-27.
- Babuška, V., Fiala, J., Kumazawa, M., Ohno, I., Sumino, Y., 1978. Elastic properties of garnet solid-solution series. *Physics of the Earth and Planetary Interiors* 16, 157-176.
- Baldwin, J.A., Powell, R., Brown, M., Moraes, R., Fuck, R.A., 2005. Modelling of mineral equilibria in ultrahigh-temperature metamorphic rocks from the Anápolis-Itaçu Complex, central Brazil. *Journal of Metamorphic Geology* 23, 511-531.

- Bebout, G.E., Barton, M.D., 2002. Tectonic and metasomatic mixing in a high-*T*, subduction-zone *mélange*—insights into the geochemical evolution of the slab–mantle interface. *Chemical Geology* 187, 79-106.
- Ben Ismail, W., Mainprice, D., 1998. An olivine fabric database: an overview of upper mantle fabrics and seismic anisotropy. *Tectonophysics* 296, 145-157.
- Bezacier, L., Reynard, B., Bass, J.D., Sanchez-Valle, C., Van de Moortèle, B., 2010a. Elasticity of antigorite, seismic detection of serpentinites, and anisotropy in subduction zones. *Earth and Planetary Science Letters* 289, 198-208.
- Bezacier, L., Reynard, B., Bass, J.D., Wang, J., Mainprice, D., 2010b. Elasticity of glaucophane, seismic velocities and anisotropy of the subducted oceanic crust. *Tectonophysics* 494, 201-210.
- Blanco-Quintero, I.F., Proenza, J.A., García-Casco, A., Tauler, E., Galí, S., 2011. Serpentinites and serpentinites within a fossil subduction channel: La Corea *mélange*, eastern Cuba. *Geological Acta* 9, 389-405.
- Boneh, Y., Wallis, D., Hansen, L.N., Krawczynski, M.J., Skemer, P., 2017. Oriented grain growth and modification of ‘frozen anisotropy’ in

- the lithospheric mantle. *Earth and Planetary Science Letters* 474, 368-374.
- Bose, K., Ganguly, J., 1995. Experimental and theoretical studies of the stability of talc, antigorite and phase A at high pressures with applications to subduction processes. *Earth and Planetary Science Letters* 136, 109-121.
- Boudier, F., Baronnet, A., Mainprice, D., 2010. Serpentine mineral replacements of natural olivine and their seismic implications: oceanic lizardite versus subduction-related antigorite. *Journal of Petrology* 51, 495-512.
- Brovarone, A.V., Beltrando, M., Malavieille, J., Giuntoli, F., Tondella, E., Groppo, C., Beyssac, O., Compagnoni, R., 2011. Inherited Ocean-Continent Transition zones in deeply subducted terranes: Insights from Alpine Corsica. *Lithos* 124, 273-290.
- Brovarone, A.V., Beyssac, O., Malavieille, J., Molli, G., Beltrando, M., Compagnoni, R., 2013. Stacking and metamorphism of continuous segments of subducted lithosphere in a high-pressure wedge: The example of Alpine Corsica (France). *Earth-Science Reviews* 116, 35-56.
- Brownlee, S.J., Hacker, B.R., Harlow, G.E., Seward, G., 2013. Seismic signatures of a hydrated mantle wedge from antigorite crystal-

- preferred orientation (CPO). *Earth and Planetary Science Letters* 375, 395-407.
- Bunge, H.J., 1982. *Texture analysis in materials science: Mathematical methods*. Butterworth&Co, London.
- Bystricky, M., Mackwell, S., 2001. Creep of dry clinopyroxene aggregates. *Journal of Geophysical Research: Solid Earth* (1978–2012) 106, 13443-13454.
- Cao, Y., Jung, H., Song, S., 2013. Petro-fabrics and seismic properties of blueschist and eclogite in the North Qilian suture zone, NW China: Implications for the low-velocity upper layer in subducting slab, trench-parallel seismic anisotropy, and eclogite detectability in the subduction zone. *Journal of Geophysical Research* 118, 3037-3058.
- Cao, Y., Jung, H., Song, S., 2017. Olivine fabrics and tectonic evolution of fore-arc mantles: A natural perspective from the Songshugou dunite and harzburgite in the Qinling orogenic belt, central China. *Geochemistry, Geophysics, Geosystems* 18, 907-934.
- Capitani, d.C., Petrakakis, K., 2010. The computation of equilibrium assemblage diagrams with Theriak/Domino software. *American Mineralogist* 95, 1006-1016.
- Chheda, T.D., Mookherjee, M., Mainprice, D., dos Santos, A.M., Molaison, J.J., Chantel, J., Manthilake, G., Bassett, W.A., 2014. Structure and

- elasticity of phlogopite under compression: Geophysical implications. *Physics of the Earth and Planetary Interiors* 233, 1-12.
- Choi, S., Fabbri, O., Topuz, G., Okay, A.I., Jung, H., 2021. Twin induced reduction of seismic anisotropy in lawsonite blueschist. *Minerals* 11.
- Chopin, C., 1984. Coesite and pure pyrope in high-grade blueschists of the Western Alps: a first record and some consequences. *Contributions to Mineralogy and Petrology* 86, 107-118.
- Coggon, R., Holland, T.J.B., 2002. Mixing properties of phengitic micas and revised garnet-phengite thermobarometers. *Journal of Metamorphic Geology* 20, 683-696.
- Comodi, P., Mellini, M., Zanazzi, P.F., 1992. Magnesiochloritoid: Compressibility and high pressure structure refinement. *Physics and Chemistry of Minerals* 18, 483-490.
- Dempsey, E.D., Prior, D.J., Mariani, E., Toy, V.G., Tatham, D.J., 2011. Mica-controlled anisotropy within mid-to-upper crustal mylonites: an EBSD study of mica fabrics in the Alpine Fault Zone, New Zealand. *Geological Society, London, Special Publications* 360, 33-47.
- Diener, J.F.A., Powell, R., 2012. Revised activity-composition models for clinopyroxene and amphibole. *Journal of Metamorphic Geology* 30, 131-142.

- Dlingan, M.A., 1979. Bastite pseudomorphs after orthopyroxene, clinopyroxene and tremolite. *The Canadian Mineralogist* 17, 729-740.
- Escartín, J., Andreani, M., Hirth, G., Evans, B., 2008. Relationships between the microstructural evolution and the rheology of talc at elevated pressures and temperatures. *Earth and Planetary Science Letters* 268, 463-475.
- Evans, B.W., 1977. Metamorphism of Alpine peridotite and serpentinite. *Annual Review of Earth and Planetary Sciences* 5, 397-447.
- Faccenda, M., Burlini, L., Gerya, T.V., Mainprice, D., 2008. Fault-induced seismic anisotropy by hydration in subducting oceanic plates. *Nature* 455, 1097-1100.
- Frost, R.B., Beard, J.S., 2007. On silica activity and serpentinization. *Journal of Petrology* 48, 1351-1368.
- Ghent, E.D., Stout, M.Z., Black, P.M., Brothers, R.N., 1987. Chloritoid-bearing rocks associated with blueschists and eclogites, northern New Caledonia. *Journal of Metamorphic Geology* 5, 239-254.
- Gifkins, R.C., 1970. *Optical microscopy of metals*, 1st ed. Elsevier, New York.
- Green, E., Holland, T.J.B., Powell, R., 2007. An order-disorder model for omphacitic pyroxenes in the system jadeite-diopside-hedenbergite-acmite, with applications to eclogitic rocks. *American Mineralogist* 92, 1181-1189.



- Grevel, K.-D., Kahl, W.-A., Majzlan, J., Navrotsky, A., Lathe, C., Fockenberg, T., 2005. Thermodynamic properties of magnesiochloritoid. *European Journal of Mineralogy* 17, 587-598.
- Griggs, D., Blacic, J., Heard, H., 1960. Deformation of Rocks at 500° to 800° C, *Geological Society of America Memoirs*, pp. 39-104.
- Guillot, S., Hattori, K., Agard, P., Schwartz, S., Vidal, O., 2009. Exhumation processes in oceanic and continental subduction contexts: A review, in: Lallemand, S., Funiciello, F. (Eds.), *Subduction Zone Geodynamics*. Springer, Berlin, Heidelberg, pp. 175-205.
- Ha, Y., Jung, H., Raymond, L.A., 2018. Deformation fabrics of glaucophane schists and implications for seismic anisotropy: the importance of lattice preferred orientation of phengite. *International Geology Review* 61, 1-18.
- Hacker, B.R., Abers, G.A., Peacock, S.M., 2003. Subduction factory 1. Theoretical mineralogy, densities, seismic wave speeds, and H<sub>2</sub>O contents. *Journal of Geophysical Research* 108.
- Haerinck, T., Adriaens, R., Debacker, T.N., Hirt, A.M., Sintubin, M., 2013. Paramagnetic metamorphic mineral assemblages controlling AMS in low-grade deformed metasediments and the implications with respect to the use of AMS as a strain marker. *Journal of the Geological Society* 170, 263-280.

- Haerinck, T., Wenk, H.-R., Debacker, T.N., Sintubin, M., 2015. Preferred mineral orientation of a chloritoid-bearing slate in relation to its magnetic fabric. *Journal of Structural Geology* 71, 125-135.
- Hansen, L.N., Zhao, Y.H., Zimmerman, M.E., Kohlstedt, D.L., 2014. Protracted fabric evolution in olivine: Implications for the relationship among strain, crystallographic fabric, and seismic anisotropy. *Earth and Planetary Science Letters* 387, 157-168.
- Healy, D., Reddy, S.M., Timms, N.E., Gray, E.M., Brovarone, A.V., 2009. Trench-parallel fast axes of seismic anisotropy due to fluid-filled cracks in subducting slabs. *Earth and Planetary Science Letters* 283, 75-86.
- Heyliger, P., Ledbetter, H., Kim, S., 2003. Elastic constants of natural quartz. *The Journal of the Acoustical Society of America* 114, 644-650.
- Hirauchi, K.-i., den Hartog, S.A.M., Spiers, C.J., 2013. Weakening of the slab–mantle wedge interface induced by metasomatic growth of talc. *Geology* 41, 75-78.
- Hirauchi, K.-i., Michibayashi, K., Ueda, H., Katayama, I., 2010. Spatial variations in antigorite fabric across a serpentinite subduction channel: Insights from the Ohmachi Seamount, Izu-Bonin frontal arc. *Earth and Planetary Science Letters* 299, 196-206.
- Hirauchi, K.-i., Nagata, Y., Kataoka, K., Oyanagi, R., Okamoto, A., Michibayashi, K., 2021. Cataclastic and crystal-plastic deformation

- in shallow mantle-wedge serpentinite controlled by cyclic changes in pore fluid pressures. *Earth and Planetary Science Letters* 576.
- Hohenberg, P., Kohn, W., 1964. Inhomogeneous electron gas. *Physical Review* 136, B864-B871.
- Holland, T., Powell, R., 1996. Thermodynamics of order-disorder in minerals: II. Symmetric formalism applied to solid solutions. *American Mineralogist* 81, 1425-1437.
- Holland, T.J.B., Baker, J., Powell, R., 1998. Mixing properties and activity-composition relationships of chlorites in the system MgO-FeO-Al<sub>2</sub>O<sub>3</sub>-SiO<sub>2</sub>-H<sub>2</sub>O. *European Journal of Mineralogy* 10, 395-406.
- Holland, T.J.B., Powell, R., 1998. An internally consistent thermodynamic data set for phases of petrological interest. *Journal of Metamorphic Geology* 16, 309-343.
- Holland, T.J.B., Powell, R., 2011. An improved and extended internally consistent thermodynamic dataset for phases of petrological interest, involving a new equation of state for solids. *Journal of Metamorphic Geology* 29, 333-383.
- Horn, C., Bouilhol, P., Skemer, P., 2020. Serpentinization, deformation, and seismic anisotropy in the subduction mantle wedge. *Geochemistry, Geophysics, Geosystems* 21, 1-17.
- Hua, Y., Zhao, D., Xu, Y., 2017. P wave anisotropic tomography of the Alps. *Journal of Geophysical Research* 122, 4509-4528.

- Huang, Z., Zhao, D., Wang, L., 2011. Shear wave anisotropy in the crust, mantle wedge, and subducting Pacific slab under northeast Japan. *Geochemistry, Geophysics, Geosystems* 12, n/a-n/a.
- Ingrin, J., Doukhan, N., Doukhan, J.-C., 1992. Dislocation glide systems in diopside single crystals deformed at 800-900°C. *European Journal of Mineralogy* 4, 1291-1302.
- Ishise, M., Kawakatsu, H., Morishige, M., Shiomi, K., 2018. Radial and azimuthal anisotropy tomography of the NE Japan subduction zone: Implications for the Pacific slab and mantle wedge dynamics. *Geophysical Research Letters* 45, 3923-3931.
- Ji, S., Shao, T., Michibayashi, K., Long, C., Wang, Q., Kondo, Y., Zhao, W., Wang, H., Salisbury, M.H., 2013. A new calibration of seismic velocities, anisotropy, fabrics, and elastic moduli of amphibole-rich rocks. *Journal of Geophysical Research* 118, 4699-4728.
- Jung, H., 2011. Seismic anisotropy produced by serpentine in mantle wedge. *Earth and Planetary Science Letters* 307, 535-543.
- Jung, H., 2017. Crystal preferred orientations of olivine, orthopyroxene, serpentine, chlorite, and amphibole, and implications for seismic anisotropy in subduction zones: a review. *Geosciences Journal* 21, 985-1011.
- Jung, H., Karato, S.-i., 2001. Water-induced fabric transitions in olivine. *Science* 293, 1460-1463.

- Jung, H., Katayama, I., Jiang, Z., Hiraga, T., Karato, S.-i., 2006. Effect of water and stress on the lattice-preferred orientation of olivine. *Tectonophysics* 421, 1-22.
- Jung, H., Mo, W., Green, H.W., 2009. Upper mantle seismic anisotropy resulting from pressure-induced slip transition in olivine. *Nature Geoscience* 2, 73-77.
- Jung, H., Park, M., Jung, S., Lee, J., 2010. Lattice preferred orientation, water content, and seismic anisotropy of orthopyroxene. *Journal of Earth Science* 21, 555-568.
- Jung, S., Jung, H., Austrheim, H.k., 2014. Characterization of olivine fabrics and mylonite in the presence of fluid and implications for seismic anisotropy and shear localization. *Earth, Planets and Space* 66, 1-21.
- Kang, H., Jung, H., 2019. Lattice-preferred orientation of amphibole, chlorite, and olivine found in hydrated mantle peridotites from Bjørkedalen, southwestern Norway, and implications for seismic anisotropy. *Tectonophysics* 750, 137-152.
- Karato, S.-i., Jung, H., Katayama, I., Skemer, P., 2008. Geodynamic significance of seismic anisotropy of the upper mantle: New insights from laboratory studies. *Annual Review of Earth and Planetary Sciences* 36, 59-95.

- Katayama, I., Hirauchi, K.-i., Michibayashi, K., Ando, J.-i., 2009. Trench-parallel anisotropy produced by serpentine deformation in the hydrated mantle wedge. *Nature* 461, 1114-1117.
- Katayama, I., Karato, S.-i., 2006. Effect of temperature on the B- to C-type olivine fabric transition and implication for flow pattern in subduction zones. *Physics of the Earth and Planetary Interiors* 157, 33-45.
- Katzir, Y., Garfunkel, Z., Avigad, D., Matthews, A., 2022. The geodynamic evolution of the Alpine orogen in the Cyclades (Aegean Sea, Greece): insights from diverse origins and modes of emplacement of ultramafic rocks. *Geological Society, London, Special Publications* 291, 17-40.
- Kienast, J.R., Messiga, B., 1987. Cr-rich Mg-chloritoid, a first record in high-pressure metagabbros from Monviso (Cottian Alps), Italy. *Mineralogical Magazine* 51, 681-687.
- Kim, D., Jung, H., 2015. Deformation microstructures of olivine and chlorite in chlorite peridotites from Almklovdaalen in the Western Gneiss Region, southwest Norway, and implications for seismic anisotropy. *International Geology Review* 57, 650-668.
- Kim, D., Jung, H., Lee, J., 2020. Strain-induced fabric transition of chlorite and implications for seismic anisotropy in subduction zones. *Minerals* 10, 1-18.

- Kim, D., Wallis, S., Endo, S., Ree, J.H., 2016. Seismic properties of lawsonite eclogites from the southern Motagua fault zone, Guatemala. *Tectonophysics* 677-678, 88-98.
- Kim, Y., Clayton, R.W., Asimow, P.D., Jackson, J.M., 2013. Generation of talc in the mantle wedge and its role in subduction dynamics in central Mexico. *Earth and Planetary Science Letters* 384, 81-87.
- Klein, C., 2002. *Manual of Mineral Science*, 22nd ed. Wiley, New York.
- Kneller, E.A., van Keken, P.E., Karato, S.-i., Park, J., 2005. B-type olivine fabric in the mantle wedge: Insights from high-resolution non-Newtonian subduction zone models. *Earth and Planetary Science Letters* 237, 781-797.
- Kohn, W., Sham, L.J., 1965. Self-Consistent equations including exchange and correlation effects. *Physical Review* 140, A1133-A1138.
- Kollé, J., Blacic, J., 1982. Deformation of single-crystal clinopyroxenes: 1. Mechanical twinning in diopside and hedenbergite. *Journal of Geophysical Research* 87, 4019-4034.
- Kresse, G., Joubert, D., 1999. From ultrasoft pseudopotentials to the projector augmented-wave method. *Physical Review B* 59, 1758-1775.
- Le Roux, V., 2008. Melt-rock interactions and melt-assisted deformation in the Lherz peridotite, with implications for the structural, chemical and isotopic evolution of the lithospheric mantle, *Geochemistry*, University Montpellier 2.

- Lee, J., Jung, H., 2015. Lattice-preferred orientation of olivine found in diamond-bearing garnet peridotites in Finsch, South Africa and implications for seismic anisotropy. *Journal of Structural Geology* 70, 12-22.
- Lee, J., Jung, H., 2021. Lattice-preferred orientation and seismic anisotropy of minerals in retrograded eclogites from Xitieshan, Northwestern China, and implications for seismic reflectance of rocks in the subduction zone. *Minerals* 11.
- Lee, J., Jung, H., Klemd, R., Tarling, M.S., Konopelko, D., 2020. Lattice preferred orientation of talc and implications for seismic anisotropy in subduction zones. *Earth and Planetary Science Letters* 537, 116178.
- Lee, J., Mookherjee, M., Kim, T., Jung, H., Klemd, R., 2021. Seismic anisotropy in subduction zones: evaluating the role of chloritoid. *Frontiers in Earth Science* 9, 1-16.
- Li, X.P., Rahn, M., Bucher, K., 2004. Serpentinites of the Zermatt-Saas ophiolite complex and their texture evolution. *Journal of Metamorphic Geology* 22, 159-177.
- Lin, F.-C., Ritzwoller, M.H., Yang, Y., Moschetti, M.P., Fouch, M.J., 2010. Complex and variable crustal and uppermost mantle seismic anisotropy in the western United States. *Nature Geoscience* 4, 55-61.



- Liu, W., Cao, Y., Zhang, J., Zhang, Y., Zong, K., Jin, Z., 2020a. Thermo-structural evolution of the Val Malenco (Italy) Peridotite: a petrological, geochemical and microstructural Study. *Minerals* 10.
- Liu, W., Zhang, J., Cao, Y., Jin, Z., 2020b. Geneses of two contrasting antigorite crystal preferred orientations and their implications for seismic anisotropy in the forearc mantle. *Journal of Geophysical Research* 125.
- Lloyd, G.E., Butler, R.W.H., Casey, M., Mainprice, D., 2009. Mica, deformation fabrics and the seismic properties of the continental crust. *Earth and Planetary Science Letters* 288, 320-328.
- Long, M.D., 2013. Constraints on subduction geodynamics from seismic anisotropy. *Reviews of Geophysics* 51, 76-112.
- Long, M.D., Silver, P.G., 2008. The subduction zone flow field from seismic anisotropy: A global view. *Science* 319, 315-318.
- Mainprice, D., 1990. A FORTRAN program to calculate seismic anisotropy from the lattice preferred orientation of minerals. *Computers & Geosciences* 16, 385-393.
- Mainprice, D., Bachmann, F., Hielscher, R., Schaeben, H., Lloyd, G.E., 2014. Calculating anisotropic piezoelectric properties from texture data using the MTEX open source package. *Geological Society, London, Special Publications* 409, 223-249.

- Mainprice, D., Hielscher, R., Schaebe, H., 2011. Calculating anisotropic physical properties from texture data using the MTEX open-source package. Geological Society Special Publication 360, 175-192.
- Mainprice, D., Ildefonse, B., 2009. Seismic anisotropy of subduction zone minerals-Contribution of hydrous phases, in: Lallemand, S., Funiciello, F. (Eds.), Subduction Zone Geodynamics. Springer, Berlin, Heidelberg, pp. 63-84.
- Mainprice, D., Le Page, Y., Rodgers, J., Jouanna, P., 2008. *Ab initio* elastic properties of talc from 0 to 12 GPa: Interpretation of seismic velocities at mantle pressures and prediction of auxetic behaviour at low pressure. Earth and Planetary Science Letters 274, 327-338.
- McCormack, K., Wirth, E.A., Long, M.D., 2013. B-type olivine fabric and mantle wedge serpentinization beneath the Ryukyu arc. Geophysical Research Letters 40, 1697-1702.
- Menzel, M.D., Garrido, C.J., López Sánchez-Vizcaíno, V., Hidas, K., Marchesi, C., 2019. Subduction metamorphism of serpentinite-hosted carbonates beyond antigorite-serpentinite dehydration (Nevado-Filábride Complex, Spain). Journal of Metamorphic Geology 37, 681-715.
- Messiga, B., Kienast, J.R., Rebay, G., Riccardi, M.P., Tribuzio, R., 1999. Cr-rich magnesiochloritoid eclogites from the Monviso ophiolites

- (Western Alps, Italy). *Journal of Metamorphic Geology* 17, 287-299.
- Messiga, B., Scambelluri, M., Piccardo, G.B., 1995. Chloritoid-bearing assemblages in mafic systems and eclogite-facies hydration of Alpine Mg-Al metagabbros (Erro-Tobbio unit, Ligurian western Alps). *European Journal of Mineralogy* 7, 1149-1167.
- Meyer, M., Klemm, R., Hegner, E., Konopelko, D., 2014. Subduction and exhumation mechanisms of ultra-high and high-pressure oceanic and continental crust at Makbal (Tianshan, Kazakhstan and Kyrgyzstan). *Journal of Metamorphic Geology* 32, 861-884.
- Michibayashi, K., Mainprice, D., Fujii, A., Uehara, S., Shinkai, Y., Kondo, Y., Ohara, Y., Ishii, T., Fryer, P., Bloomer, S.H., Ishiwatari, A., Hawkins, J.W., Ji, S., 2016. Natural olivine crystal-fabrics in the western Pacific convergence region: A new method to identify fabric type. *Earth and Planetary Science Letters* 443, 70-80.
- Mizukami, T., Yokoyama, H., Hiramatsu, Y., Arai, S., Kawahara, H., Nagaya, T., Wallis, S.R., 2014. Two types of antigorite serpentinite controlling heterogeneous slow-slip behaviours of slab-mantle interface. *Earth and Planetary Science Letters* 401, 148-158.
- Monkhorst, H.J., Pack, J.D., 1976. Special points for Brillouin-zone integrations. *Physical Review B* 13, 5188-5192.

- Mookherjee, M., Bezacier, L., 2012. The low velocity layer in subduction zone: Structure and elasticity of glaucophane at high pressures. *Physics of the Earth and Planetary Interiors* 208-209, 50-58.
- Mookherjee, M., Capitani, G.C., 2011. Trench parallel anisotropy and large delay times: Elasticity and anisotropy of antigorite at high pressures. *Geophysical Research Letters* 38, L09315.
- Mookherjee, M., Mainprice, D., 2014. Unusually large shear-wave anisotropy for chlorite in subductin zone settings. *Geophysical Research Letters* 41, 1506-1513.
- Moore, D.E., Rymer, M.J., 2007. Talc-bearing serpentinite and the creeping section of the San Andreas fault. *Nature* 448, 795-797.
- Morales, L.F.G., Mainprice, D., Boudier, F., 2013. The influence of hydrous phases on the microstructure and seismic properties of a hydrated mantle rock. *Tectonophysics* 594, 103-117.
- Morales, L.F.G., Mainprice, D., Kern, H., 2018. Olivine-antigorite orientation relationships: Microstructures, phase boundary misorientations and the effect of cracks in the seismic properties of serpentinites. *Tectonophysics* 724-725, 93-115.
- Nagaya, T., Okamoto, A., Oyanagi, R., Seto, Y., Miyake, A., Uno, M., Muto, J., Wallis, S.R., 2020. Crystallographic preferred orientation of talc determined by an improved EBSD procedure for sheet silicates:

- Implications for anisotropy at the slab–mantle interface due to Si-metasomatism. *American Mineralogist* 105, 873-893.
- Nagaya, T., Walker, A.M., Wookey, J., Wallis, S.R., Ishii, K., Kendall, J.-M., 2016. Seismic evidence for flow in the hydrated mantle wedge of the Ryukyu subduction zone. *Scientific Reports* 6, 29981.
- Nagaya, T., Wallis, S.R., Kobayashi, H., Michibayashi, K., Mizukami, T., Seto, Y., Miyake, A., Matsumoto, M., 2014. Dehydration breakdown of antigorite and the formation of B-type olivine CPO. *Earth and Planetary Science Letters* 387, 67-76.
- Negulescu, E., Sabau, G., Massonne, H.-J., 2009. Chloritoid-Bearing Mineral Assemblages in High-Pressure Metapelites from the Bughea Complex, Leaota Massif (South Carpathians). *Journal of Petrology* 50, 103-125.
- Nesse, W.D., 2009. Introduction to optical mineralogy. Oxford University Press.
- Nicolas, A., Christensen, N.I., 1987. Formation of anisotropy in upper mantle peridotites - A review. American Geophysical Union (AGU).
- Nishiyama, T., Yoshida-Shiosaki, C., Mori, Y., Shigeno, M., 2017. Interplay of irreversible reactions and deformation: A case of hydrofracturing in the rodingite–serpentinite system. *Progress in Earth and Planetary Science* 4, 1.

- Niu, X., Zhao, D., Li, J., Ruan, A., 2016. *P* wave azimuthal and radial anisotropy of the Hokkaido subduction zone. *Journal of Geophysical Research* 121, 2636-2660.
- Nozaka, T., 2005. Metamorphic history of serpentinite mylonites from the Happo ultramafic complex, central Japan. *Journal of Metamorphic Geology* 23, 711-723.
- Ohuchi, T., Kawazoe, T., Nishihara, Y., Nishiyama, N., Irifune, T., 2011. High pressure and temperature fabric transitions in olivine and variations in upper mantle seismic anisotropy. *Earth and Planetary Science Letters* 304, 55-63.
- Oyanagi, R., Okamoto, A., Harigane, Y., Tsuchiya, N., 2018. Al-zoning of serpentine aggregates in mesh texture induced by metasomatic replacement reactions. *Journal of Petrology* 59, 613-634.
- Padrón-Navarta, J.A., Sánchez-Vizcaíno, V.L., Hermann, J., Connolly, J.A.D., Garrido, C.J., Gómez-Pugnaire, M.T., Marchesi, C., 2013. Tschermak's substitution in antigorite and consequences for phase relations and water liberation in high-grade serpentinites. *Lithos* 178, 186-196.
- Padrón-Navarta, J.A., Tommasi, A., Garrido, C.J., López Sánchez-Vizcaíno, V., 2012. Plastic deformation and development of antigorite crystal preferred orientation in high-pressure serpentinites. *Earth and Planetary Science Letters* 349-350, 75-86.

- Padrón-Navarta, J.A., Tommasi, A., Garrido, C.J., Mainprice, D., 2015. On topotaxy and compaction during antigorite and chlorite dehydration: an experimental and natural study. *Contributions to Mineralogy and Petrology* 169, 1-20.
- Park, M., Kil, Y., Jung, H., 2020. Evolution of deformation fabrics related to petrogenesis of upper mantle xenoliths beneath the Baekdusan Volcano. *Minerals* 10.
- Park, Y., Jung, H., 2015. Deformation microstructures of olivine and pyroxene in mantle xenoliths in Shanwang, eastern China, near the convergent plate margin, and implications for seismic anisotropy. *International Geology Review* 57, 629-649.
- Pawley, A.R., Wood, B.J., 1995. The high-pressure stability of talc and 10 Å phase: Potential storage sites for H<sub>2</sub>O in subduction zones. *American Mineralogist* 80, 998-1003.
- Peacock, S.M., 2003. Thermal structure and metamorphic evolution of subducting slabs. *Geophysical Monograph Series* 138, 7-22.
- Peng, Y., Mookherjee, M., 2020. Thermoelasticity of tremolite amphibole: Geophysical implications. *American Mineralogist* 105, 904-916.
- Peng, Y., Mookherjee, M., Hermann, A., Manthilake, G., Mainprice, D., 2022. Anomalous elasticity of talc at high pressures: Implications for subduction systems. *Geoscience Frontiers* 13.

- Poli, S., Schmidt, M.W., 1997. The high-pressure stability of hydrous phases in orogenic belts: an experimental approach on eclogite-forming processes. *Tectonophysics* 273, 169-184.
- Pozgay, S.H., Wiens, D.A., Conder, J.A., Shiobara, H., Sugioka, H., 2007. Complex mantle flow in the Mariana subduction system: Evidence from shear wave splitting. *Geophysical Journal International* 170, 371-386.
- Précigout, J., Prigent, C., Palasse, L., Pochon, A., 2017. Water pumping in mantle shear zones. *Nature Communications* 8, 15736.
- Puelles, P., Gil Ibarguchi, J.I., Beranoaguirre, A., Ábalos, B., 2012. Mantle wedge deformation recorded by high-temperature peridotite fabric superposition and hydrous retrogression (Limo massif, Cabo Ortegal, NW Spain). *International Journal of Earth Sciences* 101, 1835-1853.
- Read, H.H., 1934. On zoned associations of antigorite, talc, actinolite, chlorite, and biotite in Unst, Shetland Islands. *Mineralogical Magazine and Journal of the Mineralogical Society* 23, 519-540.
- Regis, D., Rubatto, D., Darling, J., Cenko-Tok, B., Zucali, M., Engi, M., 2014. Multiple metamorphic stages within an eclogite-facies terrane (Sesia Zone, Western Alps) revealed by Th-U-Pb petrochronology. *Journal of Petrology* 55, 1429-1456.



- Russo, R.M., Silver, P.G., 1994. Trench-parallel flow beneath the Nazca plate from seismic anisotropy. *Science* (New York, N.Y.) 263, 1105-1111.
- Sang, L., Bass, J.D., 2014. Single-crystal elasticity of diopside to 14GPa by Brillouin scattering. *Physics of the Earth and Planetary Interiors* 228, 75-79.
- Sang, L., Vanpeteghem, C.B., Sinogeikin, S.V., Bass, J.D., 2011. The elastic properties of diopside,  $\text{CaMgSi}_2\text{O}_6$ . *American Mineralogist* 96, 224-227.
- Satta, N., Grafulha Morales, L.F., Criniti, G., Kurnosov, A., Boffa Ballaran, T., Speziale, S., Marquardt, K., Capitani, G.C., Marquardt, H., 2022. Single-crystal elasticity of antigorite at high pressures and seismic detection of serpentinized slabs. *Geophysical Research Letters* 49.
- Savage, M.K., 1999. Seismic anisotropy and mantle deformation: What have we learned from shear wave splitting? *Reviews of Geophysics* 37, 65-106.
- Schmidt, M.W., Poli, S., 1998. Experimentally based water budgets for dehydrating slabs and consequences for arc magma generation. *Earth and Planetary Science Letters* 163, 361-379.
- Shaw, D.M., 1956. Geochemistry of pelitic rocks. Part III: Major elements and general geochemistry. *Bulletin of the Geological Society of America* 67, 919-934.

- Skemer, P., Hansen, L.N., 2016. Inferring upper-mantle flow from seismic anisotropy: An experimental perspective. *Tectonophysics* 668-669, 1-14.
- Skemer, P., Katayama, I., Jiang, Z., Karato, S.I., 2005. The misorientation index: Development of a new method for calculating the strength of lattice-preferred orientation. *Tectonophysics* 411, 157-167.
- Skemer, P., Katayama, I., Karato, S.-i., 2006. Deformation fabrics of the Cima di Gagnone peridotite massif, Central Alps, Switzerland: Evidence of deformation at low temperatures in the presence of water. *Contributions to Mineralogy and Petrology* 152, 43-51.
- Smith, G.P., Wiens, D.A., Fischer, K.M., Dorman, L.M., Webb, S.C., Hildebrand, J.A., 2001. A complex pattern of mantle flow in the Lau backarc. *Science* 292, 713-716.
- Smye, A.J., Greenwood, L.V., Holland, T.J.B., 2010. Garnet-chloritoid-kyanite assemblages: Eclogite facies indicators of subduction constraints in orogenic belts. *Journal of Metamorphic Geology* 28, 753-768.
- Soda, Y., Wenk, H.-R., 2014. Antigorite crystallographic preferred orientations in serpentinites from Japan. *Tectonophysics* 615-616, 199-212.
- Soustelle, V., Manthilake, G., 2017. Deformation of olivine-orthopyroxene aggregates at high pressure and temperature: Implications for the

- seismic properties of the asthenosphere. *Tectonophysics* 694, 385-399.
- Spandler, C., Hermann, J., Faure, K., Mavrogenes, J.A., Arculus, R.J., 2008. The importance of talc and chlorite "hybrid" rocks for volatile recycling through subduction zones; evidence from the high-pressure subduction mélange of New Caledonia. *Contributions to Mineralogy and Petrology* 155, 181-198.
- Stubailo, I., Beghein, C., Davis, P.M., 2012. Structure and anisotropy of the Mexico subduction zone based on Rayleigh-wave analysis and implications for the geometry of the Trans-Mexican Volcanic Belt. *Journal of Geophysical Research* 117.
- Syracuse, E.M., van Keken, P.E., Abers, G.A., Suetsugu, D., Bina, C., Inoue, T., Wiens, D., Jellinek, M., 2010. The global range of subduction zone thermal models. *Physics of the Earth and Planetary Interiors* 183, 73-90.
- Tommasi, A., Vauchez, A., 2015. Heterogeneity and anisotropy in the lithospheric mantle. *Tectonophysics* 661, 11-37.
- Tulley, C.J., Fagereng, Å., Ujiie, K., Piazzolo, S., Tarling, M.S., Mori, Y., 2022. Rheology of naturally deformed antigorite serpentinite: Strain and strain-rate dependence at mantle-wedge conditions. *Geophysical Research Letters* 49.

- Uchida, N., Nakajima, J., Wang, K., Takagi, R., Yoshida, K., Nakayama, T., Hino, R., Okada, T., Asano, Y., 2020. Stagnant forearc mantle wedge inferred from mapping of shear-wave anisotropy using S-net seafloor seismometers. *Nat Commun* 11, 5676.
- Valenzuela, R.W., León Soto, G., 2017. Shear wave splitting and mantle flow in Mexico: what have we learned? *Geofísica Internacional* 56, 187-217.
- van Keken, P.E., Kiefer, B., Peacock, S.M., 2002. High-resolution models of subduction zones: Implications for mineral dehydration reactions and the transport of water into the deep mantle. *Geochemistry, Geophysics, Geosystems* 3.
- Vaughan, M.T., Guggenheim, S., 1986. Elasticity of muscovite and its relationship to crystal structure. *Journal of Geophysical Research* 91, 4657.
- Velde, B., 1988. Experimental pseudomorphism of diopside by talc and serpentine in (Ni, Mg)Cl<sub>2</sub> aqueous solutions. *Geochemica et Cosmochimica Acta* 52, 415-424.
- Walker, A.M., Wookey, J., 2012. MSAT—A new toolkit for the analysis of elastic and seismic anisotropy. *Computers and Geosciences* 49, 81-90.
- Wang, J., Huang, X., Zhao, D., Yao, Z., 2019. Seismic anisotropy evidence for ductile deformation of the forearc lithospheric mantle in

- subduction zones. *Journal of Geophysical Research* 124, 7013-7027.
- Wang, J., Zhao, D., 2013. P-wave tomography for 3-D radial and azimuthal anisotropy of tohoku and kyushu subduction zones. *Geophysical Journal International* 193, 1161-1181.
- Wang, J., Zhao, D., Yao, Z., 2017. Seismic anisotropy evidence for dehydration embrittlement triggering intermediate-depth earthquakes. *Scientific Reports* 7.
- Watanabe, T., Shirasugi, Y., Michibayashi, K., 2014. A new method for calculating seismic velocities in rocks containing strongly dimensionally anisotropic mineral grains and its application to antigorite-bearing serpentinite mylonites. *Earth and Planetary Science Letters* 391, 24-35.
- Wei, C.J., Song, S.G., 2008. Chloritoid–glaucophane schist in the north Qilian orogen, NW China: phase equilibria and P–T path from garnet zonation. *Journal of Metamorphic Geology* 26, 301-316.
- Wenk, H.-R., Kanitpanyacharoen, W., Voltolini, M., 2010. Preferred orientation of phyllosilicates: Comparison of fault gouge, shale and schist. *Journal of Structural Geology* 32, 478-489.
- White, R.W., Powell, R., Holland, T.J.B., 2007. Progress relating to calculation of partial melting equilibria for metapelites. *Journal of Metamorphic Geology* 25, 511-527.

- White, R.W., Powell, R., Holland, T.J.B., Johnson, T.E., Green, E.C.R., 2014. New mineral activity-composition relations for thermodynamic calculations in metapelitic systems. *Journal of Metamorphic Geology* 32, 261-286.
- White, R.W., Powell, R., Holland, T.J.B., Worley, B.A., 2000. The effect of TiO<sub>2</sub> and Fe<sub>2</sub>O<sub>3</sub> on metapelitic assemblages at greenschist and amphibolite facies conditions: mineral equilibria calculations in the system K<sub>2</sub>O-FeO-MgO-Al<sub>2</sub>O<sub>3</sub>-SiO<sub>2</sub>-H<sub>2</sub>O-TiO<sub>2</sub>-Fe<sub>2</sub>O<sub>3</sub>. *Journal of Metamorphic Geology* 18, 497-511.
- Wirth, E.A., Long, M.D., 2012. Multiple layers of seismic anisotropy and a low-velocity region in the mantle wedge beneath Japan: Evidence from teleseismic receiver functions. *Geochemistry, Geophysics, Geosystems* 13.
- Zhao, D., Yu, S., Liu, X., 2016. Seismic anisotropy tomography: New insight into subduction dynamics. *Gondwana Research* 33, 24-43.
- Zhou, D., Cao, S., Liu, J., Li, X., Dong, Y., Neubauer, F., Bai, J., Li, H., 2022. Carbonation and serpentinization of diopside in the Altun Mountains, NW China. *Scientific Reports* 12, 21361.

## 국문 초록

전세계적으로 섭입대에서는 지진과 이방성이 관찰되고 있으며 섭입대에서 활발히 일어나는 수화작용으로 인해 풍부하게 산출되는 함수광물들이 이러한 지진과 이방성에 중요하다는 것이 일반적으로 알려져 있다. 함수광물들은 그 단결정이 매우 큰 탄성적 이방성을 갖고 있는 것이 특징이며, 이 광물들이 연성 변형을 받아 형성되는 강한 결정선호방향 (crystallographic preferred orientation; CPO)은 강한 지진과 이방성을 야기하는 데에 있어 매우 중요하다. 그러나, 섭입대에는 매우 많은 종류의 함수광물들이 산출되며 그 광물들이 섭입대에서 변형을 받아 만들어지는 결정선호방향에 대한 연구가 부족한 실정이다. 활석과 경록니석은 맨틀 웨지와 섭입 경계면에서 산출되는 대표적인 함수광물이며, 사문석은 맨틀 웨지에서 가장 풍부하게 산출되는 함수광물로 알려져 있다. 따라서, 본 학위논문에서는 카자흐스탄-키르기즈스탄의 텐산 지역 내 막발 복합체에서 산출되는 석류석-경록니석-활석 편암과 영국 스코틀랜드의 발라 복합체에서 산출되는 활석-트레몰라이트-록니석 편암 내에서 관찰되는 활석 결정선호방향을 측정하였고, 막발 복합체의 석류석-경록니석-활석 편암 내에서 관찰되는 경록니석 결정선호방향을 측정하였으며, 또한 프랑스 코르시카의 몬테 산 페이트론 일대에서 산출되는 다이옵사이드 사문암 내에서 관찰되는 안티고라이트 사문석의 결정선호방향을 측정하였다.

활석의 결정선호방향은 활석의 [001]축이 엽리에 수직/아수직하게 강한 배열을 보여주었고, (100) 와 (010) 극은 엽리에 아평행한 약한 거들형태의 배열을 보여주었다. 활석의 강한 [001]축 배열은 강한 P 과 이방성 ( $AV_p = 67 - 72 \%$ )을 만들 수 있음을 발견했고, 고각 ( $\theta > 50^\circ$ )의 섭입대에서 음의 P 과 방위이방성을 만들 수 있음을 밝혀냈다.

경록니석의 결정선호방향은 경록니석의 [001]축이 엽리에 아수직하게 강하게 배열하는 특징을 보였고, (100) 와 (010)극은 엽리에 아평행하게 약한 거들형태 배열을 보여주었다. 이번 연구를 통해 경록니석 단결정의 탄성적 이방성이 최초로 계산되었으며, 경록니석이 안정한 온도-압력 조건을 슈도섹션 연구로 재검증하였다. 경록니석의 결정선호방향 결과와 단결정의 탄성적 이방성을 모두 고려하면, 이들이 차가운 섭입대에서 관측되는 해구-평행한 S 과 이방성 ( $AV_s = 9.7 - 18.1 \%$ )에 크게 영향을 줄 수 있음을 알아냈다.

사문석의 결정선호방향은 사문석의 [001]축이 엽리에 수직/아수직하게 강한 배열을 보이면서 선구조에 수직한 약한 거들형태의 배열을 함께 보여주었다. 사문암 내 다이옵사이드의 결정선호방향 결과를 고려했을 때, 사문석 결정선호방향은 다이옵사이드로부터 사문석이 topotactic growth 로 만들어질 때 형성될 수 있음을 밝혀냈다. 다이옵사이드의 (100)극이 엽리에 수직한 강한



배열을 보이는 것은 이전에 보고된 적이 없던 새로운 결정선호방향으로, 이는 사문석의 (001)면이 엽리에 나란하게 배열하는 동적-사문화작용 동안에 함께 형성되었을 것으로 보인다. 본 연구에서 얻은 사문석의 결정선호방향은 섭입대에서 해구에 평행한 S 과 이방성을 야기할 수 있는 중요한 요인임을 지시한다. 종합하자면, 활석, 경록니석, 사문석과 같은 함수광물들의 강한 결정선호방향은 섭입대에서 관측되는 강한 지진과 이방성을 해석하는 데에 크게 기여할 수 있음을 시사한다.

**주요어:** 결정선호방향, 활석, 경록니석, 사문석, 지진과 이방성, 섭입대.

**학 번 :** 2016-37813